

Radiative heat transfer in glass : the algebraic ray trace method

Citation for published version (APA):

Linden, van der, B. J. (2002). *Radiative heat transfer in glass : the algebraic ray trace method*. [Phd Thesis 1 (Research TU/e / Graduation TU/e), Mathematics and Computer Science]. Technische Universiteit Eindhoven. <https://doi.org/10.6100/IR553564>

DOI:

[10.6100/IR553564](https://doi.org/10.6100/IR553564)

Document status and date:

Published: 01/01/2002

Document Version:

Publisher's PDF, also known as Version of Record (includes final page, issue and volume numbers)

Please check the document version of this publication:

- A submitted manuscript is the version of the article upon submission and before peer-review. There can be important differences between the submitted version and the official published version of record. People interested in the research are advised to contact the author for the final version of the publication, or visit the DOI to the publisher's website.
- The final author version and the galley proof are versions of the publication after peer review.
- The final published version features the final layout of the paper including the volume, issue and page numbers.

[Link to publication](#)

General rights

Copyright and moral rights for the publications made accessible in the public portal are retained by the authors and/or other copyright owners and it is a condition of accessing publications that users recognise and abide by the legal requirements associated with these rights.

- Users may download and print one copy of any publication from the public portal for the purpose of private study or research.
- You may not further distribute the material or use it for any profit-making activity or commercial gain
- You may freely distribute the URL identifying the publication in the public portal.

If the publication is distributed under the terms of Article 25fa of the Dutch Copyright Act, indicated by the "Taverne" license above, please follow below link for the End User Agreement:

www.tue.nl/taverne

Take down policy

If you believe that this document breaches copyright please contact us at:

openaccess@tue.nl

providing details and we will investigate your claim.

Radiative Heat Transfer in Glass: The Algebraic Ray Trace Method

Bas van der Linden

Copyright ©2002 by Bas van der Linden, Helmond, The Netherlands.

All rights are reserved. No part of this publication may be reproduced, stored in a retrieval system, or transmitted, in any form or by any means, electronic, mechanical, photocopying, recording or otherwise, without prior permission of the author.

This research was supported by the Technology Foundation STW, applied science division of NWO and the technology programme of the Ministry of Economic Affairs.

Printed by Universal Press, Veenendaal

CIP-DATA LIBRARY TECHNISCHE UNIVERSITEIT EINDHOVEN

Linden, Bas J. van der

Radiative heat transfer in glass:
the algebraic ray trace method /
by Bas J. van der Linden. -

Eindhoven : Technische Universiteit Eindhoven, 2002. Proefschrift. -
ISBN 90-386-0512-9

NUGI 811

Subject headings: numerical heat transfer / heat radiation / glass
2000 Mathematics Subject Classification: 78A40, 82D30, 49M27

Radiative Heat Transfer in Glass: The Algebraic Ray Trace Method

PROEFSCHRIFT

ter verkrijging van de graad van doctor aan de
Technische Universiteit Eindhoven, op gezag van de
Rector Magnificus, prof.dr. R.A. van Santen, voor een
commissie aangewezen door het College
voor Promoties in het openbaar te verdedigen
op woensdag 3 april 2002 om 16.00 uur

door

Bas Johannes van der Linden

geboren te Helmond

Dit proefschrift is goedgekeurd door de promotoren:

prof.dr. R.M.M. Mattheij

en

prof.dr.ir. A.A. van Steenhoven

Preface

Πάντα στό νου σου νάχεις την Ιθάκη. / Το φθάσιμον εκεί είν' ο προορισμός σου. / Αλλά μη βιάξεις το ταξείδι διόλου. / Καλλίτερα χρόνια πολλά να διαρκέσει· / και γέρος πια ν' αράξεις στο νησί, / πλούσιος με όσα κέρδισες στον δρόμο, / μη προσδοκώντας πλούτη να σε δώσει η Ιθάκη.

K.Π. Καβαφης, *Ιθάκη*

Always keep Ithaca in your mind. / To arrive there is your goal. / But do not rush the voyage at all. / It had better last many a year, / so as an old man you anchor at the island, / rich of all you have gained on the way, / without hoping that Ithaca would offer you riches.

C.P. Cavafy, *Ithaca*

This text presents the main work done for my PhD research on numerical modelling of radiative heat transfer in glass. When I was offered the opportunity to perform this research at the Scientific Computing Group of the Eindhoven University of Technology, it was the radiative part that appealed to me, as I was largely unfamiliar with glass. Although my background was in aerospace engineering and glass does not provoke the emotions that for example a plane does, I have become charmed by the complexity of simulations of glass production over the latter years. Humbly, I realise that heat transfer is only one of the important parts in the understanding of glass production processes: For a complete simulation of the glass production process, we also would need thorough knowledge about the chemistry, the flow, and all the material parameters. Such a simulation would create a complexity not unlike that seen in aeroplane design.

A lot of insight has come from the fact that the research presented in this dissertation is part of a cooperative project. In a joint effort between the Departments of Mathematical, Mechanical and Chemical Engineering, three research projects were started to solve several different but related problems concerning radiative heat transfer in the glass industry. This effort was funded by the Dutch Technology Foundation STW. Next to the construction of a numerical model presented here, the following sister projects were carried out. At the Energy Technology Group, Marco Nagtegaal made a PhD research in the development of a spectral remote sensing method for obtaining temperature measurements without making contact to the hot molten glass. Finally, in the laboratory of TNO-TPD, Jeroen Broekhuijse performed many measurements to construct reliable absorption spectra for industry glasses. Since these topics are complementary rather

than overlapping, this text focuses on the numerical model only instead of a complete overview of the project. The work of Marco Nagtegaal will be published in his thesis which is due to appear in 2002. The work of Jeroen Broekhuijse will unfortunately remain undisclosed to the general public because of intellectual property considerations.

Acknowledgements

Research does not and could not happen in a social void. Rather than a work of a single person, any research is a collection of ideas, support and consultation of a multitude of people. Some of them have been quintessential for the realisation of the research and this dissertation, and I would like to take the opportunity to show my gratitude here.

First, I would like to thank prof.dr. R.M.M. Mattheij. The combination of advice, trust and liberty that he has offered me, has made the research pleasant and fulfilling.

Thanks are also due to the other members of the joint research project, ir. Marco Nagtegaal and ing. Jeroen Broekhuijse. Without our meetings, my understanding of problems in glass melts would be much less. I am also grateful to dr.ir. C.C.M. Rindt for managing the project and making the whole project more of a unity, rather than three separate researches.

The preliminary versions of this dissertations let much to be improved upon, and I am grateful to prof.dr.ir. A.A. van Steenhoven, prof.dr. P.A.J. Hilbers and prof.dr.ir. R.G.C. Beerkens for their thorough inspection. Without their watchful eyes, the thesis would have missed clarity and some examples would have had used the wrong boundary conditions.

Work in the Scientific Computing Group is inspirational thanks to the bright and friendly colleagues. Two of them were my room mates, to which I would like to express my gratitude. The many discussions I had with dr.ir. M.J.H. Anthonissen and K. Laevsky, M.Sc., have let to a better understanding of higher mathematics and a deeper insight in coding.

Finally, one person deserves special attention. Without the loving support of my girlfriend Chiara Sassone, I would not have been able to finish this dissertation in sanity. I am very grateful for the love and patience when writing took over most of my life.

Contents

1	Introduction	1
1.1	History	1
1.2	Project objectives and background	2
1.3	Outline	5
2	Radiative Heat Transfer	9
2.1	Notation and conventions for radiative heat transfer	10
2.2	Radiative transfer equation	15
2.3	Boundary conditions	18
2.3.1	Opaque boundaries	18
2.3.2	Transparent boundaries	22
2.4	Summary	24
3	Solution methods	25
3.1	Exact solution in one dimension	26
3.1.1	Radiative heat flux	28
3.1.2	Boundary conditions	29
3.1.3	Results	35
3.2	Diffusion approximations	35
3.2.1	Rosseland Approximation	36
3.2.2	Modified Diffusion Approximation	40
3.2.3	Comparison	42
3.3	Discrete Ordinate Method	43
3.3.1	Level Symmetric Sets	45
3.3.2	Quasi-Homogeneous Sets	46
3.3.3	Conclusion	50
3.4	Other methods	51
3.4.1	Ray Tracing and Monte Carlo	52
3.4.2	Finite Element Formulation	53

4 Algebraic Ray Tracing	55
4.1 Derivation of the Algebraic Ray Tracing Method	55
4.2 Accuracy analysis	60
4.3 Implementation	65
4.3.1 One dimension	66
4.3.2 Two dimensions	70
4.3.3 Three dimensions and axisymmetric geometries	74
4.4 Examples	76
4.4.1 Square mesh	76
4.4.2 Neck ring	78
5 Reducing complexity	81
5.1 Complexity analysis	81
5.1.1 Memory consumption	81
5.1.2 Time complexity	85
5.1.3 Summary	87
5.2 Domain decomposition	87
5.2.1 Iterative solution	88
5.2.2 Direct simultaneous solution	91
5.2.3 Modified domain decomposition	94
5.3 Simplification of diffuse boundaries	96
6 Applications	101
6.1 Heat Equation	101
6.2 Parison	102
6.2.1 Dwell	104
6.2.2 Reheat	108
6.3 Neck ring cooling	112
6.3.1 Thermal equilibrium	113
6.3.2 Transient problem	116
6.3.3 Accuracy of directional discretisation	118
6.3.4 Overview of results	121
6.4 Crucible with thermocouple	122
7 Conclusion and recommendations	131

A Exponential integrals	135
Bibliography	137
Index	141
Summary	143
Samenvatting	145

Introduction

1.1 History

Glass production arguably is one of the most ancient forms of industry. Glass coated objects have been found which are date back to as early as 12,000 BC. True glass objects were already produced in Mesopotamia, present day Iraq, at the beginning of history, around 4,500 BC. The discovery of glass production was probably accidental by the right combination of the necessary ingredients: heat, soda ash, limestone (such as from sea shells) and silica sand. It is not hard to imagine these ingredients to be present at a camp fire. Surprisingly, they are still the main components in every day glass today.

The production has steadily evolved since. Undoubtedly, one of the greatest advancements was made toward the end of republican Rome when the Phoenicians developed the process of glass blowing. Soon after glass became an article of daily use throughout the Roman empire and beyond. Like the ingredients, glass blowing is still in use in the production of container glass today , although it was mechanised on a large scale at the start of the twentieth century by the press-and-blow we encounter later in this dissertation. Yet, while the production of glass is ancient, the understanding of the processes involved is relatively young. The complex chemical composition and the high temperature at which glass is processed meant understanding of glass processes had to wait for fundamental theories in those fields to be established. The lack of complete understanding notwithstanding, glass production became mechanised and quality was improved by trial and error.

Nowadays, many elements of glass production are well understood. The theoretical background for both the chemical and physical phenomena is well established. Even with the advent of computers, however, many of the processes are so complex that a complete simulation of glass production is still unthinkable at present. Yet, the glass industry is in greater need for such simulations than ever in order to optimise glass production. The rise of the polymer industry means fierce competition for glass factories in many areas. Furthermore, waking up to the notion that energy is scarce, has led governments to make stringent environmental laws. Since glass is molten at high temperatures, this brings additional challenges to the glass industry.

One aspect that adds to the complexity of simulating glass production processes, is radiative heat transfer. Because of the high temperatures at which glass is processed, radiation has to be taken into account if one wants to know the precise chemical composition, viscosity, or build-up of internal stresses. Although radiative transfer has been understood for over a century thanks to the work of Maxwell and Planck, it is associated with an inherent computational complexity that denies taking it into account accurately, for example in furnace control programs or simulations of forming processes.

The present dissertation seeks a numerical method that overcomes this complexity while remaining accurate. In the remainder of this introduction we first state the research objective and background in Section 1.2. Then, in Section 1.3, we give an outline of this dissertation and together with an overview of existing approaches.

1.2 Project objectives and background

The increase in energy costs and the growing competition between glass manufacturers and from the plastics industry as well, mean production processes need to be optimised. To achieve a reduction in energy spending, modern glass factories make use of regenerating furnaces. In recent years the furnaces are often equipped with feedback control systems that adjust furnace parameters according to measurements in the glass further down the production line. For example, temperature measurements can be made in the feeder that transports the glass melt to the forming machines; Inhomogeneities that would lead to a failed end product can often already be discovered at that early stage. To make such control systems reliable, one cannot rely on the experience of furnace operators alone. Simulation models should exist that can relate inhomogeneities inside the glass melt to furnace parameters.

Another source of costs in glass production is the high failure rate of finished products. Cracks and other defects may cause a percentage of the end products to be rejected, varying from a few percent in the container industry to a quarter in television tube production. Defects in the end product are often caused by high internal stresses which again are caused by either a sub-optimal mould design or by inhomogeneities in the glass melt that was delivered to the mould. While the glass material of such rejected end-products can be re-used, the glass needs to be molten again before it can be used. Bringing the glass back to very high temperature levels, of course, brings a high cost in energy and therefore money.

An important factor in the simulation of glass production is accurate knowledge of the temperature distribution in the glass. The temperature has a large influence on a number of parameters, such as the viscosity and the chemical composition. The computation of the temperature in glass melts, however, is complicated by a phenomenon that also forms the largest appeal of glass: it is semi-transparent. Since processing of glass occurs at very high temperatures, the glass furthermore emanates light, especially in the infrared region. The semi-transparency and the large amounts of energy emanated by the glass make treatment of radiative heat transfer essential for obtaining accurate temperature profiles. Unfortunately, the semi-transparency and the emittance of radiation

also produce a strong coupling between all points within the glass, which makes numerical computation of radiative heat transfer inherently expensive.

Radiative heat transfer has been understood fairly completely since Planck derived an expression for the radiative energy emanating from a blackbody at the start of the twentieth century; this derivation can be found in [Planck, 1923]. Still, in many simulations of glass production processes that are done at present, proper treatment of radiative heat transfer is omitted. The main reason for this omission is that many existing implementations for radiative heat transfer simulations are characterised by either high computational costs or very low accuracy. In this thesis we seek to construct a method that overcomes these shortcomings. The objective is to construct a numerical model for three-dimensional radiative heat transfer in hot glass melts, that is relatively accurate, yet efficient enough such that it can be performed on workstation class computers.

There are already a number of methods for computing radiative heat transfer. The most widely applied method in glass industry is undoubtedly the Rosseland Approximation, which is also known as the Diffusion Approximation. Rosseland, an astrophysicist, derived this method in [Rosseland, 1936], when studying radiative transfer within a star. The method has great appeal as it is one of the computationally cheapest methods to implement. Although a star has clearly a different length scale than a glass object, the method can be applied to radiation inside glass successfully if some assumptions are satisfied. The first assumption is that of so-called optical thickness. This means that the glass object should be geometrically thick or heavily absorbing infrared light. For glass furnaces and for dark glasses in feeder channels this assumption is valid, for many other applications it is not. The Rosseland Approximation further assumes that accuracy is not needed close to any boundary. Unfortunately, this is often exactly the region where we would like to know the temperature distribution accurately, as it is typically the region with the steepest temperature gradients. In [Lentes and Siedow, 1998], Siedow and Lentes proposed a Modified Diffusion Approximation that overcomes the latter drawback, although their approach still needs the assumption of optical thickness. Both methods are discussed in some detail in this thesis.

Whereas the Rosseland Approximation should be considered for optically thick objects, another approximative method can be used for optically thin objects: An often overlooked but very simple approach is to simply omit the radiative terms from the energy equation, as can be done for forming processes with clear glass. Later in this thesis, we show that in such cases the solution obtained without radiative heat transfer does not deviate much from the solution obtained with full treatment of radiative heat transfer.

Unfortunately, in glass production most processes are neither optically thick nor optically thin, but rather somewhere in between. This means that above simple approximative methods cannot be used. In that case, we cannot but solve the Radiative Transfer Equation (RTE), which is the equation that describes how the radiation changes within the domain. The RTE is a partial differential equation for the intensity, a parameter that completely describes the radiative field. The intensity is not only a function of the three spatial coordinates, but also dependent on two directional coordinates and the wavelength. The dependence on so many variables, means that it usually takes a lot of effort to compute the inten-

sity, even if it is a quantity that we are ultimately not interested in. Rather the radiative heat flux, which can be computed from the intensity, is the quantity we need in heat computations.

Most accurate models for radiation compute the intensity in one way or the other. The Ray Trace Method, which is also referred to as the Discrete Transfer Method (DTM) [Kuske, 1999, Uede et al., 2000] or Discrete Transfer Radiation Model (DTRM) [Fluent, 1999], solves the RTE along rays in a predefined number of directions. Taking an initial temperature field it redistributes the emitted radiative energy. Reflective boundaries can be implemented with ease, but result in a simple iterative approach. Furthermore, the rays need to be constructed while traversing the geometry, making the tracing itself rather expensive. The method presented in this thesis, resembles the Ray Trace Method, but avoids solving reflective boundaries iteratively, and the need to re-trace the domain for every time step in a transient heat problem. Also the Monte Carlo Method, see [Yang et al., 1995] can be placed in the same class of approaches to numerical radiative heat transfer. It is superficially similar to the Ray Trace Method, but the directions of the rays are chosen randomly rather than through the so-called Discrete Ordinate Method. Furthermore, the method traces energy packets rather than rays. This makes the method suitable for simulation of difficult physical phenomena, but even more expensive than the Ray Trace Method.

Another class of approaches solves the RTE as a partial differential equation instead of as an ordinary differential equation along a ray. In [Fiveland, 1993], the RTE is rewritten as a second order parabolic equation and solved using a Finite Element Method by using two-flux intensities rather than the intensity itself. The benefit of such an approach is that it avoids the so-called ray effect, i.e. missing phenomena at some distance from a point, because the use of a limited number of directions causes a low resolution as the rays go further away. This is important for very transparent problems such as the combustion furnace in [Limpen, 2000], but for higher values of the absorption coefficient this becomes less of an issue. Furthermore, this approach introduces a directional smoothness to the intensity that is not present in the radiative field. Finally, the formulation of arbitrary reflective boundary conditions cannot be done straightforwardly and leads to an iterative solution method when used with reflective boundaries, increasing the cost of the method. A similar method is described in [Chai and Patankar, 2000]. Chai and Patankar solve the first order RTE using a Finite Volume Method. Like the Finite Element Method, this approach avoids the ray effect at the cost of an introduced smoothness to the intensity. In the book they do not describe how to treat boundary conditions, but an iterative method seems appropriate also for this method.

The methods that we described above, all have their own forte. The latter two have clearly been derived for furnace models, where the absorption coefficient is typically low in most of the thermal spectrum. The strengths of these methods do not hold for glass media. On the other hand, the Ray Trace Method can simulate a problem of any optical thickness accurately and would be the method of choice if its associated cost would not be prohibitive. The Algebraic Ray Trace Method that we introduce and study in this thesis, overcomes some of the costs associated with that method. Furthermore, the algebraic form of the method enables derivation of additional cost saving schemes. In this dissertation, we discuss a

domain decomposition and a special treatment of diffuse boundaries, that cut down computational costs considerably.

1.3 Outline

Because the quantities describing radiative heat transfer are less commonplace than for other modes of heat transfer, we give an overview of the description of radiation and how it is related to heat transfer in Chapter 2. The chapter is split into three parts. First, Section 2.1 introduces the main quantities that describe radiation and radiative heat transfer. The all important quantity of intensity is introduced in this section. The intensity is dependent on three spatial coordinates, two coordinates describing the spatial direction under consideration, and the wavelength. The dependency of the intensity on so many variables is the first hint of the complexity associated with radiative heat transfer computations. In Section 2.2 the Radiative Transfer Equation is introduced, which describes the change in intensity throughout the domain. A detailed derivation of this equation is made in text books on radiative transfer such as [Chandrasekhar, 1960, Özişik, 1973]. Unlike radiative heat transfer in areas such as furnace design, where the medium consists of air, e.g. see [Limpens, 2000], this equation has both an absorbing part and an emitting part. This makes the heat flux at a certain point depend directly on the temperature at all other points in the domain. This is one source of the inherent complexity of radiative heat transfer in glass. Matters are further complicated by the boundary conditions to the Radiative Transfer Equation, which are described in Section 2.3. They depend on the medium as well as the material that makes up the boundary. Because they create a coupling between the intensity in different directions, they form another source for the complexity of radiative heat transfer.

Having treated the equations, we have a look at existing solution methods in Chapter 3. Section 3.1 treats a one-dimensional problem that can be solved almost completely analytically. Next to the insight this gives, it shows the general approach that leads to the Algebraic Ray Trace Method, when extended to more dimensions. In Section 3.2, we proceed with the explanation of diffusion approximations. The Rosseland Approximation derived in [Rosseland, 1936] is the classical approach for a diffusion approximation and is the most widely used method in existing simulations of glass processes. However, for simulations of glass production the assumption laying at the base of the method is often invalid. Nonetheless, because it is the fastest method for radiative transfer implemented in existing modelling software, it is often used ignoring the ramifications of the violation of the basic assumption, such as in [Robb et al., 2002]. To ameliorate the accuracy near the boundary, an improved diffusion approximation was proposed in [Lentes and Siedow, 1998], which is also discussed here. By taking special care of the boundaries, the method can be used throughout the domain with similar accuracy. For optically thin problems, i.e. problems that are either geometrically thin or very transparent, the improved Rosseland fails, too. Of course, if a problem is shown to be optically thick enough, use of a diffusion method is appropriate. The Rosseland depth that is derived in that section, can assist to determine if such an approach is sensible. Other methods for treating radiative heat transfer usually discretize the directional space, i.e. only a finite number of directions in which radiation travels, is considered. This directional discretisation is

known as the Discrete Ordinate Method which is discussed in Section 3.3. Next to the Level Symmetric Sets from [Lathrop and Carlson, 1964], that are often used, but have an awkward distribution of the weights, we present a method to obtain a quasi-homogeneous direction set. This thesis improves on that method by adjustment of the weights. In a related method in [Bressloff et al., 1995], it was shown that having a nearly homogeneous direction set improved the accuracy. Compared to the Rosseland Approximations, most other methods are more accurate but much slower. Some of these methods are briefly outlined in Section 3.4. The Ray Trace Method, which is also referred to as the Discrete Transfer Method (DTM) [Kuske, 1999, Uede et al., 2000] or Discrete Transfer Radiation Model (DTRM) [Fluent, 1999], solves the Radiative Transfer Equation exactly along rays, for a given temperature distribution. It is very well suited to treat complicated boundary conditions. However, the costs associated with this method are very high, partially because the cost of following the rays is quite high and partially because the solution is approached using a simple iterative procedure, mathematically equivalent to a Jacobi or Gauss-Seidel iteration. The method presented in this thesis is very similar to the Ray Trace Method and preserves its associated accuracy while trying to overcome its time complexity. We also discuss the method presented in [Fiveland, 1993]. Rather than solving the Radiative Transfer Equation as an ordinary differential equation along a ray, it solves an almost equivalent parabolic PDE using a Finite Element Method. Since a Finite Element Method is used to solve the underlying heat problem, this seems a logical choice. However, the modelling of boundary conditions is hard for this method and by solving an equivalent problem rather than the original problem a smoothness is introduced in the intensity distribution, both spatially and directionally.

The major problem with the more accurate methods is that their time complexity is increased by focusing on the computation of the intensity, which in the end is not the quantity we want to know. It merely appears during the computation of the heat flux. The Rosseland Approximation shows, however, that there are ways to avoid the computation of the intensity itself. In Chapter 4, which is the centrepiece of this thesis, we propose a method that is partially able to avoid the computation of the intensity everywhere. In Section 4.1, we derive the method, which we call the Algebraic Ray Trace Method, in similar way that we constructed the one-dimensional exact solution. Like (classical) Ray Tracing the method makes use of a discretized directional spacing stemming from use of the Discrete Ordinate Method. But rather than using numerical values for the emitted radiative energy, we try to capture all the operations, such as interpolations and quadratures, into a set of matrices. For the spatial discretisation it can make use of an arbitrary mesh, be-it structured be-it unstructured. This means that the mesh of the underlying heat problem can be reused and no additional work is needed to construct a separate mesh for the radiative problem. The matrices can be manipulated algebraically such that in the end only the intensity on the boundary needs to be computed explicitly. The computation of the heat flux within the domain does not need the intensity explicitly. The major benefit of this approach compared to classical Ray Tracing is that we avoid the computational-geometrical construction of the rays and their intersections with mesh elements every time we need to compute the radiative heat flux. Furthermore, any iterative method can be used to solve the reflections, which brings another speed-

up. The accuracy of the method is investigated in Section 4.2. It is found that the error scales quadratically with the size of the mesh elements. However, to make the error independent of the optical thickness special care should be taken in choosing the quadrature that is used to obtain a solution along a ray. If a standard Newton-Cotes formula is used, the error can become very large for increasing optical thicknesses. To overcome this deterioration, a different chained quadrature scheme is proposed. The chapter then continues to discuss various implementation details in Section 4.3. In the discussion of the one-dimensional implementation we compare the results with the exact solution. The two- and three-dimensional implementations focus more on the programming issues that are encountered when the ray trace method is implemented. We show how to construct a three-dimensional axisymmetric mesh from a two-dimensional description, using simplex building blocks to achieve a guaranteed accuracy. We end the chapter with the discussion of some example computations of the heat flux. One of the examples is used for a numerical error estimate.

In Chapter 5, we focus on the complexity issues of the Algebraic Ray Trace Method. At the beginning of our discussion we noted that in hot semi-transparent media, such as glass, the temperature at any point has a direct influence on every other point. This is indeed reflected in the complexity where the bottleneck is formed by a full matrix containing a number of elements roughly equal to the square of the number of nodes. In today's machines this is especially an issue for the memory requirements, but the time complexity scales similarly. In Section 5.2, we therefore propose a domain decomposition technique for the Algebraic Ray Trace Method. A straight-forward approach would result in a reduction in memory requirements, but not in the time complexity. By using a more advanced approach, where the boundaries and subdomain interfaces are treated separately from domain nodes, a linear reduction in both space and complexity can be achieved. A second bottleneck term in the complexity of the Algebraic Ray Trace Method, is formed when large parts of the boundary are diffusely reflective. In Section 5.3, we show how to use the matrix representation of the ray trace procedure to arrive at a formulation for all diffuse boundaries that squashes this complexity.

After this extensive discussion of the Algebraic Ray Trace Method, we treat various examples of heat problems in Chapter 6 to assess the Algebraic Ray Trace Method. In Section 6.2, we deal with a one-dimensional model for the heat transfer in a bottle-like shape during various stages of the forming process. The example serves as a comparison between the quality of various methods. It clearly shows that the Rosseland Approximation is not the best choice for such optically non-thick geometries. For these geometries, leaving out radiation from the heat equation gives much better results. It is often not realised that for optically thin geometries radiation does not play an all-important role and that inclusion of radiative heat transfer is not necessary. This means, that for forming processes with clear glasses, the heat equation can be treated with only linear diffusion. Hence, it is easier to experiment with different solvers for the forming itself as was done for example in [Wang, 2002]. In Section 6.3, we look at these processes for an axisymmetric model for the top of a jar. Both steady and transient heat problems are considered. The example is furthermore used to study the numerical accuracy of the directional discretisation obtained by the Discrete Ordinated Method. In Section 6.4, the final example deals with a problem with more com-

plicated boundary conditions: a crucible with a thermocouple immersed in glass. The results of the computation show the expected inaccuracy of thermocouple measurements in glass. Because they change the radiative field, they cannot measure the temperature and its gradients accurately.

Finally, in Chapter 7 we give a short summary of findings made in this thesis. Furthermore, we provide a small overview of which method is applicable to which problem in glass manufacturing.

Radiative Heat Transfer

Processing of glass occurs at elevated temperatures. First the batch products, such as for example silica sands, limestone and soda, are melted in a furnace at temperatures as high as 1600°C. Looking into the furnace, you will see a bright yellow light coming out. The molten glass is transferred to the forming machines where the products are formed at temperatures of 800–1000°C, the half-products emitting a faint orange light. To make the glass stronger and to reduce internal stresses caused by cooling and forming, the products then are cooled slowly in an annealing lehr. By this time the products do not emit any visible light anymore, but the heat can still be felt from a distance.

The fact that heat can be felt from a distance — and that the glass material actually emits light — means that heat is also transferred by radiation. Thermal radiation occurs mostly in the infrared region of the electro-magnetic spectrum with wavelengths ranging from 750 nm to 1000 μm . Only at higher temperatures, there is a strong shift into the visible part of the spectrum, with wavelengths less than 750 nm.

Another special feature of glass is the fact that it is transparent: light travels through the glass. In fact glass is *semi-transparent* in the infrared and visible regions of the spectrum: it does not let all the light go through, it also absorbs a part and, as can be seen from the oven, it also emits significant amounts of light at high temperatures.

Shown below, thermal radiation scales with temperature as T^4 , meaning it becomes progressively more important as temperatures go higher. Since many important characteristics of glass, such as its viscosity and chemical reactions, which can cause foaming and affect the redox state, are strongly dependent on temperature, we have to take thermal radiation into account.

In this chapter, we investigate how the radiative heat transfer can be calculated. First, we define the notion of intensity — which completely describes the thermal radiation — and derived quantities that give information about the radiative field. In the second section, a conservation law is derived for the intensity that allows us to compute the intensity. Finally, the third section explains the treatment of boundaries.

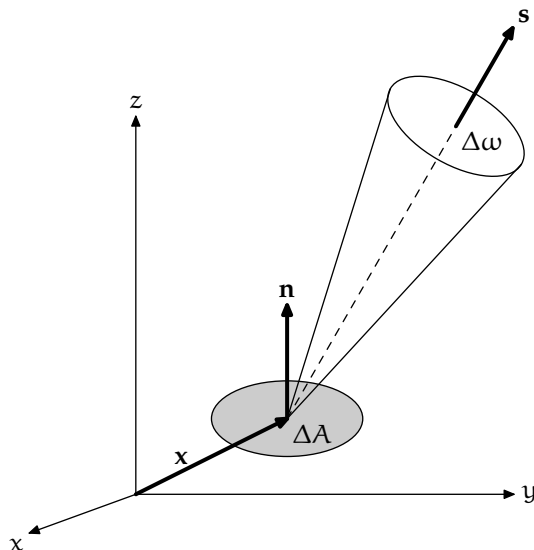


Figure 2.1: Geometric situation for the description of spectral intensity.

2.1 Notation and conventions for radiative heat transfer

Electro-magnetic radiation has a dual character. After millennia of discussion whether light consists of particles or waves, Maxwell's formulation of the electro-magnetic equations that carry his name seemed to settle the debate in favour of the wave nature in the second half of the nineteenth century. Less than fifty years later, however, Planck formulated the first law of physics, that laid the basis for quantum mechanics. Furthermore, he suggested that light consists of particles or energy quanta.

At the temperature range where glass production takes place — ranging from room temperature to a couple of thousands degrees — and the length scale of the problems — from millimetres to metres — the Maxwell equations provide an accurate basis to describe thermal radiation. For microscopic local quantities, however, such as the spontaneous emission of radiation due to temperature, results from quantum mechanics can be used. Referring to [Chandrasekhar, 1960], [Mihalas and Weibel-Mihalas, 1984], and [Özişik, 1973] for a more detailed description, it can be deduced from the Maxwell equations that a single scalar quantity suffices to describe unpolarised radiation in a dielectric medium: the *intensity*. Since glass is mostly dielectric and natural radiation, such as emission because of temperature, is unpolarised we can use the intensity for our treatment of radiation.

For a physical interpretation of the intensity, Figure 2.1 shows a small surface ΔA , at a point \mathbf{x} with a local normal vector \mathbf{n} where radiation passes through in the direction \mathbf{s} . If we consider *monochromatic* radiation — i.e. radiation at one specific electro-magnetic frequency — the monochromatic intensity $I_\nu(\mathbf{x}, \mathbf{s})$ can be defined as the amount of radiative energy ΔE_ν in the frequency range $(\nu, \nu + \Delta\nu)$ that passes through a cone with spherical angle $\Delta\omega$ around direction

\mathbf{s} . Since the area of the small surface projected on a plane perpendicular to \mathbf{s} is $\Delta A' = \Delta A \cos \vartheta$, where ϑ is the angle between the surface normal and the direction of the intensity, we can define the monochromatic intensity as

$$I_\nu(\mathbf{x}, \mathbf{s}) := \lim_{\Delta A, \Delta t, \Delta \nu, \Delta \omega \rightarrow 0} \frac{\Delta E_\nu(\mathbf{x}, \mathbf{s})}{\Delta A' \Delta t \Delta \nu \Delta \omega}, \quad (2.1)$$

taken over a period Δt . If not a plane but a small volume at point \mathbf{x} is taken as the source, $\Delta A'$ is equal to the frontal area of that volume with respect to direction \mathbf{s} . The unit of intensity is $\text{W m}^{-2} \text{sr}^{-1} \text{Hz}^{-1}$. Rather than being a completely abstract quantity, (2.1) shows that the intensity is suitable for experimental acquisition.

One occurrence of the intensity has been of special interest to science: the emissive spectrum of a so-called *blackbody*. A blackbody is a perfect absorber of radiation, i.e. it absorbs all incoming radiation from all directions and of any frequency, without any reflection or transmission. If such a body is put into an isothermal enclosure which emits and absorbs radiation, it has to emit the same amount of radiative energy as it absorbs, when it is in thermal equilibrium. Since there is no type of body that absorbs more intensity than a blackbody, it can be concluded that the emission of radiation, too, is maximised by a blackbody.

At the end of the nineteenth century two different formulae for this intensity were known as Wien's Law and the Rayleigh-Jeans Law. However, measurements showed that while these formulae were accurate in a specific part of the spectrum, they failed to predict the intensity universally. Planck then proceeded by improving upon these equations, by first deriving an expression for the entropy in terms of the energy, as can be found in [Planck, 1923]. Interestingly, for this new formulation Planck had to assume that there were only a finite number of energy states; thereby introducing quantum mechanics at the start of the twentieth century.

For the intensity of monochromatic radiation emitted by a blackbody at temperature T , Planck found the following:

$$B_\nu(T) = \frac{n_\nu^2}{c_0^2} \frac{2h\nu^3}{e^{h\nu/(k_B T)} - 1}, \quad (2.2)$$

where the function $B_\nu(T)$ is usually referred to as the *monochromatic blackbody intensity* or the *Planck function*. The physical constants are denoted with $h := 6.62608 \cdot 10^{-34} \text{ J s}$ for the Planck constant, $k_B := 1.38066 \cdot 10^{-23} \text{ J/K}$ for the Boltzmann constant, and n_ν for the *refractive index*, which is defined as the ratio of the speed of light in vacuum and within the medium:

$$n_\nu := \frac{c_0}{c}. \quad (2.3)$$

The refractive index is a material property, which is mostly influenced by the chemical composition of the medium. In general it depends on the frequency of the radiation as well as the temperature of the medium, which of course influences the chemical composition by reactions. The dependence on temperature and frequency, however, is very weak. The refractive index is often measured at a specific wavelength and at a specific temperature; see [Beerkens et al., 1997]. Here, it is assumed that the refractive index is a constant for a given problem for the remainder of this dissertation.

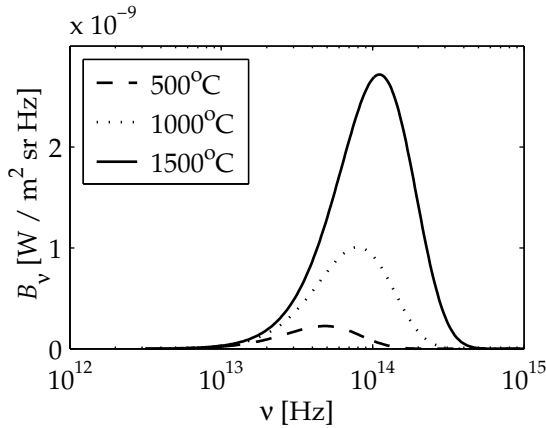


Figure 2.2: Distribution of the monochromatic blackbody intensity in the infrared range in glass at various temperatures.

If indeed the refractive index is independent of the electro-magnetic frequency, (2.2) can be integrated over all frequencies to find the total blackbody intensity:

$$B(T) = n^2 \frac{\bar{\sigma} T^4}{\pi}, \quad (2.4)$$

where $\bar{\sigma} := 5.67051 \cdot 10^{-8} \text{ W/K}^4\text{m}^2$ is the Stefan-Boltzmann constant, which is the collection of terms following from the integration of (2.2):

$$\bar{\sigma} := \frac{2\pi k_B^4}{15c_0^2 h^3}. \quad (2.5)$$

Since the temperature T itself depends on the position \mathbf{x} , and in many radiation equations the temperature does not appear by itself, we introduce the notation

$$B(\mathbf{x}) := B(T(\mathbf{x})), \quad (2.6)$$

if no confusion can arise. It should always be realised, however, that the blackbody intensity is a function of the position, purely because of the temperature at that position.

In Figure 2.2 the monochromatic blackbody intensity is shown for various temperatures in a glass medium with $n = 1.47$. Only the infrared part of the spectrum is shown. From the figure, it is clear that radiation becomes progressively more important with increasing temperature. Furthermore, we note that the frequency where the maximal intensity occurs, becomes higher with increasing temperature. This is the reason that thermal radiation can be seen at higher temperatures, while only be felt at lower ones.

Although the intensity describes thermal radiation completely, it is not the quantity we are ultimately interested in. In general, when problems involving hot or molten glass are considered, the heat equation is used in the following form:

$$c_v \rho \frac{DT}{Dt} = -\nabla \cdot \mathbf{q}_c - \nabla \cdot \mathbf{q}_r + Q, \quad (2.7)$$

where we have used c_v for the specific heat of the medium, ρ as the density, T for the temperature, t for the time, and Q for all other sources of heat, e.g. by viscous dissipation or chemical reactions. The *conductive heat flux* \mathbf{q}_c is determined by Fourier's Law:

$$\mathbf{q}_c = k_c(T)\nabla T, \quad (2.8)$$

where k_c is the *thermal conductivity* or *Fourier diffusion coefficient*, which itself can be — and usually is — depending on temperature. The last term in (2.7), \mathbf{q}_r , is the *radiative heat flux*. This quantity refers to the radiation that is emitted by the glass or any other medium. So, to use the intensity in glass applications we need to write it in a form $\nabla \cdot \mathbf{q}_r$, i.e. there needs to be a relation between the intensity and the divergence of the heat flux.

Before we can write down such a relation, we have to introduce various other concepts. As the divergence of the heat flux is a property that does not depend on direction, an integration over all directions is implied. In fact when we integrate the intensity over all directions with different powers of the elements of the direction vector \mathbf{s} , several other quantities with a physical meaning are obtained. To facilitate the definition of the various moments of the intensity, we start by introducing several direction spaces together with operators that perform integration over those spaces.

The space of all directions is given by the unit sphere. Here, this space is denoted by \mathbb{S}_2 :

$$\mathbb{S}_2 := \{\mathbf{s} \mid \mathbf{s} \in \mathbb{R}^3 \wedge \|\mathbf{s}\| = 1\}. \quad (2.9)$$

Although elements from this space are three-dimensional vectors, the space itself has only two dimensions. The integration over all directions, later also referred to by the operator W , can be rewritten in spherical coordinates as:

$$(Wf)(\mathbf{x}) := \int_{\mathbb{S}_2} f(\mathbf{x}, \mathbf{s}) d\omega = \int_{\varphi=-\pi}^{\pi} \int_{\vartheta=0}^{\pi} f(\mathbf{x}, \varphi, \vartheta) \sin \vartheta d\vartheta d\varphi. \quad (2.10)$$

When treating boundaries, we are usually not so much interested in radiation in all directions, but rather in either incoming or outgoing radiation. To that end, we define the following two hemispherical spaces with respect to some normal vector \mathbf{n} :

$$\mathbb{H}^+(\mathbf{n}) := \{\mathbf{s} \mid \mathbf{s} \in \mathbb{S}_2 \wedge \mathbf{s} \cdot \mathbf{n} > 0\} \quad (2.11)$$

$$\mathbb{H}^-(\mathbf{n}) := \{\mathbf{s} \mid \mathbf{s} \in \mathbb{S}_2 \wedge \mathbf{s} \cdot \mathbf{n} < 0\}, \quad (2.12)$$

where we omit the dependency on the normal, if there is no confusion. For completeness, a third space is defined as

$$\mathbb{H}^0(\mathbf{n}) := \{\mathbf{s} \mid \mathbf{s} \in \mathbb{S}_2 \wedge \mathbf{s} \cdot \mathbf{n} = 0\}, \quad (2.13)$$

so $\mathbb{H}^+ \cup \mathbb{H}^0 \cup \mathbb{H}^- = \mathbb{S}_2$. Finally, we define the closed versions of the hemispherical spaces as

$$\mathbb{H}_0^+ := \mathbb{H}^+ \cup \mathbb{H}^0, \quad (2.14)$$

$$\mathbb{H}_0^- := \mathbb{H}^- \cup \mathbb{H}^0. \quad (2.15)$$

To indicate integration over these hemispherical spaces we introduce the operators $W_{\mathbf{n}}^+$ and $W_{\mathbf{n}}^-$, defined by

$$(W_{\mathbf{n}}^+ f)(\mathbf{x}) := \int_{\mathbb{H}^+(\mathbf{n})} f(\mathbf{x}, \mathbf{s}) d\omega, \quad (2.16)$$

$$(W_{\mathbf{n}}^- f)(\mathbf{x}) := \int_{\mathbb{H}^-(\mathbf{n})} f(\mathbf{x}, \mathbf{s}) d\omega. \quad (2.17)$$

Again, if it is clear from the context which normal vector is intended, the index specifying the normal is dropped. The notation using operators proves useful in clarifying the similarity between analytical and numerical solution methods in later chapters.

Integration of the intensity over these spaces and application of different weight functions leads to various other physical quantities. The zeroth moment of the intensity gives the total amount of radiative energy in every direction that passes through a point. This quantity $G_{\nu}(\mathbf{x})$ is called *spectral incident radiation* and is defined by

$$G_{\nu}(\mathbf{x}) := \int_{\mathbb{S}_2} I_{\nu}(\mathbf{x}, \mathbf{s}) d\omega. \quad (2.18)$$

If the total amount of radiation for all wavelengths is needed, we need to integrate over all frequencies to find the *total incident radiation*

$$G(\mathbf{x}) := \int_{\nu=0}^{\infty} G_{\nu}(\mathbf{x}) d\nu. \quad (2.19)$$

Other forms of this quantity include mean intensity \bar{I}_{ν} and the *spectral radiative energy density* $u_{\nu}(\mathbf{x})$. They are related as follows

$$4\pi\bar{I}_{\nu}(\mathbf{x}) = cu_{\nu}(\mathbf{x}) = G_{\nu}(\mathbf{x}), \quad (2.20)$$

where we have used c for the speed of light in the medium. If the intensity is not equal in all directions, there is a net transport of radiative heat. This is the first moment of the intensity, which is the *spectral radiative heat flux* that we sought. Because of the definition of $I(\mathbf{x}, \mathbf{s})$, it can be constructed by

$$\mathbf{q}_{\nu}(\mathbf{x}) = \int_{\mathbb{S}_2} \mathbf{s} I_{\nu}(\mathbf{x}, \mathbf{s}) d\omega. \quad (2.21)$$

Since this again refers to a specific wavelength, we first need to integrate over all frequencies to obtain the *(total) radiative heat flux*, which we can use in the heat equation (2.7):

$$\mathbf{q}_r(\mathbf{x}) := \int_{\nu=0}^{\infty} \mathbf{q}_{\nu}(\mathbf{x}) d\nu. \quad (2.22)$$

Finally, we introduce the second moments, collected in the *radiation tensor* $\mathbf{P}_{\nu} = (p_{\nu,ij})$, of which the elements are defined by

$$p_{\nu,ij} := \int_{\mathbb{S}_2} s_i s_j I_{\nu}(\mathbf{x}, \mathbf{s}) d\omega, \quad (2.23)$$

where the i -th and j -th component of the direction vector \mathbf{s} are considered. They get a physical meaning after division by the speed of light: the tensor defined as

$$\sigma_{\nu}(\mathbf{x}) := \frac{1}{c} \mathbf{P}_{\nu}(\mathbf{x}), \quad (2.24)$$

represents the *spectral radiative stress tensor*. Because of the transmission of momentum when photons are absorbed or emitted by the medium, radiation exerts a force on the medium. If the intensity is independent of the direction, only the diagonal elements in these tensors remain; they then are all equal to

$$p_{\nu,ii} = \frac{1}{3}G_{\nu}(\mathbf{x}), \quad \text{and} \quad \sigma_{\nu,ii} = \frac{1}{3}u_{\nu}(\mathbf{x}), \quad (2.25)$$

which means that the radiation only exerts an isotropic pressure. In the processes seen in glass production this force is negligible; yet the tensor \mathbf{P}_{ν} proves itself useful in the derivation of diffusion approximations below.

2.2 Radiative transfer equation

As we saw in the previous section, the intensity completely describes thermal radiation in every point. The radiative heat flux, its divergence and other properties are all derived from this intensity. So, in order to completely describe the behaviour of radiative heat transfer, we need to know the behaviour of the intensity in the domain.

Since the notion of intensity is closely related to the flow of energy in a specific direction, we can look at the energy balance in a point. Such an analysis leads to a description of the change in intensity. Here, we first have a closer look at the absorption and emission in an infinitesimal volume element, and then collect the energy balance into the so-called Radiative Transfer Equation.

As radiation travels through a semi-transparent medium, a part of the radiative energy is absorbed by the medium. Considering a volume element with frontal area ΔA and depth Δs , suppose that an amount ΔE_{ν} of monochromatic radiative energy from a beam with solid angle $\Delta\omega$ around direction \mathbf{s} is absorbed by the volume during a period Δt . Then the *spectral volumetric absorption coefficient* is defined by

$$\kappa_{\nu}(\mathbf{x}, \mathbf{s}) := \lim_{\Delta t, \Delta A, \Delta s, \Delta \nu, \Delta \omega \rightarrow 0} \frac{\Delta E_{\nu}(\mathbf{x}, \mathbf{s})}{\Delta t \Delta A \Delta s \Delta \nu} \frac{1}{I_{\nu}(\mathbf{x}, \mathbf{s}) \Delta \omega} = \frac{1}{I_{\nu}(\mathbf{x}, \mathbf{s})} \frac{d\Phi_{\nu,a}}{d\omega}(\mathbf{x}, \mathbf{s}), \quad (2.26)$$

where we used $\Phi_{\nu,a}$ for the monochromatic absorption rate. If the material is isotropic — as is most likely in molten glass — the absorption coefficient is independent of the direction. The absorption rate per beam follows directly from the definition of the absorption coefficient

$$\frac{d\Phi_{\nu,a}}{d\omega}(\mathbf{x}, \mathbf{s}) = \kappa_{\nu}(\mathbf{x}) I_{\nu}(\mathbf{x}, \mathbf{s}). \quad (2.27)$$

This quantity is used below in the derivation of a conservation law for the intensity. The total absorption from all directions by the volume element can be computed from

$$\Phi_{\nu,a}(\mathbf{x}) = \int_{\mathbb{S}_2} \kappa_{\nu}(\mathbf{x}) I_{\nu}(\mathbf{x}, \mathbf{s}) d\omega = \kappa_{\nu}(\mathbf{x}) G_{\nu}(\mathbf{x}). \quad (2.28)$$

Note, that that the latter states that the absorption rate of an absorbing volume element can be completely expressed in isotropic quantities. For simplified

analyses, it is sometimes furthermore assumed that the absorption coefficient is independent of frequency. A medium with such an absorption coefficient is called a *grey medium*.

As semi-transparent media only partially absorb radiation, they cannot be classified as perfect blackbodies. As shown in [Mihalas and Weibel-Mihalas, 1984], under assumption of *local thermal equilibrium* and the validity of Kirchhoff's Law, it can be derived that the directional emission rate is linearly related to the blackbody intensity:

$$\frac{d\Phi_{\nu,e}}{d\omega}(\mathbf{x}, \mathbf{s}) = \kappa_{\nu}(\mathbf{x})B_{\nu}(\mathbf{x}). \quad (2.29)$$

Since both the absorption coefficient and the blackbody intensity are isotropic, the total spectral emissive power of a volume element is given by

$$\Phi_{\nu,e}(\mathbf{x}, \mathbf{s}) = 4\pi\kappa_{\nu}(\mathbf{x})B_{\nu}(\mathbf{x}). \quad (2.30)$$

The third phenomenon that may occur is *scattering*. Scattering is the phenomenon that a part of the radiative energy in a beam in a particular direction is redistributed over beams in other directions. During glass production scattering occurs in two stages. The first is when the batch products enter the furnace. As long as the elements in this batch are not completely molten, they represent small spherical particles, that redistribute the intensity, much alike water droplets in clouds do with sun light. The other example of scattering in glass production is in the presence of gas bubbles in the glass melt. These bubbles, too, redistribute the radiative energy.

However, in most processes no such scattering is present. Furthermore, in the cases mentioned above, scattering is so predominant that other models such as the Rosseland Approximation presented in Section 3.2.1, represent a very accurate representation of reality. It is for these considerations, that treatment of scattering is omitted altogether.

A mathematical formulation for the change in intensity, now can be found by making an energy balance for the particle under consideration. The change of the intensity in a beam going in direction \mathbf{s} through a volume at \mathbf{x} with frontal area dA and depth ds , is found as the difference between emission and absorption:

$$\frac{dI_{\nu}}{ds} = \frac{d\Phi_{\nu,e}}{d\omega} - \frac{d\Phi_{\nu,a}}{d\omega}. \quad (2.31)$$

After substitution of (2.27) and (2.29) in this equation we find that

$$\mathbf{s} \cdot \nabla I_{\nu}(\mathbf{x}, \mathbf{s}) + \kappa_{\nu}(\mathbf{x})I_{\nu}(\mathbf{x}, \mathbf{s}) = \kappa_{\nu}(\mathbf{x})B_{\nu}(\mathbf{x}). \quad (2.32)$$

This equation is called the *radiative transfer equation* or RTE. It proves useful to interpret this equation as a change in intensity along a curve:

$$\frac{dI_{\nu}}{ds}(\mathbf{x}_0 + \zeta\mathbf{s}, \mathbf{s}) + \kappa_{\nu}I_{\nu}(\mathbf{x}_0 + \zeta\mathbf{s}, \mathbf{s}) = \kappa_{\nu}B_{\nu}(\mathbf{x}_0 + \zeta\mathbf{s}), \quad (2.33)$$

where ζ is the distance along the curve. Due to the work of medieval Alhazen, see [Alhazen, 1270], and of Willebrord Snell, which was published by Huygens in [Huygens, 1690], we know that these curves are straight lines if the refractive index n is constant within the medium. In this form, we can integrate the

equation from a point \mathbf{x}_Γ on the boundary to the point of interest \mathbf{x}_0 along the ray going in direction \mathbf{s} . The boundary point \mathbf{x}_Γ where we start the integration, is a function of both \mathbf{x}_0 and \mathbf{s} and should be found first. The initial condition for the intensity at the boundary is itself an unknown, which is denoted here by $I_{\Gamma,\nu}(\mathbf{x}_\Gamma, \mathbf{s})$. How this boundary intensity can be obtained is discussed in the next section. Solving the RTE without knowledge of blackbody intensity B_ν nor the boundary intensity $I_{\Gamma,\nu}$, gives us a so-called *formal solution*:

$$I_\nu(\mathbf{x}_0, \mathbf{s}) = e^{-\kappa_\nu \|\mathbf{x}_0 - \mathbf{x}_\Gamma\|} I_{\Gamma,\nu}(\mathbf{x}_\Gamma, \mathbf{s}) + \int_0^{\|\mathbf{x}_0 - \mathbf{x}_\Gamma\|} \kappa_\nu e^{-\kappa_\nu \zeta} B_\nu(\mathbf{x}_0 - \zeta \mathbf{s}) d\zeta. \quad (2.34)$$

The fact that we can straightforwardly solve the intensity along a ray lays at the base of a numerical solution method called the *ray trace method* discussed in Section 3.4.1 and its algebraic form, which forms the centrepiece of this dissertation and is discussed in detail in Chapter 4.

The RTE can be simplified by choosing a different coordinate system. If we define the *optical distance* τ along a ray through

$$d\tau = \kappa_\nu ds, \quad (2.35)$$

the RTE simplifies to

$$\frac{dI_\nu}{d\tau} + I_\nu = B_\nu. \quad (2.36)$$

From this simplification it follows that for radiative heat transfer not the spatial dimensions determine the solution, but rather the optical dimensions. This means problems can be characterised by the *optical thickness* of the problem, which for every spectral line is defined as

$$\tau_0 = \kappa_\nu L, \quad (2.37)$$

where L is some characteristic length of the problem, and κ_ν was assumed to be constant within the domain. As shown in Section 3.2.1, different approximations can be made for the cases where the geometry is optically thick ($\tau_0 \gg 1$), optically thin ($\tau_0 \ll 1$) and the case in between. Typically, problems in glass simulations are neither optically thin nor optically thick, which disqualifies some major simplifications. This is discussed in more detail in Section 3.2.

Although radiative heat transfer is completely described by the intensity, we are interested in the total effect on the radiative heat flux. For the divergence of the heat flux of the volume element, which represents the rate of cooling in absence of other heat transfer modes, it holds that

$$\nabla \cdot \mathbf{q}_\nu = \Phi_{\nu,e} - \Phi_{\nu,a}, \quad (2.38)$$

which after substitution becomes

$$\nabla \cdot \mathbf{q}_\nu = 4\pi\kappa_\nu B_\nu - \kappa_\nu G_\nu = 4\pi\kappa_\nu (B_\nu - \bar{I}_\nu). \quad (2.39)$$

This implies that we do not need to know the intensity in every direction, but rather the average intensity in order to compute the divergence of the heat flux. Consequently, in the search of solution methods we should try to avoid the factual computation of the intensity, and try to find the average instead.

2.3 Boundary conditions

Since (2.32) is a first order ordinary differential equation, we need to specify a single boundary condition. Let Ω be the geometric domain of interest, which is assumed to have a finite volume. Furthermore, let Γ be its boundary such that $\Gamma \cap \Omega = \emptyset$. For convenience of notation, let any arbitrary entity $E(\mathbf{x})$, defined on Ω , be extended to the boundary, such that

$$E(\mathbf{x}_\Gamma) := \lim_{\mathbf{x} \rightarrow \mathbf{x}_\Gamma} E(\mathbf{x}), \quad \text{with } \mathbf{x}_\Gamma \in \Gamma, \text{ and } \mathbf{x} \in \Omega. \quad (2.40)$$

Since the rays along which (2.32) can be solved are straight lines, they all intersect the boundary and have a constant direction. This means, that we can define an injective projection $p_\Gamma(\mathbf{x}, \mathbf{s})$ that associates any point-direction pair (\mathbf{x}, \mathbf{s}) in $\Omega \times \mathbb{S}_2$ with some point \mathbf{x}_Γ on Γ . More specifically, it gives the first intersection with the boundary, when we follow a line from point \mathbf{x} in direction $-\mathbf{s}$. Thus, the boundary condition to the RTE can be written as

$$I_\nu(\mathbf{x}_\Gamma, \mathbf{s}) = I_{\Gamma, \nu}(\mathbf{x}_\Gamma, \mathbf{s}), \quad \mathbf{x}_\Gamma = p_\Gamma(\mathbf{x}, \mathbf{s}), \quad (2.41)$$

where $I_{\Gamma, \nu}(\mathbf{x}_\Gamma, \mathbf{s})$ is the intensity at the boundary. Note that if n was not assumed to be a constant and rays would be curves, the possibility would exist that a ray never crosses the geometric boundary. In such a hypothetical case, boundary conditions to (2.32) would have to be specified within the domain. Although a closed system could be created mathematically, obtaining such data physically would be impossible.

2.3.1 Opaque boundaries

The boundary radiation $I_{\Gamma, \nu}(\mathbf{x}_\Gamma)$ depends on the physical-optical properties of the boundary. The most simple case is presented when the boundaries behave as perfect *black boundaries*, i.e. the boundaries behave as perfect emitters/absorbers. In that case, the intensity emitted by the boundary is a direct function of the temperature of the boundary using Planck's function:

$$I_{\Gamma, \nu}(\mathbf{x}_\Gamma) = B_{\Gamma, \nu}(\mathbf{x}_\Gamma) := B_\nu(T_w(\mathbf{x}_\Gamma)), \quad (2.42)$$

where T_w is the *wall temperature* and $B_{\Gamma, \nu}$ is the blackbody intensity generated at this temperature. As is shown below for the one-dimensional case, absence of conduction in general means that the temperature of the medium close to the wall is different from the temperature of the wall itself.

Although boundaries modelled as perfectly black surfaces provide simple boundary conditions, they are often not the best model for physical boundaries. An opaque boundary absorbs and emits radiative heat, but also reflects incident radiation. To study the reflection, let \mathbf{n}_Γ be the normal of the boundary surface at point \mathbf{x}_Γ pointing into the domain. Then the amount of radiative energy arriving at the surface per unit time, per unit area, and per unit frequency is given by

$$g'_\nu(\mathbf{x}_\Gamma, \tilde{\mathbf{s}}) d\tilde{\omega} := I_\nu(\mathbf{x}_\Gamma, \tilde{\mathbf{s}}) \cos \tilde{\vartheta} d\tilde{\omega}, \quad (2.43)$$

where we have introduced the convention by marking directions and angles referring to incoming radiation with a tilde. The total amount of radiative energy

incident to the surface is called the *spectral irradiance*. It is defined by

$$G'_\nu(\mathbf{x}_\Gamma) := \int_{\mathbb{H}^-} I_\nu(\mathbf{x}_\Gamma, \tilde{\mathbf{s}}) \cos \tilde{\vartheta} \, d\tilde{\omega}. \quad (2.44)$$

Here, we used $\tilde{\mathbf{s}}$ to specify the direction of the incident radiation; $\tilde{\mathbf{s}}$ lies on the hemisphere defined by $\tilde{\mathbf{s}} \cdot \mathbf{n}_\Gamma \leq 0$. Furthermore, $d\tilde{\omega}$ is an infinitesimal spherical angle around $\tilde{\mathbf{s}}$ on this hemisphere. Finally, $\tilde{\vartheta}$ is the angle between $\tilde{\mathbf{s}}$ and $-\mathbf{n}_\Gamma$:

$$\tilde{\vartheta} := \pi - \arccos(\tilde{\mathbf{s}} \cdot \mathbf{n}_\Gamma). \quad (2.45)$$

Similarly, the total amount of radiative energy that is leaving the surface into the domain is called the (*spectral*) *radiosity*, and is defined by:

$$J'_\nu(\mathbf{x}_\Gamma) := \int_{\mathbb{H}^+} I_\nu(\mathbf{x}_\Gamma, \mathbf{s}) \cos \vartheta \, d\omega, \quad (2.46)$$

where ϑ is the angle between the direction of intensity and the normal proper. The fraction of the incident energy that is reflected by the surface is specified by the *spectral reflection distribution function* $\varphi_\nu(\mathbf{x}_\Gamma, \tilde{\mathbf{s}}, \mathbf{s})$, defined by

$$\varphi_\nu(\mathbf{x}_\Gamma, \tilde{\mathbf{s}}, \mathbf{s}) := \frac{1}{I_\nu(\mathbf{x}_\Gamma, \tilde{\mathbf{s}}) \cos \tilde{\vartheta}} \frac{dI_\nu(\mathbf{x}_\Gamma, \mathbf{s})}{d\tilde{\omega}}. \quad (2.47)$$

We can use this distribution to calculate the contribution of the reflection to the intensity in direction \mathbf{s} :

$$I_{\Gamma, \nu, \text{reflection}}(\mathbf{x}_\Gamma, \mathbf{s}) = \int_{\mathbb{H}^-} \varphi_\nu(\mathbf{x}_\Gamma, \tilde{\mathbf{s}}, \mathbf{s}) I_\nu(\mathbf{x}_\Gamma, \tilde{\mathbf{s}}) \cos \tilde{\vartheta} \, d\tilde{\omega}. \quad (2.48)$$

The distribution φ_ν is a characteristic property of the interaction between the semi-transparent medium and the opaque boundary and should be obtained by measurements. Note, that it does not deal with cross-spectral reflections, i.e. when the reflected radiation has a different frequency as the incident radiation. As done with the refractive index, we use lack of measurement data to justify our assumption of *monochromatic reflections*: we assume that all radiative energy incident to a boundary surface is reflected with the same frequency.

Obtaining the complete distribution by experimentation is often hard. Therefore, two other, related, distributions are used. The first one specifies the fraction of the incident radiation that is reflected in any direction and is called the *spectral directional-hemispherical reflectivity*. It is defined by

$$\rho_\nu(\mathbf{x}_\Gamma, \tilde{\mathbf{s}} \rightarrow \mathbb{H}^+) := \int_{\mathbb{H}^+} \frac{1}{I_\nu(\mathbf{x}_\Gamma, \tilde{\mathbf{s}}) \cos \tilde{\vartheta}} \frac{\cos \vartheta \, dI_\nu(\mathbf{x}_\Gamma, \mathbf{s})}{d\tilde{\omega}} \, d\omega, \quad (2.49)$$

where we used ϑ for the angle between the normal and the outgoing direction, so $\cos \vartheta := \mathbf{n}_\Gamma \cdot \mathbf{s}$. It is related to the reflection distribution function through

$$\rho_\nu(\mathbf{x}_\Gamma, \tilde{\mathbf{s}} \rightarrow \mathbb{H}^+) := \int_{\mathbb{H}^+} \varphi_\nu(\mathbf{x}_\Gamma, \tilde{\mathbf{s}}, \mathbf{s}) \cos \vartheta \, d\omega. \quad (2.50)$$

This distribution can be measured by letting a beam of monochromatic radiation fall onto a surface, and measure the increase in energy over an entire hemisphere

over the surface. If instead, the increase in radiative energy of a specific beam leaving the surface is measured, the so-called *hemispherical-directional reflectivity* is obtained. This is defined by

$$\rho_{\nu}(\mathbf{x}_{\Gamma}, \mathbb{H}^{-} \rightarrow \mathbf{s}) := \frac{\int_{\mathbb{H}^{-}} \varphi_{\nu}(\mathbf{x}_{\Gamma}, \tilde{\mathbf{s}}, \mathbf{s}) I_{\nu}(\mathbf{x}_{\Gamma}, \tilde{\mathbf{s}}) \cos \tilde{\vartheta} \, d\tilde{\omega}}{\frac{1}{\pi} \int_{\mathbb{H}^{-}} I_{\nu}(\mathbf{x}_{\Gamma}, \tilde{\mathbf{s}}) \cos \tilde{\vartheta} \, d\tilde{\omega}}. \quad (2.51)$$

By its definition, we see directly how we can use this reflectivity to compute the contribution of reflection to the outgoing intensity:

$$I_{\Gamma, \nu, \text{reflection}}(\mathbf{x}_{\Gamma}, \mathbf{s}) = \frac{1}{\pi} \rho_{\nu}(\mathbf{x}_{\Gamma}, \mathbb{H}^{-} \rightarrow \mathbf{s}) G'_{\nu}(\mathbf{x}_{\Gamma}). \quad (2.52)$$

This distribution depends on the directional distribution of the incoming radiation, so a measured hemispherical-directional reflectivity is only valid for problems where the radiative field has the same shape. However, often it is assumed that the incoming intensity does not vary with direction, i.e. $I_{\nu}(\mathbf{x}_{\Gamma}, \tilde{\mathbf{s}}) = G'_{\nu}(\mathbf{x}_{\Gamma})/\pi$, for all incoming directions $\tilde{\mathbf{s}}$. For the approximated hemispherical-directional reflectivity we then find the relation

$$\rho_{\nu}(\mathbf{x}_{\Gamma}, \mathbb{H}^{-} \rightarrow \mathbf{s}) = \rho_{\nu}(\mathbf{x}_{\Gamma}, \tilde{\mathbf{s}} \rightarrow \mathbb{H}^{+}), \quad (2.53)$$

where \mathbf{s} and $\tilde{\mathbf{s}}$ satisfy $\mathbf{s} + \tilde{\mathbf{s}} = \mathbf{0}$. So, under the assumption of directional independence of the incoming radiation, either reflectivity can be used for (2.52).

Whereas the above distributions are useful for obtaining and using experimental data, other distributions can be constructed using theoretical models. For engineering purposes, two particular distributions are often used because of their simplicity. The first is the distribution function corresponding to *diffuse reflection*. In the case of diffuse reflection a fraction $\rho_{\nu, d}$ of the incident radiation is reflected equally into every direction $\mathbf{s} \in \mathbb{H}^{+}$. The fraction $\rho_{\nu, d}$ is called the *diffuse reflectivity*. If we define the constant outgoing intensity as $\bar{I}'_{\nu}(\mathbf{x}_{\Gamma})$, we find for the radiosity due to reflection:

$$J'_{\nu}(\mathbf{x}_{\Gamma}) = \int_{\mathbb{H}^{+}} \bar{I}'_{\nu}(\mathbf{x}_{\Gamma}) \cos \vartheta \, d\omega = \bar{I}'_{\nu}(\mathbf{x}_{\Gamma}) \int_{\mathbb{H}^{+}} \cos \vartheta \, d\omega = \pi \bar{I}'_{\nu}(\mathbf{x}_{\Gamma}). \quad (2.54)$$

Construction of an energy balance at the boundary shows that, since $J'_{\nu} = \rho_{\nu, d} G'_{\nu}$, we have

$$\bar{I}'_{\nu}(\mathbf{x}_{\Gamma}) = \frac{1}{\pi} \rho_{\nu, d} G'_{\nu}(\mathbf{x}_{\Gamma}). \quad (2.55)$$

This corresponds to a hemispherical-directional reflectivity that is independent of the direction:

$$\rho_{\nu}(\mathbf{x}_{\Gamma}, \mathbb{H}^{-} \rightarrow \mathbf{s}) = \rho_{\nu, d}. \quad (2.56)$$

Substituting this result in (2.52), we find that the contribution of diffuse reflection to the outgoing intensity can be computed as

$$I_{\Gamma, \nu, \text{diffuse}}(\mathbf{x}_{\Gamma}, \mathbf{s}) = \frac{1}{\pi} \rho_{\nu, d} G'_{\nu}(\mathbf{x}_{\Gamma}). \quad (2.57)$$

The other simple reflection model is that of *specular reflection*. In this case a fraction ρ_s of the incident radiation is reflected as in a mirror. This means, that radiation arriving in direction $\tilde{\mathbf{s}}$ will be reflected in a direction \mathbf{s}^* , defined by

$$\mathbf{s}^* := \tilde{\mathbf{s}} + 2(\mathbf{n}_{\Gamma} \cdot \tilde{\mathbf{s}})\mathbf{n}_{\Gamma}. \quad (2.58)$$

The outgoing intensity in direction \mathbf{s}^* then is equal to the incoming intensity in direction $\tilde{\mathbf{s}}$: $I_\nu(\mathbf{x}_\Gamma, \mathbf{s}^*) = I_\nu(\mathbf{x}_\Gamma, \tilde{\mathbf{s}})$. That this is valid can be concluded from the fact that (2.58) maps \mathbb{H}^- exactly into \mathbb{H}^+ , which means that the reflected irradiance is equal to the induced radiosity:

$$\int_{\mathbb{H}^-} I_\nu(\mathbf{x}, \tilde{\mathbf{s}}) \cos \tilde{\vartheta} d\tilde{\omega} = \int_{\mathbb{H}^+} I_\nu(\mathbf{x}, \mathbf{s}) \cos \vartheta d\omega. \quad (2.59)$$

The fraction $\rho_{\nu,s}$ is called the *specular reflectivity*. The contribution of the specular reflections to the outgoing radiation becomes

$$I_{\Gamma,\nu,\text{specular}}(\mathbf{x}_\Gamma, \mathbf{s}) = \rho_{\nu,s} I_\nu(\mathbf{x}_\Gamma, \tilde{\mathbf{s}}), \quad (2.60)$$

with $\tilde{\mathbf{s}} = \mathbf{s} - 2(\mathbf{n}_\Gamma \cdot \mathbf{s})\mathbf{n}_\Gamma$ representing the sole direction that has a contribution in direction \mathbf{s} .

Since not all of the irradiance is reflected, the remainder is absorbed by the surface, if it is opaque. The quantity specifying this absorption is called the *spectral directional absorptivity* and is defined by

$$\alpha_\nu(\mathbf{x}_\Gamma, \tilde{\mathbf{s}}) := \frac{1}{I_\nu(\mathbf{x}_\Gamma, \tilde{\mathbf{s}}) \cos \tilde{\vartheta}} \frac{d\Phi'_{\nu,a}(\mathbf{x}, \tilde{\mathbf{s}})}{d\tilde{\omega}}, \quad (2.61)$$

where $\Phi'_{\nu,a}$ is the absorption rate of the surface and $d\Phi'_{\nu,a}/d\tilde{\omega}$ represents the absorption rate from a specific beam. Since we assumed the surface to be opaque, all incident radiation is either absorbed or reflected, so for every beam we find

$$\frac{d\Phi'_{\nu,a}}{d\tilde{\omega}}(\mathbf{x}_\Gamma, \tilde{\mathbf{s}}) = I_\nu(\mathbf{x}_\Gamma, \tilde{\mathbf{s}}) \cos \tilde{\vartheta} - \rho_\nu(\mathbf{x}_\Gamma, \tilde{\mathbf{s}} \rightarrow \mathbb{H}^+) I_\nu(\mathbf{x}_\Gamma, \tilde{\mathbf{s}}) \cos \tilde{\vartheta}, \quad (2.62)$$

which leads to the conclusion that

$$\alpha_\nu(\mathbf{x}_\Gamma, \tilde{\mathbf{s}}) = 1 - \rho_\nu(\mathbf{x}_\Gamma, \tilde{\mathbf{s}} \rightarrow \mathbb{H}^+). \quad (2.63)$$

For diffusely and specularly reflective boundaries, the absorptivity is independent of the incident direction. In these cases the absorptivity can be found by the simple relation

$$\alpha_\nu(\mathbf{x}_\Gamma) = 1 - \rho_{\nu,d} - \rho_{\nu,s}. \quad (2.64)$$

As we saw from the definition of a blackbody, it has the maximum possible emission rate. The *spectral directional emissivity* is defined as the imperfectness of the body under consideration:

$$\epsilon_\nu(\mathbf{x}_\Gamma, \mathbf{s}) := \frac{I_\nu(\mathbf{x}_\Gamma, \mathbf{s})}{B_\nu(\mathbf{x}_\Gamma)}. \quad (2.65)$$

If a body with such emissivity is placed in an isothermal enclosure, as we did with the blackbody, it can be derived that the rate at which the body emits radiative energy, has to be equal to its absorption rate:

$$\int_{\mathbb{H}^+} \epsilon_\nu(\mathbf{x}_\Gamma, \mathbf{s}) \cos \vartheta d\omega = \int_{\mathbb{H}^-} \alpha_\nu(\mathbf{x}_\Gamma, \tilde{\mathbf{s}}) \cos \tilde{\vartheta} d\tilde{\omega}. \quad (2.66)$$

If the absorptivity and emissivity are independent of the direction, this simply reduces to

$$\epsilon_\nu(\mathbf{x}_\Gamma) = \alpha_\nu(\mathbf{x}_\Gamma). \quad (2.67)$$

The contribution of natural radiation by the boundary to the outgoing radiation, can be computed by

$$I_{\Gamma,\nu,\text{emission}}(\mathbf{x}_\Gamma, \mathbf{s}) = \epsilon_\nu(\mathbf{x}_\Gamma) B_\nu(T_\Gamma(\mathbf{x}_\Gamma)), \quad (2.68)$$

where we used T_Γ for the temperature of the boundary itself, not of the glass close to the boundary. If problems without conduction are considered, these are typically not equal to each other. Together with (2.52), we then find for the outgoing intensity that

$$I_{\Gamma,\nu}(\mathbf{x}_\Gamma, \mathbf{s}) = \epsilon_\nu B_\nu(T_\Gamma(\mathbf{x}_\Gamma)) + \frac{1}{\pi} \rho_{\nu}(\mathbf{x}_\Gamma, \mathbb{H}^- \rightarrow \mathbf{s}) G'_\nu(\mathbf{x}_\Gamma). \quad (2.69)$$

If a combination of diffuse and specular reflectivities is used to model an opaque boundary, one finds

$$I_{\Gamma,\nu}(\mathbf{x}_\Gamma, \mathbf{s}) = (1 - \rho_{\nu,d} - \rho_{\nu,s}) B_\nu(T_\Gamma(\mathbf{x}_\Gamma)) + \frac{1}{\pi} \rho_{\nu,d} G'_\nu(\mathbf{x}_\Gamma) + \rho_{\nu,s} I_\nu(\mathbf{x}_\Gamma, \tilde{\mathbf{s}}). \quad (2.70)$$

With the two relations (2.69) and (2.70), the radiative problem is completely determined if all boundaries are opaque.

2.3.2 Transparent boundaries

However, if the surface boundary does not mark a transition from the glass to an opaque medium, but rather to another transparent or semi-transparent medium, a different set of contributions from reflections and emissions has to be constructed. Let us assume that the intensity in the other semi-transparent medium is known and that its value on the interface boundary is $I_{\Gamma,\nu,2}(\mathbf{x}_\Gamma, \mathbf{s})$ with $\mathbf{s} \in \mathbb{H}^+$. For example, when modelling a hot glass object standing in open air — or, for that matter, in the middle of a factory — the radiation falling onto the object can be modelled as an isothermal enclosure at temperature T_∞ radiating as a perfect blackbody and so $I_{\Gamma,\nu,2}(\mathbf{x}_\Gamma, \mathbf{s}) = B_\nu(T_\infty)$.

As shown in Figure 2.3, when a ray reaches the interface between two semi-transparent media, one part of it is refracted and another part is reflected. The Law of Reflection (see [Huygens, 1690]) states that the reflected direction follows the specular reflection defined before:

$$\mathbf{s} = \tilde{\mathbf{s}} - 2(\mathbf{n}_\Gamma \cdot \tilde{\mathbf{s}})\mathbf{n}_\Gamma, \quad (2.71)$$

where — as before — we used the primed direction for the radiation incident onto the boundary from the domain under consideration, and the unprimed direction for the outgoing radiation. The relation between the refracted direction and the incident direction is given by the Law of Sines or Snell's Law, which states that

$$\frac{\sin \vartheta_2}{\sin \vartheta_1} = \frac{n_1}{n_2}, \quad (2.72)$$

where ϑ_1 and ϑ_2 are the angles defined in the figure and n_1 and n_2 are the refractive indices of the two media. The amount of radiative energy that is reflected can be found using the Fresnel reflection equations, which lead to

$$\rho_{\nu,r}(\mathbf{x}_\Gamma, \vartheta_1) = \frac{1}{2} \left[\frac{\sin^2(\vartheta_1 - \vartheta_2)}{\sin^2(\vartheta_1 + \vartheta_2)} + \frac{\tan^2(\vartheta_1 - \vartheta_2)}{\tan^2(\vartheta_1 + \vartheta_2)} \right]. \quad (2.73)$$

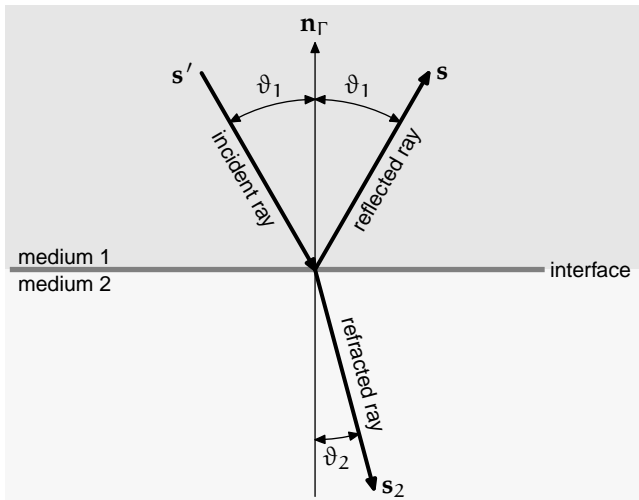


Figure 2.3: Refraction and reflection of radiation at an interface between two (semi) transparent media.

The notable symmetry in the appearance of sines and tangents is not so much mystical as it is due to the fact that this equation follows from a derivation using two orthogonal electro-magnetic waves, with amplitudes parallel and perpendicular to the surface respectively. A second note about this equation is that, although at first sight it seems that for a ray with a direction perpendicular to the surface, i.e. $\vartheta_1 = \vartheta_2 = 0$, $\rho_{v,f}(\mathbf{x}_\Gamma, 0) = 0$, elaboration learns that in fact

$$\rho_{v,f}(\mathbf{x}_\Gamma, 0) = \left(\frac{n_2 - n_1}{n_2 + n_1} \right)^2. \quad (2.74)$$

So, even for perpendicularly incident radiation, part of the radiation is reflected.

If we assume the second transparent medium to be air, as is common in glass processes, then $n_2 < n_1$. In this case a *critical angle* ϑ_1^* exists, such that the refracted direction lays parallel to the surface. Since in this case $\sin \vartheta_2 = 1$, the critical angle is defined by

$$\vartheta_1^* = \arcsin \frac{n_2}{n_1}. \quad (2.75)$$

For angles of incidence higher than this critical angle, (2.74) cannot be used. Instead, it is known that under these angles, all radiative energy is reflected:

$$\rho_{v,f}(\mathbf{x}_\Gamma, \vartheta_1) = 1, \quad \forall \vartheta_1 > \vartheta_1^*. \quad (2.76)$$

Since (2.73) and (2.76) are symmetric in ϑ_1 and ϑ_2 , the emissivity of the surface is

$$\epsilon_v(\mathbf{x}_\Gamma, \mathbf{s}) = 1 - \rho_{v,f}(\mathbf{x}_\Gamma, \vartheta_1). \quad (2.77)$$

The boundary condition for the RTE in case of Fresnel reflection at the boundary becomes

$$I_{\Gamma,v,\text{Fresnel}}(\mathbf{x}_\Gamma, \mathbf{s}) = (1 - \rho_{v,f}(\mathbf{x}_\Gamma, \vartheta_1)) I_{\Gamma,v,2}(\mathbf{x}_\Gamma, \mathbf{s}_2) + \rho_{v,f}(\mathbf{x}_\Gamma, \vartheta_1) I(\mathbf{x}_\Gamma, \tilde{\mathbf{s}}), \quad (2.78)$$

which should be used for transitions from one transparent medium to another. Note that except for the fact that the reflectivity is a function of the angle with the surface normal, the formulation is very similar to the specular reflections we saw before; this means that in later chapters, when analysing the implementation and complexity, Fresnel reflections behave as specular reflection as well. Later, notably in Chapter 6, we show examples of the use of Fresnel reflections.

2.4 Summary

In this chapter we introduced the governing equations for radiative heat transfer, both within the domain and at the boundary. Throughout the chapter we have encountered many equations. For clarity, here we list the ones that are the most important for radiative heat computations. We have shown that the divergence of the heat flux can be computed through

$$\nabla \cdot \mathbf{q}_\nu = 4\pi\kappa_\nu B_\nu - \kappa_\nu G_\nu. \quad (2.39)$$

While the blackbody intensity B_ν is directly related to the temperature, the total incident radiation G_ν has to be obtained from the intensity by

$$G_\nu(\mathbf{x}) := \int_{\mathbb{S}_2} I_\nu(\mathbf{x}, \mathbf{s}) d\omega. \quad (2.18)$$

This means that the intensity needs to be known throughout the domain and in every direction. The intensity itself can be obtained by solving the RTE

$$\mathbf{s} \cdot \nabla I_\nu(\mathbf{x}, \mathbf{s}) + \kappa_\nu(\mathbf{x}) I_\nu(\mathbf{x}, \mathbf{s}) = \kappa_\nu(\mathbf{x}) B_\nu(\mathbf{x}). \quad (2.32)$$

Clearly, to solve this equation we again need to know the blackbody intensity, and consequently the temperature. Additionally, we need to know the intensity of radiation leaving the boundary. This can be found by solving radiative boundary equations. Their are different models for reflections at the boundary. About the reflective interaction between glass and opaque boundaries not much data is available. Therefore, opaque boundaries are often modelled using specular and diffuse reflections. For those boundaries the intensity leaving the boundaries can be found using

$$I_{\Gamma,\nu}(\mathbf{x}_\Gamma, \mathbf{s}) = (1 - \rho_{\nu,d} - \rho_{\nu,s}) B_\nu(T_\Gamma(\mathbf{x}_\Gamma)) + \frac{1}{\pi} \rho_{\nu,d} G'_\nu(\mathbf{x}_\Gamma) + \rho_{\nu,s} I_\nu(\mathbf{x}_\Gamma, \tilde{\mathbf{s}}). \quad (2.70)$$

If a boundary is an interface between two (semi-)transparent media Fresnel reflections are used instead. The intensity leaving the boundary into the domain of interest then is given by the boundary becomes

$$I_{\Gamma,\nu,\text{Fresnel}}(\mathbf{x}_\Gamma, \mathbf{s}) = (1 - \rho_{\nu,f}(\mathbf{x}_\Gamma, \vartheta_1)) I_{\Gamma,\nu,2}(\mathbf{x}_\Gamma, \mathbf{s}_2) + \rho_{\nu,f}(\mathbf{x}_\Gamma, \vartheta_1) I(\mathbf{x}_\Gamma, \tilde{\mathbf{s}}). \quad (2.78)$$

The equations that we have repeated here define the radiative problem. In the next section we investigate various methods to solve the thus defined problem. Furthermore, we get familiar with the behaviour of radiation.

Solution methods

In the previous chapter we have seen that in order to compute radiative heat transfer, i.e. the divergence of the radiative heat flux, we have to know the intensity. By the very nature of this quantity — after all, it depends on six independent variables: three spatial, two directional and one spectral — it is challenging for every method for radiative heat transfer, to achieve an accurate description of the radiative field, while maintaining limited needs for both computational time and memory.

The fact that, in theory, not the intensity itself needs to be known but rather its directional average, as was shown in (2.39), only provides an additional sour paradox: we are likely to add complexity to our problem for a quantity we ultimately do not need. Of course, for an accurate description of the directionally average intensity we do need to know the intensity, yet it indicates that complexity might be reduced if explicit computation of the intensity can be avoided.

To study methods to compute radiative heat transfer, we start with a one-dimensional problem. In one dimension the RTE (2.32) can be solved straightforwardly for any direction. The analytical solution provides a very good basis for comparison of the accuracy of other methods. Furthermore, the methodology of this problem lays at the basis of the Algebraic Ray Trace method presented in the next chapter.

In Section 3.2, a widely used approximation is studied: the Rosseland Approximation. By making assumptions on the physical properties of the radiative problem, this approximation avoids computation of the intensity and arrives at a formulation of the heat flux that resembles the conductive term in (2.7); this makes it easy to implement. Since assumptions about the physics inherently limit the reach of the problems a method can address, we pay special attention to determine in which case it is appropriate to use this method and when it should be avoided. It is shown that for many applications in glass production, this method is of insufficient accuracy.

That same section explains an improved version of the Rosseland approximation. This is done by adding an extra term, containing information about the radiation at the boundary. For optically thick problems, such an approach offers good results.

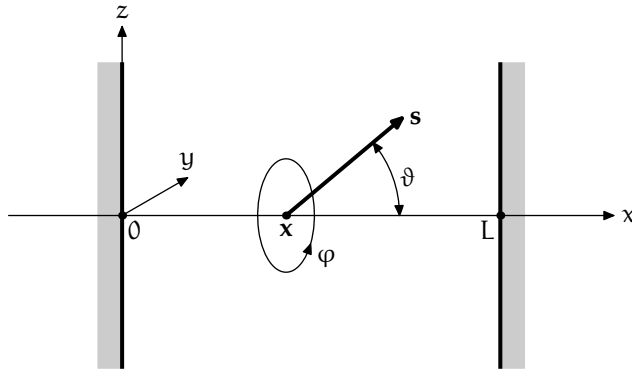


Figure 3.1: Definition of angles for a one-dimensional radiative problem in a slab geometry.

The so-called Discrete Ordinate Method is introduced in Section 3.3. This method is an aid for numerical approaches to the solution of the RTE. It offers a set of directions together with an appropriate quadrature over the direction space. The RTE then can be solved for the limited number of directions in the set.

In Section 3.4 we have look at some other existing numerical methods: the ray trace method, the Monte Carlo method and a finite element formulation. These are discussed briefly to show where their shortcoming are and what are the elements we want to improve upon.

3.1 Exact solution in one dimension

If the geometry is one-dimensional — e.g. a sheet of glass between two infinite plates as displayed in Figure 3.1 — we can find an exact solution for the radiative heat flux and its divergence. Here, we only restrict the spatial coordinate to one dimension, the directional vector still lies in \mathbb{S}_2 . So, while all entities just depend on one dimension, radiation is allowed to move in a three-dimensional space. If a spherical coordinate system is chosen, such as in Figure 3.1, ϑ represents the angle with the x -axis and φ the angle around the x -axis, it is clear that because of the one-dimensionality all entities are independent of φ . Rather than using ϑ as a description, we use its cosine:

$$\mu := \cos \vartheta. \quad (3.1)$$

If we assume that the absorption coefficient is constant over the domain, we can formulate the RTE (2.32) for the slab geometry in the optical coordinate $\tau = \kappa_\nu x$ as

$$\mu \frac{\partial I_\nu}{\partial \tau}(\tau, \mu) + I_\nu(\tau, \mu) = B_\nu(\tau). \quad (3.2)$$

The problem in Figure 3.1 has a geometrical depth L , which corresponds to an optical thickness of $\tau_0 = \kappa_\nu L$. For the formal solution to this equation, we discern intensity in forward x -direction, denoted by $I_\nu^+(\tau, \mu)$, and intensity in negative x -

direction for which the notation $I_{\nu}^{-}(\tau, \mu)$ is used. For any $\mu > 0$, we find

$$I_{\nu}^{+}(\tau, \mu) = I_{\nu}^{+}(0, \mu)e^{-\tau/\mu} + \frac{1}{\mu} \int_0^{\tau} e^{-(\tau-s)/\mu} B_{\nu}(s) ds, \quad (3.3a)$$

$$I_{\nu}^{-}(\tau, -\mu) = I_{\nu}^{-}(\tau_0, \mu)e^{-(\tau_0-\tau)/\mu} + \frac{1}{\mu} \int_{\tau}^{\tau_0} e^{-(s-\tau)/\mu} B_{\nu}(s) ds. \quad (3.3b)$$

For the limiting case that $\mu = 0$, which corresponds to directions perpendicular to the x -axis, (3.2) directly states that

$$I_{\nu}(\tau, 0) = B_{\nu}(\tau). \quad (3.4)$$

For further analysis, equations (3.3a) and (3.3b) are replaced by a more formal notation. In one dimension, the intersection point \mathbf{x}_{Γ} with the boundary defined in (2.41) can be found straightforwardly. Expressed in terms of optical distance it can be written as

$$\tau_{\Gamma}(\tau, \mu) = \begin{cases} 0, & \text{if } \mu > 0, \\ \tau_0, & \text{if } \mu < 0. \end{cases} \quad (3.5)$$

This allows us to replace the integrals in the formal solution by the operator A_{μ} defined by:

$$(A_{\mu}f)(\tau) := \frac{1}{\mu} \int_{\tau_{\Gamma}}^{\tau} e^{-|\tau-s|/|\mu|} f(s) ds. \quad (3.6)$$

The observation made in (3.4) reduces this operator to the unity operator for radiation perpendicular to the x -axis, i.e. at $\mu = 0$:

$$(A_0f)(\tau) := f(\tau). \quad (3.7)$$

The contribution of the boundary to the intensity at any point is the intensity at the boundary scaled by some extinction coefficient, defined by

$$R_b(\tau, \mu) := e^{-|\tau-\tau_{\Gamma}|/|\mu|}. \quad (3.8)$$

Using these notations, we can rewrite equations (3.3a) and (3.3b) as

$$I_{\nu}(\tau, \mu) = (A_{\mu}B_{\nu})(\tau) + R_b(\tau, \mu)I_{\Gamma,\nu}(\tau, \mu), \quad (3.9)$$

where we have used the following shorthand form for the radiation at the boundaries:

$$I_{\Gamma,\nu}(\tau, \mu) = I_{\nu}(\tau_{\Gamma}(\tau, \mu), \mu) = \begin{cases} I_{\nu}(0, \mu), & \mu > 0 \\ I_{\nu}(\tau_0, \mu), & \mu < 0 \end{cases} \quad (3.10)$$

Since A_{μ} and R_b depend on the geometry only, and not on the radiative field, we see that the intensity in the domain is only coupled to the intensity on the boundary. So, if the latter is known the intensity can be computed independent of the other intensities. Furthermore, this relation shows that the intensities on the different boundaries are coupled.

3.1.1 Radiative heat flux

This formal solution can be further processed to compute the radiative heat transfer. The divergence of the heat flux stated in (2.39), can be expressed in optical coordinates and using the operator notation of (2.10) for the integration as

$$\frac{dq_\nu}{d\tau}(\tau) = 4\pi B_\nu(\tau) - (W I_\nu)(\tau). \quad (3.11)$$

The integration over all directions is a bit simpler in the one-dimensional case due to the independence on φ . So, we find that the operator W can be worked out as

$$(Wf)(x) = 2\pi \int_{-1}^1 f(x, \mu) d\mu. \quad (3.12)$$

After substitution of (3.9), this results in

$$\frac{dq_\nu}{d\tau} = (4\pi - WA_\mu)B_\nu - W(R_b I_{\Gamma_\nu}). \quad (3.13)$$

Since in this formulation application of A_μ is always followed by integration over all directions through W , it makes sense to combine them into the direction-independent operator G :

$$(Gf)(\tau) := (W(A_\mu f))(\tau). \quad (3.14)$$

In order to find an explicit formulation for this new operator, it is simpler to first consider integration over the two different hemispheres, as the interval over which is integrated in (3.6) is different in those cases. The integration over all directions performed by the operator W can be replaced by integration over the two hemispheres, defined in (2.11) and (2.12), with the positive x -direction taken as the normal direction:

$$W(A_\mu f) = W^+(A_\mu f) + W^-(A_\mu f). \quad (3.15)$$

The integration over the separate hemispheres is more convenient:

$$\int_{\mathbb{H}^+} A_\mu f(s) d\omega = 2\pi \int_0^1 \int_0^\tau \frac{1}{\mu} e^{-(\tau-s)/\mu} f(s) ds d\mu = 2\pi \int_0^\tau E_1(\tau-s) f(s) ds, \quad (3.16a)$$

$$\int_{\mathbb{H}^-} A_\mu f(s) d\omega = 2\pi \int_{-1}^0 \int_\tau^{\tau_0} \frac{1}{\mu} e^{-(s-\tau_0)/\mu} f(s) ds d\mu = 2\pi \int_\tau^{\tau_0} E_1(s-\tau) f(s) ds. \quad (3.16b)$$

Combining these equations, we find the operator G to be

$$(Gf)(\tau) = 2\pi \int_0^{\tau_0} E_1(|s-\tau|) f(s) ds, \quad (3.17)$$

with $E_1(x)$ being the *exponential integral* of the first order, which is discussed in more detail in Appendix A. Instead of optical coordinates, we can use Cartesian coordinates. Rewriting (3.17) we then find

$$(G_\nu^* f)(x) = 2\pi \int_0^L \kappa_\nu E_1(\kappa_\nu |s-x|) f(s) ds, \quad (3.18)$$

where we have used the asterisk to indicate that this formulation is used for a different coordinate system. The index ν was added to signal the right-hand side's explicit dependence on the frequency. Using this formulation, the divergence of the heat flux is written as

$$\frac{dq_\nu}{d\tau} = (4\pi - G)B_\nu - W(R_b I_{\Gamma,\nu}) \quad \text{or} \quad \frac{1}{\kappa_\nu} \frac{dq_\nu}{dx} = (4\pi - G_\nu^*)B_\nu - W(R_b I_{\Gamma,\nu}). \quad (3.19)$$

This formulation shows, that in order to compute the radiative heat transfer in the domain it is not necessary to know the intensity in the whole domain. The operator G only depends on the *optical geometry*, i.e. the physical geometry and the distribution of the absorption coefficient. Since $I_{\Gamma,\nu}$ itself depends on the direction, we cannot *a priori* perform the integration of R_b over all directions. This also means, that in order to compute the heat flux, the intensity needs to be known everywhere on the boundary and in every direction that points into the domain.

3.1.2 Boundary conditions

For black boundaries, prescribed in a manner analogous to (2.42) as

$$I_{\Gamma,\nu}(\tau, \mu) = B_{\Gamma,\nu}(\tau_\Gamma(\tau, \mu)), \quad (3.20)$$

the boundary radiation can straightforwardly be determined from the temperature of the boundary. Again, making a split between the positive x -direction and negative x -direction we find

$$W(R_b I_{\Gamma,\nu}) = W^+(R_b I_\nu^+(0, \mu)) + W^-(R_b I_\nu^-(\tau_0, \mu)). \quad (3.21)$$

Like before, the operators can be evaluated more easily if we treat the two hemispheres separately

$$W^+(R_b I_{\Gamma,\nu}) = 2\pi \int_0^1 e^{-\tau/\mu} B_{\nu,0} d\mu = 2\pi E_2(\tau) B_{\nu,0}, \quad (3.22a)$$

$$W^-(R_b I_{\Gamma,\nu}) = 2\pi \int_{-1}^0 e^{(\tau_0 - \tau)/\mu} B_{\nu,1} d\mu = 2\pi E_2(\tau_0 - \tau) B_{\nu,1}. \quad (3.22b)$$

Here, we used $B_{\nu,0}$ and $B_{\nu,1}$ for the blackbody intensity of the two boundaries; E_2 is an exponential integral and is discussed in Appendix A. So the computation of the heat flux divergence is accomplished by the combination of (3.19), (3.22a) and (3.22b):

$$\frac{dq_\nu}{dx} = 4\pi\kappa_\nu B_\nu(x) - 2\pi\kappa_\nu^2 \int_0^L E_1(\kappa_\nu|x-s|) B_\nu(s) ds - 2\pi\kappa_\nu E_2(\kappa x) - 2\pi\kappa_\nu E_2(\kappa(L-x)). \quad (3.23)$$

From this equation it follows that knowledge of the geometry and temperature suffices for computation of radiative heat transfer: We do not need to compute the intensity explicitly. This lowers the computational complexity, as the introduction of the intensity, which depends on six independent variables, can be omitted. An example of the computation of the heat flux divergence can be found below in Section 3.1.3.

This situation changes if reflections are present. In Section 2.3, reflections were discussed in some detail. For the exact solution we limit ourselves to the two cases where either diffuse or specular reflection is present. In one dimension the specular reflective boundary conditions for $\mu > 0$ are

$$I_{\nu}^{+}(0, \mu) = \epsilon_{\nu,0} B_{\nu,0} + \rho_{\nu,0} I_{\nu}^{-}(0, -\mu), \quad (3.24a)$$

$$I_{\nu}^{-}(\tau_0, -\mu) = \epsilon_{\nu,1} B_{\nu,1} + \rho_{\nu,1} I_{\nu}^{+}(\tau_0, \mu). \quad (3.24b)$$

In these equations, the intensities on the right-hand side are unknown. However, we can use the formal solutions of (3.3a) and (3.3b), to reduce the number of unknowns. After substitution we find

$$I_{\nu}^{+}(0, \mu) = \epsilon_{\nu,0} B_{\nu,0} + \rho_{\nu,0} I_{\nu}^{-}(\tau_0, -\mu) e^{-\tau_0/\mu} + \rho_{\nu,0} (A_{-\mu} B_{\nu})(0), \quad (3.25a)$$

$$I_{\nu}^{-}(\tau_0, -\mu) = \epsilon_{\nu,1} B_{\nu,1} + \rho_{\nu,1} I_{\nu}^{+}(0, \mu) e^{-\tau_0/\mu} + \rho_{\nu,1} (A_{\mu} B_{\nu})(\tau_0). \quad (3.25b)$$

So, for every positive μ , we find a linear system of equations:

$$\begin{pmatrix} 1 & -\rho_{\nu,0} e^{-\tau_0/\mu} \\ -\rho_{\nu,1} e^{-\tau_0/\mu} & 1 \end{pmatrix} \begin{pmatrix} I_{\nu}^{+}(0, \mu) \\ I_{\nu}^{-}(\tau_0, -\mu) \end{pmatrix} = \begin{pmatrix} b_{\nu,0}(\mu) \\ b_{\nu,1}(-\mu) \end{pmatrix}, \quad (3.26)$$

where we have used the following definitions:

$$b_{\nu,0}(\mu) := \epsilon_{\nu,0} B_{\nu,0} + \rho_{\nu,0} (A_{-\mu} B_{\nu})(0), \quad (3.27a)$$

$$b_{\nu,1}(-\mu) := \epsilon_{\nu,1} B_{\nu,1} + \rho_{\nu,1} (A_{\mu} B_{\nu})(\tau_0). \quad (3.27b)$$

The determinant of this system is $D_{\nu,\mu} := 1 - \rho_{\nu,0} \rho_{\nu,1} e^{-2\tau_0/\mu}$, from which it follows that the system has a solution unless both $\rho_{\nu,0} = \rho_{\nu,1} = 1$ and $\tau_0 = 0$. If we omit the possibility of a degenerate geometry, the second condition implies that $\kappa_{\nu} = 0$, i.e. there is no interaction with the medium. This again means that the right-hand side, too, will be zero. More interestingly, this states that in a semi-transparent medium a solution can always be found, even if all the boundaries are purely reflective. The solution is

$$I^{+}(0, \mu) = \frac{1}{D_{\nu,\mu}} b_{\nu,0}(\mu) + \frac{\rho_{\nu,0}}{D_{\nu,\mu}} e^{-\tau_0/\mu} b_{\nu,1}(-\mu), \quad (3.28a)$$

$$I^{-}(\tau_0, \mu) = \frac{1}{D_{\nu,\mu}} b_{\nu,1}(-\mu) + \frac{\rho_{\nu,1}}{D_{\nu,\mu}} e^{-\tau_0/\mu} b_{\nu,0}(\mu). \quad (3.28b)$$

With these equations the outgoing radiation at the boundary can be calculated once the temperature distribution and consequently the blackbody intensity distribution are known. To compute the contribution to the heat flux divergence, these results still need to be integrated over all directions weighed according to (3.21). Unfortunately, the $1/D_{\nu,\mu}$ term prevents finding a closed solution. For very small reflection coefficients, however, we have $D_{\nu,\mu} \approx 1$. Under this as-

Name	κ [m^{-1}]	n [—]	c_v [J/kgK]	ρ [kg/m^3]
Green bottle	350	1.47	1350	2500
White float	35	1.47	1350	2500

Table 3.1: Material properties of some grey glasses used in sample computations.

sumption, i.e. $\rho_{v,0}, \rho_{v,1} \ll 1$, we find

$$\begin{aligned} I^+(0, \mu) &\approx b_{v,0}(\mu) + \rho_{v,0} e^{-\tau_0/\mu} b_{v,1}(-\mu) \\ &\approx \epsilon_{v,0} B_{v,0} + \rho_{v,0} B_{v,1} e^{-\tau_0/\mu} + \rho_{v,0} \int_0^{\tau_0} e^{-s/\mu} B(s) ds, \end{aligned} \quad (3.29a)$$

$$\begin{aligned} I^-(\tau_0, -\mu) &\approx b_{v,1}(-\mu) + \rho_{v,1} e^{-\tau_0/\mu} b_{v,0}(\mu) \\ &\approx \epsilon_{v,1} B_{v,1} + \rho_{v,1} B_{v,0} e^{-\tau_0/\mu} + \rho_{v,1} \int_0^{\tau_0} e^{-(\tau_0-s)/\mu} B(s) ds, \end{aligned} \quad (3.29b)$$

where we left out all terms containing the product $\rho_{v,0}\rho_{v,1}$ and used the fact that $\epsilon_{v,i}\rho_{v,j} = (1 - \rho_{v,i})\rho_{v,j} \approx \rho_{v,j}$. These simplifications allow us to integrate over all directions, as specified by (3.21):

$$\begin{aligned} \frac{1}{2\pi} W^+(R_b I_{\Gamma,v}) &= \epsilon_{v,0} B_{v,0} E_2(\tau) + \\ &\quad \rho_{v,0} B_{v,1} E_2(\tau_0 + \tau) + \rho_{v,0} \int_0^{\tau_0} E_1(\tau + s) B(s) ds, \end{aligned} \quad (3.30a)$$

$$\begin{aligned} \frac{1}{2\pi} W^-(R_b I_{\Gamma,v}) &= \epsilon_{v,1} B_{v,1} E_2(\tau_0 - \tau) + \\ &\quad \rho_{v,1} B_{v,0} E_2(2\tau_0 - \tau) + \rho_{v,1} \int_0^{\tau_0} E_1(2\tau_0 - \tau - s) B(s) ds. \end{aligned} \quad (3.30b)$$

The three parts on the right-hand side correspond to the emission of the wall itself, the reflected radiation emitted by the other wall and the reflected radiation generated by the medium. A more precise approximation can be made for higher values of the reflectivity coefficients, by expanding the geometric series generated by the approximation of $1/D_{v,\mu}$:

$$\frac{1}{D_{v,\mu}} = 1 + d_{v,\mu} + d_{v,\mu}^2 + \cdots + d_{v,\mu}^n + O(d_{v,\mu}^{n+1}), \quad (3.31)$$

with $d_{v,\mu} := \rho_{v,0}\rho_{v,1} e^{-2\tau_0/\mu}$. Every term in this series corresponds to an extra reflection step taken into account. The accuracy eventually depends on the value of d , which as we have seen is certainly less than 1 for semi-transparent media.

Once the boundary contribution problem has been solved, enough information is available to compute (3.19). Here, we forgo writing the complete expression for the divergence of radiative heat flux. In Section 3.1.3 an example is presented for a one-dimensional problem, of which the results are shown in Figure 3.2.

While in the previous analysis we encountered a system for every $(\mu, -\mu)$ -pair, diffuse reflections give rise to a coupling between more directions. As seen in

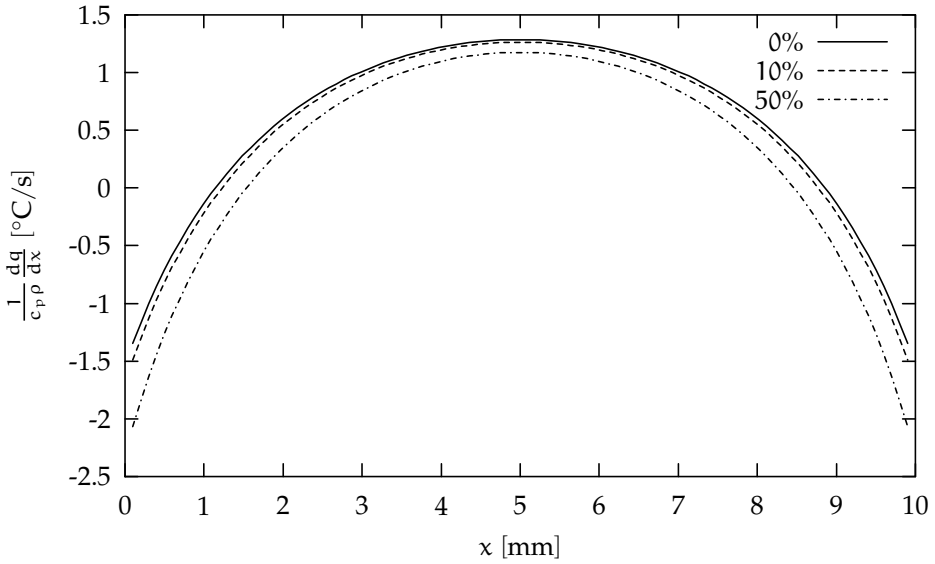


Figure 3.2: Divergence of the heat flux for various values of the specular reflectivity for a parabolic temperature profile in a 1 cm slab geometry with the green glass from Table 3.1 as medium.

Section 2.3, diffuse reflections provide the following boundary conditions:

$$I_{\nu}^{+}(0, \mu) = \epsilon_{\nu,0} B_{\nu,0} + \rho_{\nu,0} \frac{1}{\pi} G'_{\nu}(0) \quad (3.32a)$$

$$I_{\nu}^{-}(\tau_0, -\mu) = \epsilon_{\nu,1} B_{\nu,1} + \rho_{\nu,1} \frac{1}{\pi} G'_{\nu}(\tau_0). \quad (3.32b)$$

In these equations G' is the irradiance defined in (2.44), which itself is depending on the incoming radiation, but independent of the direction. In one dimension it can be computed as

$$G'_{\nu}(0) = 2\pi \int_0^1 I_{\nu}^{-}(0, -\mu) \mu \, d\mu \quad (3.33a)$$

$$G'_{\nu}(\tau_0) = 2\pi \int_0^1 I_{\nu}^{+}(\tau_0, \mu) \mu \, d\mu. \quad (3.33b)$$

After substituting the formal solution in (3.3a) and (3.3b), we find this is equal to

$$G'_{\nu}(0) = 2\pi \int_0^1 \left[I_{\nu}^{-}(\tau_0, -\mu) e^{-\tau_0/\mu} + (A_{\mu} B_{\nu})(0) \right] \mu \, d\mu, \quad (3.34a)$$

$$G'_{\nu}(\tau_0) = 2\pi \int_0^1 \left[I_{\nu}^{+}(0, \mu) e^{-\tau_0/\mu} + (A_{-\mu} B_{\nu})(\tau_0) \right] \mu \, d\mu. \quad (3.34b)$$

Introducing $g_{\nu,0} := \int_0^1 I_{\nu}^{+}(0, \mu) e^{-\tau_0/\mu} \mu \, d\mu$ and $g_{\nu,1} := \int_0^1 I_{\nu}^{-}(\tau_0, -\mu) e^{-\tau_0/\mu} \mu \, d\mu$,

this can be written as

$$G'(0) = 2\pi g_{\nu,1} + 2\pi \int_0^{\tau_0} E_2(s) B_{\nu}(s) ds, \quad (3.35a)$$

$$G'(\tau_0) = 2\pi g_{\nu,0} + 2\pi \int_0^{\tau_0} E_2(\tau_0 - s) B_{\nu}(s) ds. \quad (3.35b)$$

We can reduce the number of unknowns by multiplying (3.32a) and (3.32b) by $\mu e^{-\tau_0/\mu}$ and integrating those over the interval $\mu = (0, 1)$. We find

$$g_{\nu,0} = \epsilon_{\nu,0} B_{\nu,0} E_3(\tau_0) + 2\rho_{\nu,0} g_{\nu,1} E_3(\tau_0) + 2\rho_{\nu,0} E_3(\tau_0) \int_0^{\tau_0} E_2(s) B_{\nu}(s) ds, \quad (3.36a)$$

$$g_{\nu,1} = \epsilon_{\nu,1} B_{\nu,1} E_3(\tau_0) + 2\rho_{\nu,1} g_{\nu,0} E_3(\tau_0) + 2\rho_{\nu,1} E_3(\tau_0) \int_0^{\tau_0} E_2(\tau_0 - s) B_{\nu}(s) ds, \quad (3.36b)$$

where we have introduced another exponential integral E_3 , which is explained in Appendix A. This corresponds to the system

$$\begin{pmatrix} 1 & -2\rho_{\nu,0} E_3(\tau_0) \\ -2\rho_{\nu,1} E_3(\tau_0) & 1 \end{pmatrix} \begin{pmatrix} g_{\nu,0} \\ g_{\nu,1} \end{pmatrix} = \begin{pmatrix} b_{\nu,0} \\ b_{\nu,1} \end{pmatrix}, \quad (3.37)$$

where we again have used a shorthand form for the right-hand side:

$$b_{\nu,0} := \epsilon_{\nu,0} B_{\nu,0} E_3(\tau_0) + 2\rho_{\nu,0} E_3(\tau_0) \int_0^{\tau_0} E_2(s) B_{\nu}(s) ds, \quad (3.38a)$$

$$b_{\nu,1} := \epsilon_{\nu,1} B_{\nu,1} E_3(\tau_0) + 2\rho_{\nu,1} E_3(\tau_0) \int_0^{\tau_0} E_2(\tau_0 - s) B_{\nu}(s) ds. \quad (3.38b)$$

The solution of this system can be found if its determinant, defined by

$$D_{\nu} := 1 - 4\rho_{\nu,0}\rho_{\nu,1} E_3^2(\tau_0), \quad (3.39)$$

is unequal to zero. As was the case with specular reflections this is true as long as $\tau_0 > 0$ and the walls are purely reflective at the same time. The solution to the system is

$$g_{\nu,0} := \frac{1}{D_{\nu}} b_{\nu,0} + \frac{2}{D_{\nu}} \rho_{\nu,0} E_3(\tau_0) b_{\nu,1}, \quad (3.40a)$$

$$g_{\nu,1} := \frac{1}{D_{\nu}} b_{\nu,1} + \frac{2}{D_{\nu}} \rho_{\nu,1} E_3(\tau_0) b_{\nu,0}. \quad (3.40b)$$

These values can be calculated once the distribution in blackbody intensity is known. Then, using (3.35a) and (3.35b), we can calculate the intensities according to (3.32a) and (3.32b). Since these intensities do not depend on the direction, the contributions in (3.21) can be easily computed. After these manipulations we arrive at

$$W^+(R_b I_{\Gamma,\nu}) = 2\pi I_{\nu}^+(0, \mu) \int_0^1 e^{-\tau/\mu} d\mu = 2\pi I_{\nu}^+(0, \mu) E_2(\tau), \text{ for any } \mu > 0, \quad (3.41a)$$

$$W^-(R_b I_{\Gamma,\nu}) = 2\pi I_{\nu}^-(\tau_0, -\mu) \int_0^1 e^{-\tau/\mu} d\mu = 2\pi I_{\nu}^-(\tau_0, -\mu) E_2(\tau_0 - \tau), \text{ for any } \mu > 0. \quad (3.41b)$$

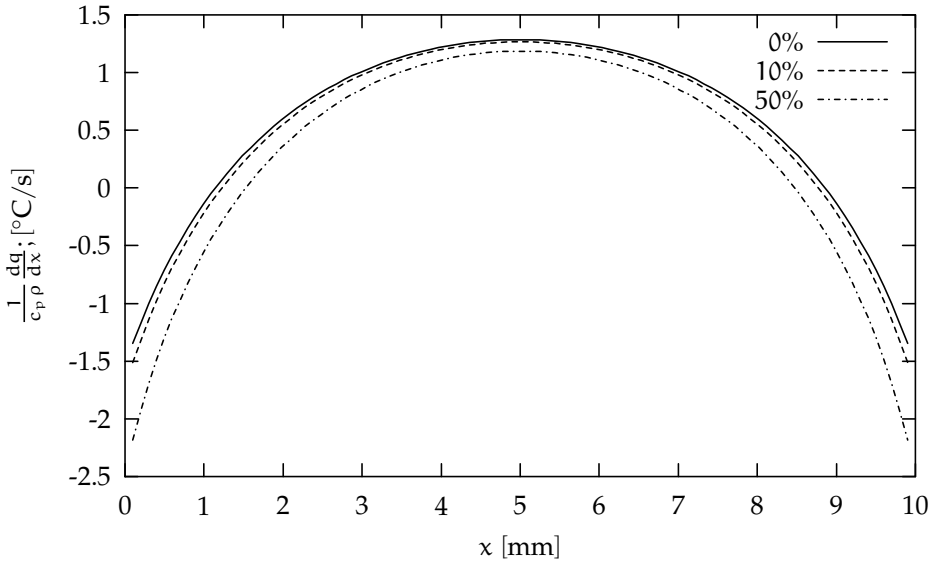


Figure 3.3: Divergence of the heat flux for various values of the diffuse reflectivity for a parabolic temperature profile in a 1 cm slab geometry with the green glass from Table 3.1 as medium.

To compare these results with the ones obtained for specular reflection, we again make the assumption that the reflectivities are so small that the determinant $D_\nu \approx 1$. This approximation leads to

$$g_{\nu,0} \approx b_{\nu,0} + \rho_{\nu,0} E_3(\tau_0) b_{\nu,1} \approx \epsilon_{\nu,0} B_{\nu,0} E_3(\tau_0), \quad (3.42a)$$

$$g_{\nu,1} \approx b_{\nu,1} + \rho_{\nu,1} E_3(\tau_0) b_{\nu,1} \approx \epsilon_{\nu,1} B_{\nu,1} E_3(\tau_0). \quad (3.42b)$$

The terms with reflectivity disappear, as only higher powers of the reflectivity appear. Together with the assumption that the reflectivities are small this makes them negligible. The approximate contribution to the heat flux by the reflective boundaries becomes

$$\begin{aligned} \frac{1}{2\pi} W^+(R_b I_{\Gamma,\nu}) &= \epsilon_{\nu,0} B_{\nu,0} E_2(\tau) + \\ & 2\rho_{\nu,0} B_{\nu,1} E_3(\tau_0) E_2(\tau) + 2\rho_{\nu,0} E_2(\tau) \int_0^{\tau_0} E_2(s) B_\nu(s) ds, \end{aligned} \quad (3.43a)$$

$$\begin{aligned} \frac{1}{2\pi} W^-(R_b I_{\Gamma,\nu}) &= \epsilon_{\nu,1} B_{\nu,1} E_2(\tau_0 - \tau) + \\ & 2\rho_{\nu,1} B_{\nu,0} E_3(\tau_0) E_2(\tau_0 - \tau) + 2\rho_{\nu,1} E_2(\tau_0 - \tau) \int_0^{\tau_0} E_2(\tau_0 - s) B_\nu(s) ds. \end{aligned} \quad (3.43b)$$

Together with (3.19), we can use these equations to compute the divergence of the radiative heat flux with diffuse boundaries. In the next subsection we have a look at how this compares to specular reflection, in several example computations.

3.1.3 Results

To compare the three different types of boundaries discussed before, a 1D example is considered. The geometry is chosen as a 1 cm thick slab with the green glass specified in Table 3.1 as a semi-transparent medium. On this medium a parabolic temperature profile is imposed such that the temperature at the boundaries is 1000°C, while the temperature in the middle is 20°C higher.

The results for specular reflection are displayed in Figure 3.2. This figure shows the weighed divergence of the heat flux at various levels of the specular reflectivity. The case with $\rho = 0$, of course, corresponds to a geometry with black boundaries. By dividing the heat flux divergence by the specific heat c_v and the density ρ , it represents the cooling rate if radiative heat transfer were the only mode of heat transfer. As we can see, an increase in the reflectivity means an overall reduction of the cooling rate, whilst the heating near the boundaries increases.

In Figure 3.3 the weighed divergence of the heat flux is shown for the case of diffuse reflections. Comparing the results with the specular reflections, we observe the differences are minimal. However, we have seen that the diffuse reflection is considerably easier to calculate; after all the integrals in (3.30a) and (3.30b) need to be evaluated for every τ , while in the diffuse formulation the integrals in (3.43a) and (3.43b) only need to be evaluated once for all τ .

This indicates the simpler model of diffuse reflections could be used instead of specular reflections. Whether this also holds for geometries in higher dimensions is investigated in later chapters, yet for one-dimensional geometries with low values of the reflectivity using the diffuse model instead of the specular model represents a significant reduction in complexity in the computation of the boundary intensity. The origin of this difference between the two formulations, can be found in the fact that the outgoing intensities are independent of the direction. In the diffuse formulation, in fact, we have managed to compute the divergence of the radiative heat flux completely without computing the intensity, by using the total incident radiation within the domain and the irradiance at the boundaries. Later in Section 5.1, we will show that in more dimensions diffuse boundaries are more difficult to treat and will lead to higher memory requirements of the numerical model. But if the boundaries are completely diffuse, the observation that diffuse boundaries do not need explicit computation of the intensity in order to obtain the divergence of the heat flux, remains valid. In Section 5.3 we manage to formulate the higher dimensional problem in such a way.

3.2 Diffusion approximations

As we saw in the previous section, even for simple one-dimensional geometries, finding the heat flux can become quite arduous. In higher dimensions, where the geometries can be far more complex, it is even hard to formulate the necessary equations, let alone to solve them. For that reason many people have sought a physically approximative model to treat radiation. For simulations involving hot glass, the most popular of those methods is undoubtedly the so-called *Rosseland approximation*, which is treated below in the first subsection.

Unfortunately, the Rosseland method is often used where it is not appropriate, i.e. outside the domain of optically thick problems and close to the boundaries. Various improvements on the Rosseland approximation have been sought by people, yielding a class of methods called *modified diffusion approximations*. One of those improvements is discussed below, in the second subsection. The improvement makes additional effort, but the results are much better close to the boundaries.

3.2.1 Rosseland Approximation

Rosseland formulated the approximation in [Rosseland, 1936] to study radiative transfer in the interiors of stars. Because stars have large geometries, some assumptions can be made about certain problem defining parameters. Because of their very large geometry, the optical depth obviously is large, too:

$$\tau_0 \gg 1. \quad (3.44)$$

As the following derivation rests on this assumption, we can apply the approximation in other optically thick cases. Since many kinds of glass have large absorption coefficients, problems such as glass furnaces and feeder channels can be characterised as optically thick.

Rosseland multiplied (2.32) with \mathbf{s} and integrated the result over all directions to arrive at

$$\mathbf{q}_v = -\frac{1}{\kappa_v} \nabla \cdot \mathbf{P}_v, \quad (3.45)$$

where \mathbf{P}_v is the radiation tensor defined in (2.23). He then continued by splitting the intensity I_v in $I_v(\mathbf{x}, \mathbf{s}) = \bar{I}_v(\mathbf{x}) + I'_v(\mathbf{x}, \mathbf{s})$. Component \bar{I}_v is the average of the intensity over all directions as defined by (2.20), whereas I'_v stands for the deviation from this average. Because of its definition, a similar split can be made for \mathbf{P}_v by splitting its elements into $p_{v,ij} = \bar{p}_{v,ij} + p'_{v,ij}$, with

$$\bar{p}_{v,ij} = \int_{\mathbb{S}^2} \bar{I}_v s_i s_j d\omega = \frac{1}{3} G_v \delta_{ij}, \quad (3.46)$$

$$p'_{v,ij} = \int_{\mathbb{S}^2} I'_v s_i s_j d\omega, \quad (3.47)$$

where δ_{ij} is the Kronecker delta. According to (2.32) this means that I_v is close to B_v . Since B_v is independent of the direction, it means that I_v is close to its directional average \bar{I}_v . Thus it follows that $I'_v/\bar{I}_v \ll 1$ and $|p'_{v,ij}/\bar{p}_{v,ij}| \ll 1$. The assumption of optical thickness in (2.39) leads to the approximation $G_v \approx 4\pi B_v$. So it is found that the radiation tensor can be approximated by

$$p_{v,ij} = \frac{4\pi}{3} B_v \delta_{ij}, \quad (3.48)$$

and consequently the heat flux by

$$\mathbf{q}_v = -\frac{1}{\kappa_v} \nabla \cdot \left(\frac{4\pi}{3} B_v \right) = -\frac{4\pi}{3\kappa_v} \nabla B_v. \quad (3.49)$$

The total heat flux is then found by integrating (3.49) over all frequencies:

$$\mathbf{q}_r = \int_0^\infty \mathbf{q}_\nu d\nu = -\frac{4\pi}{3} \int_0^\infty \frac{1}{\kappa_\nu} \nabla B_\nu d\nu = -\frac{4\pi}{3} \int_0^\infty \frac{1}{\kappa_\nu} \frac{dB_\nu(T)}{dB(T)} \nabla B d\nu = -\frac{4\pi}{3\kappa_R} \nabla B. \quad (3.50)$$

Here we introduced the *Rosseland mean absorption coefficient*, which is defined by

$$\frac{1}{\kappa_R} := \int_0^\infty \frac{1}{\kappa_\nu} \frac{dB_\nu(T)}{dB(T)} d\nu. \quad (3.51)$$

Together with the definition of B_ν in (2.4), we find the divergence of the heat flux to be

$$\nabla \cdot \mathbf{q}_r = -\nabla \cdot (\kappa_R \nabla T), \quad (3.52)$$

where we have introduced the *Rosseland diffusion coefficient* which is found to be

$$\kappa_R := \frac{16\pi \bar{\sigma} n^2}{3\kappa_R} T^3, \quad (3.53)$$

where it is assumed that the refractive index is constant. So, the Rosseland approximation leads to a diffusion-like expression. Because it was assumed that the problem is optically thick, the non-local effects of radiation were neglected: it is this assumption that replaces heat transport through photons by heat transport through phonons. It has been shown, that this approximation gives good results, as long as the assumption of optical thickness is not violated: e.g. in the centre of glass melts in furnaces, Rosseland's approximation is adequate. In many areas in glass production such an assumption cannot validly be made, leading to huge errors as shown in [Laevksy et al., 1999].

Section 3.2.3 discusses the results obtained with the Rosseland method for a geometry that is optically thick and another geometry which is not optically thick. The solutions to those example problems are shown in Figure 3.4 and Figure 3.5. A detailed discussion of these results can be found in the section mentioned.

To estimate the accuracy of the Rosseland approximation, we return to the one-dimensional case. Furthermore, we assume that the walls are at $x = -\infty$ and $x = \infty$, so that there is no contribution from them, and that the medium is grey. In that case, the heat flux following from (3.19) reads

$$\frac{dq_r}{dx} = 4\pi\kappa B(x) - 2\pi\kappa^2 \int_{-\infty}^\infty E_1(\kappa|x-s|)B(s) ds. \quad (3.54)$$

The integral in this equation can be written as

$$\int_{-\infty}^\infty E_1(\kappa|x-s|)B(s) ds = \int_0^\infty E_1(x)\{B(x+t) + B(x-t)\} dt. \quad (3.55)$$

Integrating this by parts and using the properties listed in Appendix A, we find

$$\begin{aligned} & \int_0^\infty E_1(x)\{B(x+t) + B(x-t)\} dt = \\ & - \left[\frac{1}{\kappa} E_2(\kappa t) \{B(x+t) + B(x-t)\} \right]_0^\infty + \frac{1}{\kappa} \int_0^\infty E_2(\kappa t) \{B'(x+t) - B'(x-t)\} dt = \\ & \frac{2}{\kappa} B(x) + \frac{1}{\kappa} \int_0^\infty E_2(\kappa t) \{B'(x+t) - B'(x-t)\} dt. \quad (3.56) \end{aligned}$$

where we used the notation B' for the first derivative of $B(x)$. If we repeat the integration by parts several more times, we end up with

$$\int_{-\infty}^{\infty} E_1(\kappa|x-s|)B(s) ds = \frac{2}{\kappa}B(x) + \frac{2}{3\kappa^3}B''(x) + \frac{1}{\kappa^4} \int_{-\infty}^{\infty} E_5(\kappa|x-s|)B^{(4)}(s) ds, \quad (3.57)$$

where B'' is the second derivative and $B^{(4)}$ the fourth. When we substitute this back into (3.54), we find

$$\frac{dq_r}{dx} = -\frac{4\pi}{3\kappa}B''(x) + r(x). \quad (3.58)$$

The first term corresponds to the Rosseland approximation, while the second term is the residual or error caused by this approximation:

$$r(x) := -\frac{2\pi}{\kappa^2} \int_{-\infty}^{\infty} E_5(\kappa|x-s|)B^{(4)}(s) ds. \quad (3.59)$$

Now, let M_B be the supremum of the fourth derivative of $B(x)$:

$$M_B := \sup_x |B^{(4)}(x)|, \quad (3.60)$$

then the residual can be estimated by

$$|r(x)| \leq \frac{2\pi}{\kappa^2} \int_{-\infty}^{\infty} E_5(\kappa|x-s|)M_B ds = \frac{4\pi}{5\kappa^3}M_B. \quad (3.61)$$

So, in absence of influence of the boundaries the Rosseland approximation can be expected to work quite well for high values of the absorption coefficient, as long as the fourth derivative of the blackbody intensity distribution is limited. When boundaries are present however, we face a different situation. Obtaining the residual for the one-dimensional case with black boundaries at $x = 0$ and $x = L$ can be done in a similar fashion as shown above. If we furthermore assume that conduction is present such that the temperature in the medium at the walls is equal to the temperature of those walls, the same holds true for the blackbody intensity:

$$B(0) = B_0 \text{ and } B(L) = B_1.$$

In that case the residual can be found to be

$$r(x) = r_0(x) + r_1(x) + r_d(x), \quad (3.62)$$

with $r_0(x)$ being the residual caused by the boundary at $x = 0$ and $r_1(x)$ the residual caused by the wall at $x = L$; $r_d(x)$ is the residual caused by phonon approximation. These are given by

$$r_0(x) = -2\pi B'(0)E_3(\kappa x) + \frac{2\pi}{\kappa}B''(0)E_4(\kappa x) - \frac{2\pi}{\kappa^2}B'''(0)E_5(\kappa x), \quad (3.63)$$

$$r_1(x) = 2\pi B'(L)E_3(\kappa(L-x)) + \frac{2\pi}{\kappa}B''(L)E_4(\kappa(L-x)) + \frac{2\pi}{\kappa^2}B'''(L)E_5(\kappa(L-x)), \quad (3.64)$$

$$r_d(x) = -\frac{2\pi}{\kappa^2} \int_0^L E_5(\kappa|x-s|)B^{(4)}(s) ds. \quad (3.65)$$

Application	L	d_R (green)	d_R (white)
furnace	100 cm	5.4 cm	35.5 cm
feeder	10 cm	3.6 cm	17.4 cm
parison	1 cm	1.7 cm	1.1 cm

Table 3.2: The Rosseland depth d_R for a linear temperature profile ($T_0 = 1000^\circ\text{C}$, $T_1 = 1200^\circ\text{C}$) for green bottle glass ($\kappa = 350\text{ m}^{-1}$) and white float glass ($\kappa = 35\text{ m}^{-1}$).

The last residual can be estimated by

$$|r_d(x)| \leq \frac{4\pi}{5\kappa^3} (1 - 5E_6(\frac{1}{2}\kappa L)) M_B. \quad (3.66)$$

As can be seen the main error does not result from the phonon approximation but from the wall effects. Since the Rosseland approximation reduces radiation to a phenomenon that is local, the heat flux within the medium is calculated without using the conditions at the boundary. If a boundary is not perfectly insulated, we have $(dT/dx) \neq 0$ at the boundaries, and consequently $B'(0) \neq 0$ and $B'(L) \neq 0$. The Rosseland approximation therefore only works correctly far enough from the boundaries. If the gradient of the temperature at the boundary is known, the first term in (3.63) offers a method to estimate the depth where the Rosseland operates within a given accuracy.

Since $|r_0(x)|$ decreases monotonously as the distance to the boundary increases, we can find a distance from the boundary where the size of this residual is equal to the size of ‘phonofication’-residual $r_d(x)$. Therefore, we define the *Rosseland depth* d_R as the distance from the boundary where we have

$$|r_0(d_R)| \leq \sup_{x \in (0, L)} |r_d(x)|. \quad (3.67)$$

This distance can be estimated by a combination of (3.63) and (3.66):

$$E_3(\kappa d_R) < \frac{2}{5\kappa^3} \sup_{\mathbf{x} \in \Omega} |\nabla^4 B(\mathbf{x})| \bigg/ \max_{\mathbf{x} \in \mathbf{x}_r} \|\nabla \cdot B(\mathbf{x})\|, \quad (3.68)$$

of which the solution needs to be found numerically. Note that since $E_3(x)$ is monotonously decreasing smaller values on the right-hand side lead to higher values of d_R .

In Table 3.2 computed values of d_R are displayed for the green and white glasses. From this table it is clear that only for the green glass in a furnace environment with a typical depth of 1 m the Rosseland approximation can be used satisfactorily throughout the most of the domain. For the white glass and for thinner geometries another method should be applied. Note, that the Rosseland depth d_R only gives an estimate for the required depth such that the error due to boundary effects is of the same order as the error introduced by the phonon approximation. So, it has to be verified that $|r_d|$ is small. For the linear temperature profile used to compute these numbers, this poses no problems.

Although the temperature profile used for Table 3.2 is very different from that used for Figure 3.4, we see that the estimate d_R is of the same order of magnitude

of the depth where the Rosseland approximations starts to agree with the exact solution in that figure. The computed value is about two to four times as large as what visual inspection of the figure would suggest. This means that the Rosseland depth can be estimated properly using (3.68) for a simplified temperature profile.

We have seen that close to the boundary the Rosseland approximation always leads to significant errors. However, because of its low computational costs the Rosseland approximation can be used within an area of the domain that has a distance to the boundary of at least the Rosseland depth. For the area close to the boundary and for the geometries for which the Rosseland approximation is unfit, other more elaborate methods need to be applied.

The Rosseland approximation avoids the computation of the intensity. Yet, when combined with another method the intensity might need to be known at the interface between the domains where the different methods are used. To retrieve the intensity, we can make use of (2.39), which, rephrased, states that the directionally average intensity satisfies

$$\bar{I}_\nu(\mathbf{x}) = B_\nu(\mathbf{x}) - \frac{1}{4\pi\kappa_\nu} \nabla \cdot \mathbf{q}_\nu(\mathbf{x}). \quad (3.69)$$

Since the Rosseland approximation considers radiation to be a local phenomenon, the resulting radiation is isotropic, i.e. equal to the directional average. Hence, we can use

$$I_\nu(\mathbf{x}, \mathbf{s}) = B_\nu(\mathbf{x}) + \frac{1}{3\kappa_\nu^2} \nabla^2 B_\nu(\mathbf{x}), \quad (3.70)$$

where we assumed a constant absorption coefficient.

3.2.2 Modified Diffusion Approximation

Because Rosseland's method is not universally applicable in heat computations, various people have sought to improve upon Rosseland's approximation by modified diffusion approximations. This class of approximations, do only replace a part of the radiative heat transfer by a diffusion-like term, while accounting differently for the non-local effects. A recent example is given by Siedow and Lenten in [Lenten and Siedow, 1998, Lenten and Siedow, 1999], which constructs an improved Rosseland approximation by a Taylor expansion of the blackbody intensity $B_\nu(\mathbf{x})$ around a point of interest \mathbf{x}_0 , so in terms of $\mathbf{x} - \mathbf{x}_0$:

$$B_\nu(\mathbf{x}) \doteq B(\mathbf{x}_0) + (\mathbf{x} - \mathbf{x}_0) \cdot \nabla B(\mathbf{x}_0). \quad (3.71)$$

This approximation can be substituted into (2.34) to find an approximation for the intensity at \mathbf{x}_0 :

$$\begin{aligned} I_\nu(\mathbf{x}_0, \mathbf{s}) &\doteq I_\nu(\mathbf{x}_\Gamma, \mathbf{s}) e^{-\kappa_\nu \|\mathbf{x}_0 - \mathbf{x}_\Gamma\|} + B_\nu(\mathbf{x}_0) \\ &\quad - B_\nu(\mathbf{x}_\Gamma) e^{-\kappa_\nu \|\mathbf{x}_0 - \mathbf{x}_\Gamma\|} - \frac{1}{\kappa_\nu} \left(1 - e^{-\kappa_\nu \|\mathbf{x}_0 - \mathbf{x}_\Gamma\|}\right) \mathbf{s} \cdot \nabla B_\nu(\mathbf{x}_0), \end{aligned} \quad (3.72)$$

with \mathbf{x}_Γ being the first intersection with the boundary of the ray leaving \mathbf{x} into direction $-\mathbf{s}$. Note, that this approximation does not follow directly from integrating the Taylor expansion. In that case the term $-B_\nu(\mathbf{x}_\Gamma) e^{-\kappa_\nu \|\mathbf{x}_0 - \mathbf{x}_\Gamma\|}$ would

be replaced by $-B_\nu(\mathbf{x}_0)e^{-\kappa_\nu\|\mathbf{x}_0-\mathbf{x}_r\|}$. Replacing the $B_\nu(\mathbf{x}_0)$ with $B_\nu(\mathbf{x}_r)$, however, leads to a simpler expression for the contribution of the boundary later on. As in Rosseland's approximation, this expression for the intensity is multiplied by \mathbf{s} and integrated over all directions in order to find the heat flux:

$$\mathbf{q}_\nu = \int_{\mathbb{S}^2} \mathbf{s} [I_\nu(\mathbf{x}_r, \mathbf{s}) - B_\nu(\mathbf{x}_r)] e^{-\kappa_\nu\|\mathbf{x}-\mathbf{x}_r\|} d\omega - \frac{1}{\kappa_\nu} \int_{\mathbb{S}^2} \mathbf{s} (\mathbf{s} \cdot \nabla B_\nu) \{1 - e^{-\kappa_\nu\|\mathbf{x}-\mathbf{x}_r\|}\} d\omega. \quad (3.73)$$

For large optical depth, this simplifies to Rosseland's approximation: the first integral, taking the contribution of the boundary into account, disappears as $\exp(-\kappa_\nu\|\mathbf{x}-\mathbf{x}_r\|)$ tends to zero. Also in the second integral the exponent disappears. This exponent accounts for the fact that the domain is finite. So, for large optical depth the heat flux is written as

$$\mathbf{q}_\nu = -\frac{1}{\kappa_\nu} \int_{\mathbb{S}^2} \mathbf{s} (\mathbf{s} \cdot \nabla B_\nu) d\omega, \quad (3.74)$$

which indeed evaluates to the divergence found for the Rosseland approximation in (3.52). Taking the divergence of the radiative heat flux in (3.73), we find:

$$\nabla \cdot \mathbf{q}_\nu = \kappa_\nu \int_{\mathbb{S}^2} [I_\nu(\mathbf{x}_r, \mathbf{s}) - B_\nu(\mathbf{x}_r)] e^{-\kappa_\nu\|\mathbf{x}-\mathbf{x}_r\|} d\omega - \nabla \cdot \left(\frac{1}{\kappa_\nu} A_\nu \nabla B_\nu \right), \quad (3.75)$$

where $I_\nu(\mathbf{x}_r, \mathbf{s})$ has to be determined using radiative boundary conditions. Diffusion tensor A_ν in this relation is depending on the geometry and is given by:

$$A_\nu(\mathbf{x}) = (a_{\nu,ij}(\mathbf{x})), \text{ with } a_{\nu,ij}(\mathbf{x}) = \int_{\mathbb{S}^2} s_i s_j [1 - e^{-\kappa_\nu\|\mathbf{x}-\mathbf{x}_r\|}] d\omega. \quad (3.76)$$

Because of the fact that $\int_{\mathbb{S}^2} s_i s_j d\omega = \delta_{ij}$, where δ is the Kronecker delta, and that for large optical depth $(1 - e^{-\kappa_\nu\|\mathbf{x}-\mathbf{x}_r\|}) \approx 1$, the off-diagonal terms can be neglected. This means this modified diffusion approximation can be implemented easily using diffusion methods in existing software.

The accuracy of this approach can be studied by comparing it to the exact solution for a problem with black boundaries as was done in Section 3.1. For a one-dimensional problem the modified diffusion approximation can also be stated in a simplified manner. For that purpose, we assume conduction is present, so there are no discontinuities at the boundary: $B(0) = B_0$ and $B(L) = B_1$, where L is the distance between the two boundaries. Since the blackbody intensity here only varies with the x -direction, we are only interested in the value of $a_{\nu,11}$. The distance between a point x and the boundary in a specific direction is x/μ for the left boundary and $(L-x)/\mu$ for the other. With these definitions the coefficient $a_{\nu,11}$ is found to be

$$\begin{aligned} a_{\nu,11} &= \int_{\varphi=0}^{2\pi} \int_{\mu=0}^1 \mu^2 (2 - e^{-\kappa x/\mu} - e^{-\kappa(L-x)/\mu}) d\mu d\varphi \\ &= \frac{4\pi}{3} - 2\pi E_4(\kappa x) - 2\pi E_4(\kappa(L-x)). \end{aligned} \quad (3.77)$$

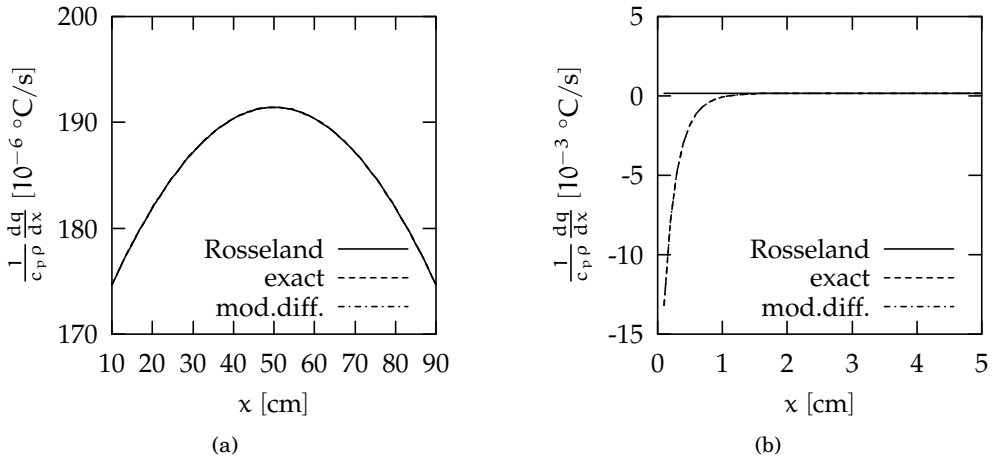


Figure 3.4: Comparison of $\nabla \cdot \mathbf{q}_r$ calculated exactly, using the Rosseland approximation and using the modified diffusion approximation of Section 3.2.2 in a 1 m thick slab geometry filled with the green glass from Table 3.1: (a) Inside the domain the three curves coincide. (b) Near the boundary the curves of the exact solution and the modified diffusion approximation coincide, while the Rosseland approximation deviates.

Furthermore, taking the black boundaries into account, the divergence of the heat flux simplifies to

$$\frac{\partial q}{\partial x} = -\frac{\partial}{\partial x} \left[\frac{2\pi}{3\kappa} \left\{ 2 - 3E_4(\kappa x) - 3E_4(\kappa(L-x)) \right\} \frac{\partial B}{\partial x} \right]. \quad (3.78)$$

Note that the first term on the right-hand side in (3.73) disappears, because of the assumption of black boundaries: The emitted intensity in a point \mathbf{x}_Γ on the boundary is equal to the blackbody intensity there. For increasing κ , the terms involving the exponential integrals converge to zero, so we would return to the Rosseland approximation. The results of the modified diffusion method are compared with the Rosseland approximation and the exact solution in the next subsection.

A drawback of this method, that we did not encounter in the simple case of a one-dimensional problem with black boundaries, is the fact that the intensity at the boundary has to be known *a priori*. To that purpose a two scale analysis in [Klar and Siedow, 1999] leads to a set of equations at the boundary. However, in [Lentes and Siedow, 1998] itself, Siedow and Lentes propose a ray trace approach for the boundary, which seems to give better results. A variant of the ray trace method is presented in the next chapter. Parts of that method — viz. the computation of boundary radiation — can be used for the modified diffusion method.

3.2.3 Comparison

Since we can compute the divergence of the radiative heat flux exactly in one dimension, we can obtain a good indication of the accuracy of the diffusion approximations by comparing them in a one-dimensional geometry. Because the

assumption of optical thickness was essential for the derivation of both diffusion approximation that we have shown here, we consider two geometries: one optical thick slab geometry, where the assumption of optical thickness is valid, and one slab geometry that violates that assumption. In both cases we use the green glass from Table 3.1 as the semi-transparent medium. The first geometry is chosen to have a depth of 1 m, corresponding to the depth of the glass bath in a furnace, while the other geometry has a depth of 1 cm, which corresponds to a typical depth of a *parison*, a half-product in the production of glass bottles. In both cases, a parabolic temperature profile is imposed with $T = 1000^\circ\text{C}$ at the boundaries and $T = 1020^\circ\text{C}$ in the middle.

The Rosseland approximation, modified diffusion approximation and exact solution for the optical thick case are shown in Figure 3.4. The figure displays the heat flux divergence $\nabla \cdot \mathbf{q}_r / (\rho c_v)$ which would represent the rate of cooling in absence of other modes of heat transfer. In this situation the optical depth is $\tau_0 = 350$. Since the optical depth is large, this figure shows there is good agreement in the centre of the domain, where the curves all coincide as can be seen in the first graph. However, there are significant aberrations near the boundary for the Rosseland approximation. The modified diffusion approximation performs very well near the boundaries, too, thanks to the special treatment of these boundaries.

In Figure 3.5, the same comparison is displayed for the geometry that is not optically thick. For this one centimetre thick slab of green glass, the optical depth is $\tau_0 = 3.5$, which is not significantly larger than unity. Since the assumption of optical thickness is not valid here, the figure shows an abysmal performance of the Rosseland approximation and not much improvement for the modified diffusion method, showing the main error here is due to treating radiation as diffusion, rather than due to boundary effects.

From the figures it can be concluded that the Rosseland approximation provides good solutions, as long as it is used not closer than a distance d_R from the boundary. In the region closer to the boundary the modified diffusion approximation may be used for good results. However, in higher dimensional problems or when reflections are present, obtaining the terms dependent on the boundary may prove quite laborious. For geometries that are not optically thick, neither of the diffusion approximations works well. This is not surprising, as the basic assumption upon which these methods rely, is not valid in that case: radiation cannot be considered to be a local effect. Because of these considerations and the fact that many applications in glass production are not optically thick, we consider alternatives for this class of approximations, in the remainder of this chapter and the next.

3.3 Discrete Ordinate Method

For numerical approaches it is impossible to solve the radiative transfer equation (2.32) for every direction \mathbf{s} . Logically, only a limited number of directions might be chosen to solve this equation. Together with this set of directions an appropriate quadrature is needed for the integrals involving integration over the directions. This transformation of direction space is called the *Discrete Ordinate*

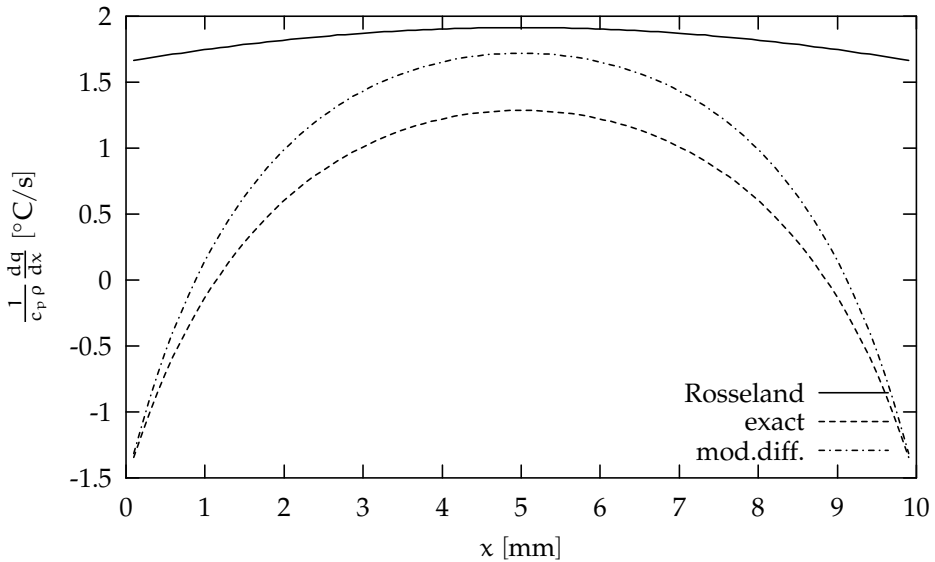


Figure 3.5: Comparison of $\nabla \cdot \mathbf{q}_r$ calculated exactly, using the Rosseland approximation and using the modified diffusion approximation of Section 3.2.2 in a 1 cm thick slab geometry filled with the green glass from Table 3.1.

Method or DOM in short:

$$\text{DOM} : (\mathbb{S}_2, W) \rightarrow (\mathcal{S}_2, W_{\mathcal{S}}), \quad (3.79)$$

where \mathcal{S}_2 is a set of N directions defined by

$$\mathcal{S}_2 := \{\mathbf{s}_i \mid \mathbf{s}_i \in \mathbb{S}_2, i = 1, 2, \dots, N\} \quad (3.80)$$

and $W_{\mathcal{S}}$ is some operator such that

$$(W_{\mathcal{S}}\mathbf{f})(\mathbf{x}) \doteq (W\mathbf{f})(\mathbf{x}), \quad (3.81)$$

for a vector function $\mathbf{f}(\mathbf{x})$ whose elements satisfy $f_i(\mathbf{x}) = f(\mathbf{x}, \mathbf{s}_i)$, $i = 1, 2, \dots, N$. $W_{\mathcal{S}}$ is a quadrature that can be written more conveniently as a vector \mathbf{w} :

$$(W_{\mathcal{S}}\mathbf{f})(\mathbf{x}) = \mathbf{w} \cdot \mathbf{f}(\mathbf{x}) = \sum_i w_i f_i(\mathbf{x}). \quad (3.82)$$

The chosen quadrature should certainly be exact for a function that is independent of direction:

$$\sum_i w_i = \int_{\mathbb{S}_2} d\omega = 4\pi. \quad (3.83)$$

The RTE can then be written as

$$\mathbf{s}_i \cdot \nabla I_{\nu}(\mathbf{x}, \mathbf{s}_i) + \kappa_{\nu} I_{\nu}(\mathbf{x}, \mathbf{s}_i) = \kappa_{\nu} B_{\nu}(\mathbf{x}), \quad \mathbf{s}_i \in \mathcal{S}_2 \quad (3.84)$$

and the heat flux can be found using a variation of (2.39):

$$\nabla \cdot \mathbf{q}_{\nu}(\mathbf{x}) \doteq 4\pi B_{\nu}(\mathbf{x}) - \sum_{\mathbf{s}_i \in \mathcal{S}_2} w_i I(\mathbf{x}, \mathbf{s}_i). \quad (3.85)$$

While the choice of directions would be a simple case in a two-dimensional space, the fact that \mathbb{S}_2 is not a Euclidean space complicates things. To make the direction set work equally well for a number of geometries, the directions should be spread as evenly over the space as possible. If this would not be the case, the result of the subsequent computations are depending on the alignment of the direction sphere in space. In [Bressloff et al., 1995], it was shown that having a near homogeneous direction set indeed improved the accuracy in a radiation problem in a non-participating medium. Recalling that

$$\mathbf{s} = \begin{pmatrix} \cos \varphi \sin \vartheta \\ \sin \varphi \sin \vartheta \\ \cos \vartheta \end{pmatrix}, \quad (3.86)$$

where $\varphi \in [-\pi, \pi]$ is the azimuthal angle and $\vartheta \in [0, \pi]$ is the zenith angle. As we did here, these two angles are usually defined as the angle around and with the positive z-axis respectively, but could be defined with respect to any other vector. The result of the quadrature should, of course, not depend on the choice of the alignment of the unit sphere in space. However, only through the five regular polyhedra a truly homogeneous direction set can be obtained, meaning that the largest homogeneous direction set only comprises twenty directions: for greater accuracy we need to find another approach.

3.3.1 Level Symmetric Sets

One approach that is often followed to construct a direction set, is the use of so-called Level-Symmetric Sets. In [Lathrop and Carlson, 1964], this approach is explained and tabulated. The essence of the method is to find a set of values (or levels) m_i , such that when the planes $x = m_i$, $y = m_j$ and $z = m_k$ have an intersection point with the sphere, so do the groups of planes with the levels permuted. This makes the direction set symmetric on ninety degree rotations, but also puts a constraint on the levels m_i :

$$m_i^2 = m_1^2 + 2(i-1) \frac{1-3m_1^2}{n-2}, \quad (3.87)$$

where n is the number of levels per axis. This factually leaves only the first level as a degree of freedom for choosing the directions. To pertain the symmetry furthermore reduces the degrees of freedom in choosing the point weights.

In Figure 3.6, the level symmetric set S_{12} is portrayed. The figure marks directions by dots and gives an indications of the weight by means of colour. The weights haven been scaled such that a value of 1 represents equality with $w = 4\pi/N$, the truly homogeneous case. The solid lines mark the Voronoi regions for the different directions. As we can see there is a ϑ -band where the weights are relatively low. Due to all the symmetry requirements, this band extends over all φ , meaning these effects along these directions are underrepresented. On the other hand there are also larger Voronoi regions, marked by a darker colour in the figure. In these parts of the direction domain the resolution will be smaller.

So, while direction sets constructed following this approach are symmetric, the weights for the various directions vary strongly. Before, however, we already argued that a direction set and the direction weights should be distributed homogeneously rather than symmetrically. Symmetry here refers to symmetry between

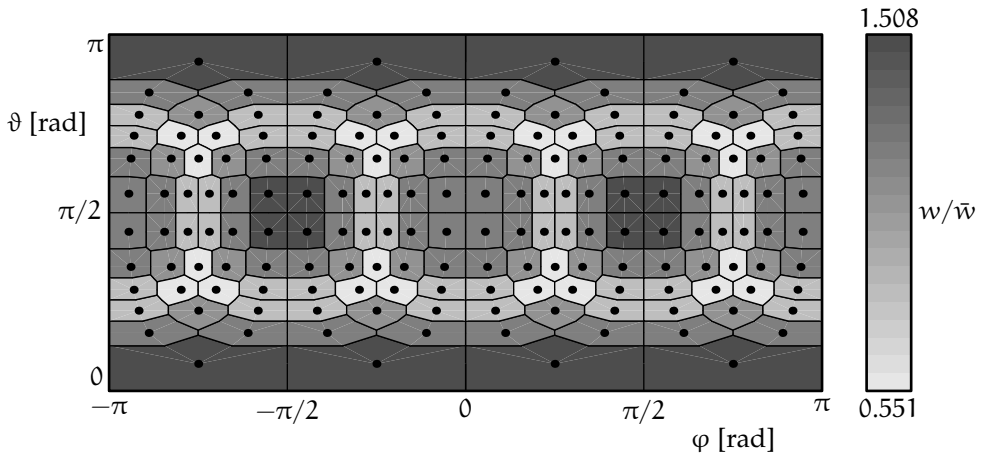


Figure 3.6: Directions and weight distribution in spherical coordinates for the level symmetric set S_{12} from [Lathrop and Carlson, 1964] comprising a total of 168 directions. The directions themselves are marked by dots.

the octants and under rotations of ninety degrees, not to the homogeneity of the distribution of the directions within an octant.

3.3.2 Quasi-Homogeneous Sets

In [Slob, 1997], a different approach which tries to achieve an as good as possible homogeneity. He chooses the analogy with electrons confined to the shell of a sphere. Since the electrons repel each other, they maximise the distance between them. This does not lead to a homogeneous set, where the distance between all neighbouring electrons would be the same — which is impossible for an arbitrary number of directions — but approximates this situation closely. Since the reference is rather brief about the details of such an approach, we study it a bit deeper here.

The force between electrons is reciprocal to the square of the distance. As can be found in many introductory books to electricity as [Buijze, 1989], Coulomb's Law states that the electrical force \mathbf{F}_i on a charge q due to a charge Q_i be

$$\mathbf{F}_i = \frac{1}{4\pi\epsilon_0} \frac{Q_i q}{r_i^2} \frac{\mathbf{r}_i}{r_i}, \quad (3.88)$$

where ϵ_0 is the *electrical permittivity*, \mathbf{r}_i is the vector from Q_i to q , and r_i is the size of that vector. Usually, instead of expressing the force due to Q_i on a test charge q , the electrical field is used

$$\mathbf{E}_i := \frac{\mathbf{F}_i}{q} = \frac{Q_i}{4\pi\epsilon_0 r_i^3} \mathbf{r}_i. \quad (3.89)$$

This field is a potential field, so we can write

$$\mathbf{E}_i = -\nabla V_i, \text{ with } V_i := \frac{Q_i}{4\pi\epsilon_0 r_i}, \quad (3.90)$$

where V_i is called the *electrical potential* and r_i now stands for the distance to the source. For an N charged particle system, the potential can be summed. When we look at the potential of a particle Q_i in an N particle system the potential of that particle is

$$V_i = \sum_{j \neq i} \frac{Q_j}{4\pi\epsilon_0 r_{ij}}, \quad (3.91)$$

with r_{ij} the distance from the source charges to the charge under consideration. The *electrical potential energy* U_e is closely related to this quantity. For the whole system this potential energy is equal to

$$U_e = \sum_i Q_i V_i = \frac{1}{2} \sum_i \sum_{j \neq i} \frac{Q_i Q_j}{4\pi\epsilon_0 r_{ij}}. \quad (3.92)$$

The quasi-homogeneous direction set then can be found by minimising this potential energy. For homogeneity, we take only unit charges and to further simplify the equation we choose $\epsilon_0 = 1/4\pi$. This means the direction can be found using the following minimisation problem:

$$\min_{\mathbf{s}_1, \mathbf{s}_2, \dots, \mathbf{s}_N \in \mathbb{S}_2} \frac{1}{2} \sum_{i=1}^N \sum_{\substack{j=1 \\ j \neq i}}^N \frac{1}{\|\mathbf{s}_i - \mathbf{s}_j\|}. \quad (3.93)$$

Since we restrict the particles to a certain space, the minimal potential energy is not obtained when the electrical field vanishes at the position of each particle. The latter can never be achieved when we restrict the particles to the shell of the unit sphere. Rather the minimum is obtained when

$$\sum_{j \neq i} \left\{ \mathbf{E}_j - (\mathbf{E}_j \cdot \mathbf{s}_i) \mathbf{s}_i \right\} = \mathbf{0}, \text{ for all } i, \quad (3.94)$$

i.e. when the electrical field is oriented perpendicular to the unit sphere at the location of each particle. This means that the particles are aligned homogeneously with respect to each other. As stated before such a situation can only be attained for a certain number of particles when they are not co-planar, but the solution to (3.93) gives the best approximation.

For better homogeneity, we argue that the centre of mass of these electrons should be in the origin. If it were not, it would mean that some part of the sphere has a higher electron density than another, and therefore would have a preference for a certain group of directions. This approach also has numerical advantages as the number of independent variables in (3.93) decreases eight-fold. Furthermore, as is shown next this distribution has beneficial effects in the computation of the weights, too.

When the directions are known, the weights still need be determined. Whereas in [Slob, 1997] constant weights seem to be taken, we choose a slightly different approach. The Voronoi diagram in Figure 3.7 shows that — since the final position of the electrons do not define a regular solid — the areas would be (slightly) different. Please note, that the projection used in the figure exaggerates the area near the poles $\vartheta = 0$ and $\vartheta = \pi$. It seems natural therefore that each direction

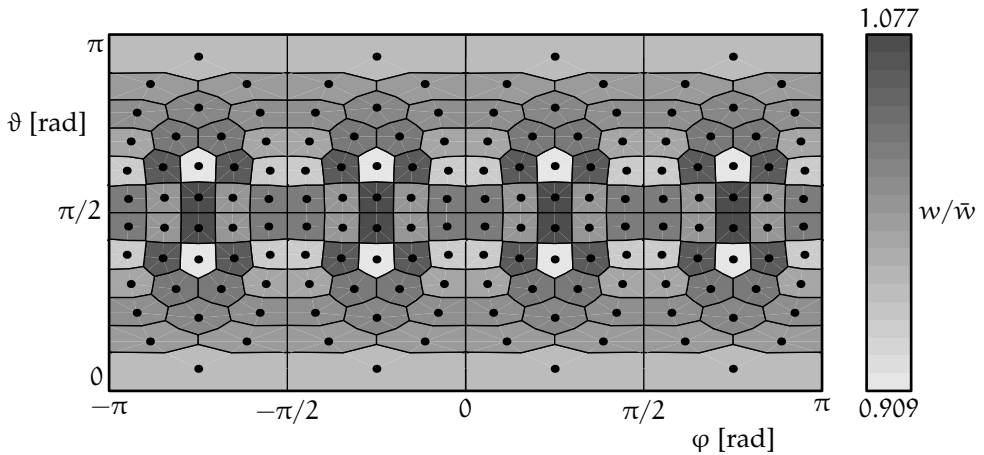


Figure 3.7: Directions and weight distribution in spherical coordinates for an octant-symmetric quasi-homogeneous direction set with 160 directions. The directions are marked by dots. Weights were computed with $p = 24$ in (3.97).

should receive its own weight. We can compute these weights by requiring that a number of moments are integrated exactly.

Let s_x be the x -component of the direction vector and let the other components be defined similarly. Then the (i, j, k) -moment is defined by

$$M_{i,j,k} := \int_{\mathbb{S}_2} s_1^i s_2^j s_3^k d\omega. \quad (3.95)$$

These moments vanish unless all of the subscripts are even. In that case we find

$$M_{2i,2j,2k} := 2 \frac{\Gamma(\frac{1}{2} + i)\Gamma(\frac{1}{2} + j)\Gamma(\frac{1}{2} + k)}{\Gamma(\frac{3}{2} + i + j + k)}. \quad (3.96)$$

The quadrature weights can be computed by requiring that they integrate these moments exactly up to some order p :

$$\sum_{n=1}^N s_{1,n}^i s_{2,n}^j s_{3,n}^k w_n = M_{i,j,k}, \text{ for all } i + j + k \leq p. \quad (3.97)$$

If the directions are distributed symmetrically for each octant — as proposed before — all moments with one or more odd indices are integrated exactly by the quadrature. This means, only the all-even moments need to be considered.

The linear system generated by (3.97) is in general non-square, i.e. there are either more or less equations than unknowns. In these cases the system can be solved in a least-square sense. In Figure 3.7 the directions and weight distribution are displayed for a quasi-homogeneous set with 160 directions distributed symmetrically over the octants. The weights were submitted to the all-even moments (3.97) with $p = 24$. Comparing this figure to Figure 3.6, we observe similarity of the Voronoi diagram, where the latter seems to squeeze in extra directions due to the symmetry requirements with the octant. The effect of the

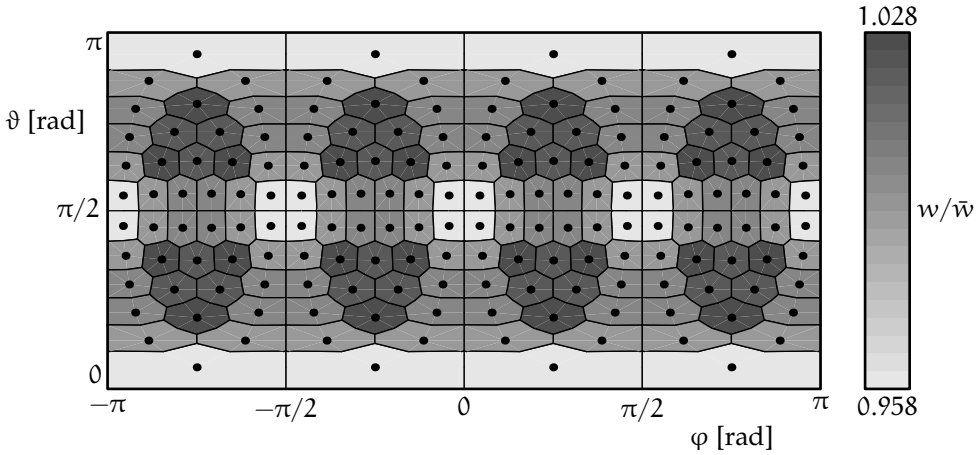


Figure 3.8: Directions and weight distribution in spherical coordinates for an octant-symmetric quasi-homogeneous direction set with 168 directions, corresponding to the number of directions of the S_{12} set of Figure 3.6. Weights were computed with $p = 24$ in (3.97).

non-homogeneity of the directions shows in the fact that the weights of the level-symmetric set vary much more than the quasi-homogeneous set.

At a 160 directions the quasi-homogeneous set lacks the symmetry within the octant, that we saw for the level-symmetric set. However, if we increase the number of directions slightly to 168, i.e. the number of directions in the S_{12} set, symmetry appears also in the direction set and weight distribution in the quasi-homogeneous direction set as is shown in Figure 3.8. Interestingly the weight distribution of this direction set varies even less, indicating that the number of directions should be chosen to allow for symmetry within the octant. From the level-symmetric sets we know that this means the number of directions should be computed by

$$N = 4n(n + 1), \quad n = 1, 2, \dots \quad (3.98)$$

In Figure 3.9(a), the behaviour of the standard deviation σ_w of the weights is displayed for the two sets with 160 and 168 directions. The standard deviation is computed as

$$\sigma_w := \sqrt{\frac{1}{N-1} \sum_{i=1}^N (w_i - \bar{w})^2}, \quad (3.99)$$

with \bar{w} being the mean weight. The standard deviation is a measure of how much variation occurs within the weight set. We see that a small increase in the number of directions, the weights become distributed more homogeneously even with an increasing number of spherical moments that have to be integrated exactly.

Figure 3.9(b) shows that this behaviour is by no means accidental. In that figure the normalised standard deviation, defined as σ_w/\bar{w} , is plotted against the number of directions. For number of directions in the figure only multiples of 8 were used, so all the the calculated direction sets where symmetrical over the octants. The figure shows that a local minimum is found for every number of directions

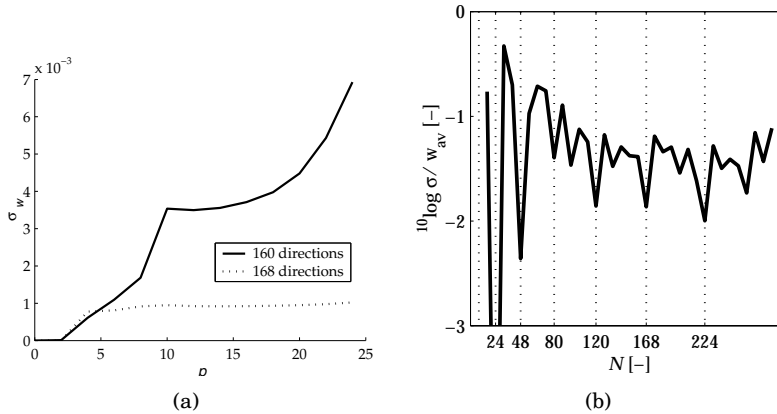


Figure 3.9: (a) Standard deviation of the weights as function of p for two octant-symmetric quasi-homogeneous sets with 160 and 168 directions respectively; (b) Normalised standard deviation as function of the number of directions.

following from (3.98), i.e. the number of directions used for the Level Symmetric Sets. By choosing those specific numbers, the resulting direction set is more homogeneous within the octant, as was already illustrated by the difference in Figures 3.7 and 3.8. Since the equations (3.97) are solved in a least-square sense, there is an associated residual to these equations, which is a measure for the (in)accuracy of the DOM at a specific level p . In Figure 3.10(a), this residual is shown as a function of p for the two sets with 160 and 168 directions respectively. Clearly, the extra homogeneity that is obtained for the set with N taken from (3.98) results in a residual that is much smaller. Since the restriction to the number of directions indicated by (3.98), leads to a more homogeneous distribution of the quadrature weights and to a lower residual, we restrict ourselves to these N in the remainder of this dissertation.

As the variance of the weights is quite small, we could be tempted to choose the weights constant after all. However, this has quite an impact on the residual to the equations (3.97) as can be noted from Figure 3.10. Here we see that the residual increases dramatically, especially for lower values of p . Choosing the number of directions according to (3.98) brings no benefit anymore. Because of the sharp increase of the residual and the fact that for a given direction set the weights only need to be computed once and for ever, approximating the quadrature weights by a constant is ill-advised.

3.3.3 Conclusion

In this section we have introduced the Discrete Ordinate Method and shown how to construct a direction set with appropriate quadrature weights. The first method, the Level Symmetric Sets worked out in [Lathrop and Carlson, 1964], provide one way to construct such sets. However, the constraints put on the directions means the quadrature weights vary over the unit sphere. Using such sets with the DOM would make certain directions more important than others. If the radiative field is known a priori, this could be used to align the direction sphere appropriately in physical space.

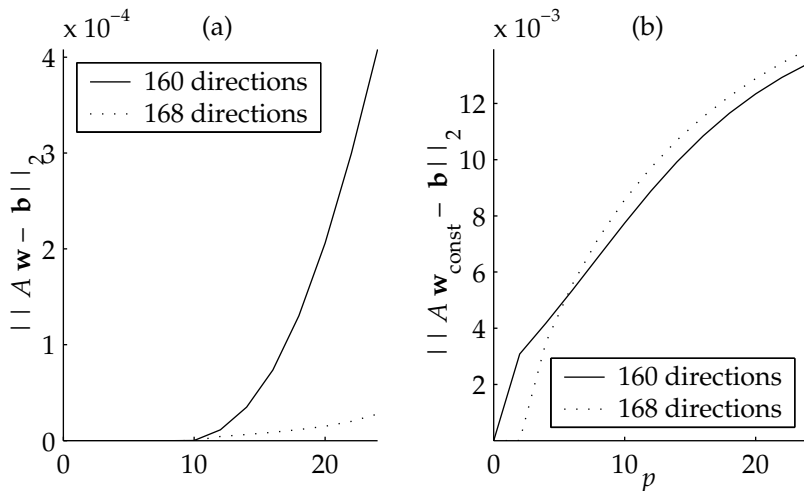


Figure 3.10: Residual to the equations (3.97) as a function of the maximum order p for a direction set with 160 and 168 directions. Figure (a) shows the residual for optimised weights, while (b) shows the residual if the weights were to be taken constant.

Unfortunately, we do not have much information about the directional distribution of the intensity beforehand. The RTE (2.32) only describes the intensity distribution along rays of constant direction, not over the direction space. Therefore, we would like to have a direction set which does not emphasise any particular direction. After an idea taken from [Slob, 1997], we worked out the quasi-homogeneous direction sets. This method releases most of the geometrical constraints imposed for the Level Symmetric Sets and relies on solving the minimisation problem (3.93). Although this minimisation problem gives a near homogeneous distribution of directions, the quadrature weights should not be taken constant. Here, we introduced the system (3.97) that imposes constraints on the weights, such that the resulting quadrature rule integrates spherical moments up to a certain order p optimally in a least-square sense. Furthermore, we found that both the best homogeneity is reached and the residual is minimised for numbers of directions required stemming from the Level Symmetric Set theory.

In the following sections and chapters we concentrate on solving the equations resulting from the directional discretisation of the RTE by the DOM. For the actual implementation we make use of the Quasi-Homogeneous Sets for the reasons outlined above.

3.4 Other methods

The approximative methods presented in this chapter failed to properly treat reflective boundaries, as they avoided the computation of the intensity. The intensity, after all, was used to formulate the boundary conditions for the RTE (2.32). In this section we have a brief look at various other existing methods. These vary from methods that are generally considered to be very accurate, yet computationally expensive such as the Ray Trace Method and Monte Carlo Method,

to variational formulations. Each of these methods has specific problems, that explain for the erroneous popularity of the Rosseland method and are therefore discussed only briefly.

3.4.1 Ray Tracing and Monte Carlo

Two methods that do accomplish proper treatment of reflective boundaries are the (classical) Ray Trace Method and the Monte Carlo Method. The Ray Trace Method, which is also referred to as the Discrete Transfer Method (DTM), e.g. in [Kuske, 1999, Uede et al., 2000], and as the Discrete Transfer Radiation Model (DTRM), see for example [Fluent, 1999], takes a domain divided in elements together with its temperature field. From the temperature field the amount of spontaneous radiation emitted by each element can be computed using Planck's function (2.2) or (2.4). From the discrete ordinate method a set of directions together with weights is obtained, and the emitted radiation can be distributed as starting intensities for rays emitted by the element at hand. Each ray is then followed, i.e. traced, along its path until the boundary is reached. For every element that is passed, the length of the path that the ray traverses through the element is measured. Using this length the change in intensity that the ray undergoes while traversing the element is computed. This change is subtracted from the intensity of the ray using a modified formulation of (2.33)

$$\frac{dI_\nu}{ds}(\mathbf{x}_0 + \zeta\mathbf{s}, \mathbf{s}) + \kappa_\nu I_\nu(\mathbf{x}_0 + \zeta\mathbf{s}, \mathbf{s}) = 0. \quad (3.100)$$

This modified version considers only absorption, and not emission, because the locally emitted radiation is tracked by another ray. Furthermore, the change in the intensity in the ray is added to the irradiance $G(\mathbf{x})$ of the element. When the ray reaches the boundary, the remaining energy in the ray is redistributed over the outgoing intensities at this boundary using the radiative boundary conditions.

After all the rays for every domain element are processed, the rays at the boundary are initiated using the intensity distribution caused by the remaining energy by the incoming rays and the spontaneous emission by the boundary itself. These rays, originating at the boundary are then processed the same way as before. Since these rays leave an amount of energy at some other boundary, iteration is necessary until all the energy has been processed. After this iteration has been finished, we know the irradiance in all elements in the domain and at the boundary and we can use (2.39), to compute the radiative heat flux divergence.

A major drawback of the Ray Trace Method is that it is computationally expensive. Every time the heat flux needs to be known, the whole domain has to be re-traced, and the iteration on the boundaries has to be redone. Let N be the number of directions, M the number of elements in the domain and M_Γ the number of elements on the boundary, then every time $N(M + M_\Gamma)$ rays have to be initiated. The number of elements that every ray crosses is proportional to $\sqrt[3]{M}$; so, it takes a number proportional to $NM\sqrt[3]{M}$, to distribute the radiative energy emitted by the domain elements. On top of these costs, there is the cost of the iterative redistribution of the radiative energy of the boundary elements. If this iteration takes k times, the total cost of the method is proportional to $NM\sqrt[3]{M} + kN\sqrt[3]{MM_\Gamma}$. Since less energy is absorbed by the domain, k increases

for optically thinner geometries. Depending on the geometry the first or second term will be dominant. For a cube subdivided in smaller cubes, the computational complexity is $NM\sqrt[3]{M} + kNM$, where it is to be noted that rarely $k > \sqrt[3]{M}$; so, in a compact geometry the first term is dominant. For an elongated geometry — e.g. a tower of stacked small cubes — the complexity is $NM\sqrt[3]{M} + kNM\sqrt[3]{M}$. Since in thin geometries k is larger, the second term is dominant for slender geometries.

A more conservative estimate, that eliminates the number of directions N , is found by the observation that the emitted energy in a node is ideally distributed over all mesh elements. Since this means M contributions from every one of the M nodes, M^2 contributions have to be computed for the first iteration step in that case. For each next iteration an additional $M\sqrt[3]{M}$. So, for a properly chosen number of directions, a total number of floating point operations proportional to $M^2 + kM\sqrt[3]{M}$ needs to be performed, where k again is the number of iterations needed.

The costs of the Ray Trace Method is further increased by the fact that the cost of the operations to redistribute the radiative energy themselves is high itself: the tracing of the ray means many intersections must be tested for each time a ray propagates to the next cell. Furthermore, the effort has to be repeated every time the temperature changes. These heavy costs make the Ray Trace Method unattractive. In Chapter 4, we present a method similar to this Ray Trace Method that tries to avoid some of the costs associated with ray tracing.

The accuracy of the Ray Trace Method can be taken even higher by applying a Monte Carlo approach. Very similar to the Ray Trace Method, the Monte Carlo approach first computes the spontaneously emitted energy for all elements in the domain. But rather than distributing this energy over outgoing rays in pre-defined directions, it is divided in small packets that are sent into random directions. As is done in [Yang et al., 1995], every energy packet gets an additional random number as an attribute, which determines after which optical distance it is absorbed by the medium, or boundary. After all the packets have been emitted and absorbed, the number of packets per element is counted, thus yielding the irradiance of that element. Finally, the heat flux divergence is obtained with (2.39).

Since physical models usually formulate how energy is converted, the Monte Carlo approach allows a straightforward implementation for a range of phenomena that are hard to implement with other methods, like cross-spectral reflections or scattering or complex spectra. Unfortunately, usually a very high number of packets is needed before the method gives accurate results. The high number of packets, in the end, make it even more expensive computationally than the Ray Trace Method. So, apart from special purpose simulations dealing with complex physical behaviour a Monte Carlo approach is usually not employed.

3.4.2 Finite Element Formulation

Heat problems involving conduction are commonly solved using a finite element (FEM) solution method. Unfortunately, the hyperbolic character of the RTE makes it unfit for this kind of solution method. To construct a suitable equation as was

done in [Fiveland, 1993], we can introduce the following quantities:

$$u(\mathbf{x}, \mathbf{s}) = \frac{1}{2}I(\mathbf{x}, \mathbf{s}) + \frac{1}{2}I(\mathbf{x}, -\mathbf{s}), \quad (3.101)$$

$$v(\mathbf{x}, \mathbf{s}) = \frac{1}{2}I(\mathbf{x}, \mathbf{s}) - \frac{1}{2}I(\mathbf{x}, -\mathbf{s}), \quad (3.102)$$

where we omitted the subscript signalling the dependence on the frequency. Writing out the RTE for the directions \mathbf{s} and $-\mathbf{s}$, we find that these variables obey the following two ODEs:

$$v_s(\mathbf{x}, \mathbf{s}) + u(\mathbf{x}, \mathbf{s}) = B(\mathbf{x}), \quad (3.103)$$

$$u_s(\mathbf{x}, \mathbf{s}) + v(\mathbf{x}, \mathbf{s}) = 0, \quad (3.104)$$

where we used the notation $f_s := df/ds = \frac{1}{\kappa}\mathbf{s} \cdot \nabla f$. The two variables can be separated by differentiation of (3.103). By subtracting and adding the results we obtain

$$-u_{ss}(\mathbf{x}, \mathbf{s}) + u(\mathbf{x}, \mathbf{s}) = B(\mathbf{x}), \quad (3.105)$$

$$-v_{ss}(\mathbf{x}, \mathbf{s}) + v(\mathbf{x}, \mathbf{s}) = -B_s(\mathbf{x}). \quad (3.106)$$

From these equations only the first needs to be solved, as from the definition of $u(\mathbf{x}, \mathbf{s})$, we see that

$$G(\mathbf{x}) = 2 \int_{\mathbb{H}_n^+} u(\mathbf{x}, \mathbf{s}) d\omega, \quad (3.107)$$

which then can be used in combination with (2.39) to compute the divergence of the heat flux. The vector \mathbf{n} with respect to which the hemisphere is defined, can be chosen arbitrarily. If the heat flux itself needs to be known, this has to be done through $v(\mathbf{x}, \mathbf{s})$, which can be obtained through (3.104).

For every direction \mathbf{s}_i given by the DOM, equation (3.105) can be further processed to come to a weak formulation of the problem, which then can be solved using finite elements. This approach, however, has three drawbacks. Firstly, (3.105) is a parabolic partial differential equation, written in its canonical form. It holds along the characteristic curve $\mathbf{x}_0 + \frac{s}{\kappa}\mathbf{s}$, so when it is integrated over a small volume, comprising a multitude of such characteristic lines, a smoothness is introduced that is not inherent to the equation itself.

A second drawback is that this method spends a lot of effort in computing the intensity — actually, the closely related variable $u(\mathbf{x}, \mathbf{s})$ — in the domain, while it can be found directly using the formal solution (2.34) once the intensity on the boundary is known.

Finally, it can be complicated to solve arbitrary reflective boundary conditions. Typically, these are solved by iteration which is not guaranteed to converge quickly if the reflectivity is close to unity. This means that the use of purely specular boundaries to reduce the number of elements in presence of symmetry planes might not have the desired complexity reduction.

Algebraic Ray Tracing

In the previous chapter we have encountered several different solution methods. For the optically thick case, the modified diffusion method gave good results, but when the assumption of optical thickness is not valid it failed. Other methods that were presented were either too computationally intensive or failed to treat reflective boundaries properly.

In the first section a new method, the ARTM, is proposed that bears resemblance with the Ray Trace Method. As in ray tracing, the method presented here makes use of the concept of rays. Yet, in spirit it is closer to the methodology that we applied to construct the exact one-dimensional solution. We show that two separable problems can be formulated: one to solve the intensity on the boundary, the other to compute the heat flux divergence given the boundary radiation together with a temperature field.

Section 4.2 gives a theoretical error estimate for the presented method, taking all the different discretisations and numerical integrations into account. Section 4.3 focuses on some implementation details. Finally, in Section 4.4 we present some examples and constructs a numerical error estimate.

4.1 Derivation of the Algebraic Ray Tracing Method

In the discussion of (classical) Ray Tracing we saw, that this method redistributes the spontaneously emitted energy over the domain of interest. The energy could be obtained from knowledge of the temperature field. This meant that every time the temperature changes the whole process of redistribution had to be repeated, which means high costs for every occasion the heat flux divergence is needed.

An approach to overcome this growth in complexity, is to do the ray tracing algebraically, and in the other direction. We will call this approach the *Algebraic Ray Trace Method* or ARTM in short. The method as been presented before in [van der Linden and Mattheij, 1999a, van der Linden and Mattheij, 1999b]. As was shown in Section 3.1, the divergence of the heat flux could be formulated in terms of the blackbody intensity distribution by making use of the formal solution of the RTE without usage of numeric values of $B(\mathbf{x})$. In higher dimensions, too, this formal solution exists as is shown in (2.34). But whereas it was possible

to compute the irradiance analytically in one dimension, this proves to be too difficult for arbitrary domains in higher dimensions.

Therefore, we make use of the DOM of Section 3.3, to limit the number of directions \mathbf{s}_i to a finite set \mathcal{S} . Furthermore, the DOM gives appropriate quadrature weights w_i for every direction \mathbf{s}_i to perform integration over all directions. Space, too, is discretized. For this discretisation we make use of the mesh that exists for solving the heat equation for which the radiative heat flux is computed. So, suppose, the domain of interest Ω is already divided in some grid consisting of a certain number of elements built from a set \mathcal{M} of M nodes with coordinates \mathbf{x}_i , $i = 1, 2, \dots, M$. A subset \mathcal{M}_Γ of \mathcal{M} represents nodes laying on the boundary. In glass process simulations this often will be a Finite Element Method (FEM) or Finite Volume Method (FVM) based grid, as done in [Nefedov, 1999]. For FEM the elements typically are line pieces, triangles or tetrahedra, depending on the dimension of the problem; for FVM rectangles and boxes are more likely elements.

Assuming that the temperature is known, or should be calculated, at the nodes as $T_i := T(\mathbf{x}_i)$, we can define the discrete blackbody intensity as $b_i := B(T_i)$. Since it is unlikely that the characteristic lines of (2.31) go in general through more than one node, we extend the discrete blackbody intensity to the whole domain Ω by

$$\tilde{B}(\mathbf{x}) = \sum_{m=1}^M b_m \varphi_m(\mathbf{x}), \quad (4.1)$$

where $\varphi_m(\mathbf{x})$ are appropriate interpolating functions, such that

$$\tilde{B}(\mathbf{x}_m) = B(\mathbf{x}_m) \text{ for all } m \in \{1, 2, \dots, M\}. \quad (4.2)$$

The intensity has to be discretized twice: a directional discretisation, achieved by making use of the DOM, and a spatial discretisation on the underlying grid. Therefore, we define the discrete intensity as:

$$h_{ij} := I(\mathbf{x}_j, \mathbf{s}_i), \quad (4.3)$$

with $\mathbf{x}_j \in \mathcal{M}$ and $\mathbf{s}_i \in \mathcal{S}$. To solve (2.34), a ray starting at \mathbf{x}_j is followed *back* in direction $-\mathbf{s}_i$ until the boundary of the domain is reached. Quantities particular to such a ray are indicated with the superscript ij . Note, that tracing the ray back follows the approach used in constructing the exact solution for one dimension as used in Section 3.1. On the contrary, in the (classical) ray tracing procedure outlined in Section 3.4.1 the rays were followed in a forward direction, which can only be done if the emitted energy is known at a node. In the present method we do not need a numerical value as yet.

The construction of the discrete version of the formal solution to the RTE in (2.34) consists of two distinct parts: partially extinct radiation from the boundary and an integral containing the contribution from spontaneous radiation in the domain. To construct this formal solution using the information we have on the mesh, we follow the ray back to the boundary, collecting all intersections with element boundaries in the set $\mathcal{X}_{ij} = \{\mathbf{x}_1^{ij}, \mathbf{x}_2^{ij}, \dots, \mathbf{x}_K^{ij}\}$, where K is the number of intersections and \mathbf{x}_m^{ij} are the coordinates of the m -th intersection.

The last intersection in \mathcal{X}_{ij} is equivalent to \mathbf{x}_Γ in (2.34). In general it does not coincide with any of the nodes on the boundary. This means that we have to

interpolate to find the proper boundary intensity:

$$I_v(\mathbf{x}_\Gamma^{ij}, \mathbf{s}_i) \doteq \sum_{m=1}^M v_m^{ij} h_{im}, \quad (4.4)$$

where the interpolation coefficients v_m^{ij} are determined for each ray (i, j) separately. For reasons that will become clear later, it proves wiser to restrict the interpolation to use only those intensities h_{im} with $\mathbf{x}_m \in \mathcal{M}_\Gamma$. If we furthermore define

$$\rho_{ikjm} := \delta_{ik} v_m^{ij} e^{-\kappa \|\mathbf{x}_k^{ij} - \mathbf{x}_j\|}, \quad (4.5)$$

we can write the boundary radiation in a form that fits better with the boundary conditions that are studied later. The Kronecker delta is used to make the coefficient ρ_{ikjm} operate over all directions. Since the rays are assumed to be straight, the ray still refers to exactly the same direction upon arrival at the boundary. The extension of the coefficient is done to make it of the same shape as the coefficients we find for the boundary conditions.

The contribution of the boundary in direction \mathbf{s}_i at node \mathbf{x}_j can then be written as

$$e^{-\kappa \|\mathbf{x}_\Gamma^{ij} - \mathbf{x}_j\|} I_v(\mathbf{x}_\Gamma^{ij}, \mathbf{s}_i) \doteq \sum_{k=1}^N \sum_{m=1}^M \rho_{ikjm} h_{km}. \quad (4.6)$$

Since the coordinates in \mathcal{X}_{ij} are co-linear, a one-dimensional quadrature Q_{ij} can be constructed that approximates the integral in (2.34):

$$(Q_{ij}B)(\mathbf{x}_j, \mathbf{s}_i) := \sum_{k=1}^K u_k^{ij} B(\mathbf{x}_k) \doteq \kappa \int_0^{\|\mathbf{x}_K - \mathbf{x}_j\|} e^{-\kappa \zeta} B(\mathbf{x}_j - \zeta \mathbf{s}_i) d\zeta, \quad (4.7)$$

where u_k^{ij} are the quadrature coefficients, which are given for every ray (i, j) . However, since we do not know $B(x)$ itself, we use its approximation $\tilde{B}(\mathbf{x})$ of (4.2), so we find

$$(Q_{ij}B)(\mathbf{x}_j, \mathbf{s}_i) \doteq (Q_{ij}\tilde{B})(\mathbf{x}_j, \mathbf{s}_i) = \sum_{k=1}^M u_k^{ij} \left\{ \sum_{m=1}^M b_m \varphi_m(\mathbf{x}_k) \right\}. \quad (4.8)$$

If we define

$$a_{ijm} = \sum_{k=1}^M u_k^{ij} \varphi_m(\mathbf{x}_k), \quad (4.9)$$

then (4.8) can be written in the more convenient form

$$(Q_{ij}B)(\mathbf{x}_j, \mathbf{s}_i) \doteq \sum_{m=1}^M a_{ijm} b_m. \quad (4.10)$$

Combining (4.6) and (4.10), we can express the formal solution in discretized form as

$$h_{ij} = \sum_{k=1}^N \sum_{m=1}^M \rho_{ikjm} h_{km} + \sum_{m=1}^M a_{ijm} b_m. \quad (4.11)$$

For intensities at the boundary in the direction of the domain, this equation collapses into the trivial equality $h_{ij} = h_{ij}$. So, to describe these intensities correctly, additional equations are needed.

Such equations are found by using a combination of the boundary equations (2.42) and (2.48). These can be discretized to give

$$h_{ij} = I_{\Gamma, \nu}(\mathbf{x}_j, \mathbf{s}_i) \doteq \epsilon_{ij} r_{ij} + \sum_{\{k | \mathbf{s}_k \cdot \mathbf{n}_j > 0\}} w_k \varphi_\nu(\mathbf{x}_k, \mathbf{s}_k, \mathbf{s}_i) \cos \vartheta_k h_{kj}, \quad (4.12)$$

where w_k are the weights obtained by using the DOM and ϑ_k is the angle between the incoming direction and the local normal. Furthermore, ϵ_{ij} is the emissivity at \mathbf{x}_j in direction \mathbf{s}_i and r_{ij} is the intensity emitted by the boundary; in case of opaque boundaries this is equal to the blackbody intensity of the wall, in case of transparent boundaries it follows from the study of the external radiative field.

From (4.12) we see that it correlates intensities in different directions at the same point. To construct coefficients describing the boundary conditions in a similar form as the coefficients ρ_{ikjm} , we define the following coefficients for the intensity leaving the boundary

$$\rho_{ikjm} = \delta_{jm} w_k \varphi_\nu(\mathbf{x}_k, \mathbf{s}_k, \mathbf{s}_i) \cos \vartheta_k, \quad (4.13)$$

where the Kronecker delta performs a trivial extension of the coefficients to intensities at other points, where the coefficient is simply zero. Then, we can write for the intensity at the boundary

$$h_{ij} = \sum_{k=1}^N \sum_{m=1}^M \rho_{ikjm} h_{km} + \epsilon_{ij} r_{ij}, \quad (4.14)$$

where it is understood that we use this equation only for $\mathbf{x}_j \in \mathcal{M}_\Gamma$ and $i \in \{i | \mathbf{s}_i \cdot \mathbf{n}_j < 0\}$. Note that the form of (4.14) is indeed similar to (4.11).

To operate with equations (4.11) and (4.14), it is easier to write the intensity as a vector, rather than a tensor. Here we choose to do this by placing all columns in the tensor below each other; we place the columns corresponding to points on the boundary before the ones inside the domain. Using the same scheme to reorder the ray trace tensors ρ_{ijkm} into $\mathbf{R} = (r_{ij})$, $\epsilon_{ij} r_{ij}$ into \mathbf{r} , and a_{ijm} into $\mathbf{A} = (a_{ij})$, (4.11) and (4.14) are transformed into

$$\begin{pmatrix} \mathbf{I} - \mathbf{R}_\Gamma & \mathbf{0} \\ -\mathbf{R}_\Omega & \mathbf{I} \end{pmatrix} \begin{pmatrix} \mathbf{h}_\Gamma \\ \mathbf{h}_\Omega \end{pmatrix} = \begin{pmatrix} \mathbf{A}_\Gamma \\ \mathbf{A}_\Omega \end{pmatrix} \mathbf{b} + \begin{pmatrix} \mathbf{r} \\ \mathbf{0} \end{pmatrix}, \quad (4.15)$$

where the indices Γ and Ω means we are referring to points on the boundary or inside the domain respectively. Note, that the coefficients in \mathbf{R}_Ω are completely determined by equation (4.5), while the coefficients in \mathbf{R}_Γ are for half the rows determined by (4.5) and for the other half by (4.13). Although the sizes of the matrices involved are large, they are very sparse; e.g. \mathbf{R}_Ω only has as many non-zeros per row, as the number of points that were used in the interpolation, while the number of non-zeros in \mathbf{R}_Γ does not exceed half the number of directions.

If we solve the intensity vector from this system for given \mathbf{b} and \mathbf{r} , the heat flux divergence $\mathbf{f} = (f_j)$ with $f_j := \nabla \cdot \mathbf{q}(\mathbf{x}_j)$ can be constructed by:

$$\frac{1}{\kappa} \mathbf{f} = 4\pi \mathbf{b} - \mathbf{W} \mathbf{h}, \quad (4.16)$$

where W is a matrix performing a quadrature over all directions for each point. With the definition of \mathbf{w} above, this can be written as

$$W := \begin{pmatrix} \mathbf{w}^T & & & \\ & \mathbf{w}^T & & \\ & & \ddots & \\ & & & \ddots \end{pmatrix}. \quad (4.17)$$

In its form (4.15), the ARTM does exactly what we have said what seems unwise to do: We compute the intensity in every direction in every point only to throw away most of the detailed information upon multiplication with W in (4.16). Yet, the form of the matrix on the left-hand side in (4.15), allows us to compute the equations for the intensities on the boundary \mathbf{h}_Γ separately from those in the domain. So, the intensities on the boundary are computed by

$$(I - R_\Gamma)\mathbf{h}_\Gamma = A_\Gamma\mathbf{b} + \mathbf{r}. \quad (4.18)$$

The matrix $F_\Gamma = I - R_\Gamma$ is a sparse, non-symmetric matrix. From the construction of R_Γ we know that all off-diagonal elements are less than zero and that at least half of the rows have positive sums while the others are positive or zero, unless the geometry is either completely transparent or has zero volume and at the same time has $\rho_d + \rho_s = 1$; so in practise it always has a solution. The benefit of the ARTM over normal ray tracing lies, apart from avoiding duplication of effort, mainly in the formulation of the boundary problem in (4.18). To solve that system we can use an arbitrary solver, while classical ray tracing with its iterative approach is solving it using a Jacobi or Gauss-Seidel iteration, i.e. it approximates the inverse of F_Γ by

$$F_\Gamma^{-1} = I + R_\Gamma + R_\Gamma^2 + R_\Gamma^3 + \dots, \quad (4.19)$$

which might not necessarily converge fast.

After this equation is solved, the intensity throughout the domain can be directly computed by

$$\mathbf{h}_\Omega = R_\Omega\mathbf{h}_\Gamma + A_\Omega\mathbf{b}. \quad (4.20)$$

However, since we are not so much interested in the intensity itself, we can also compute the total incident radiation directly. Let $\mathbf{g} = (g_j)$ be the discretized total incident radiation with $g_j := G(\mathbf{x}_j)$. Since by definition $\mathbf{g} = W\mathbf{h}$, we can compute the incident intensity by

$$\mathbf{g}_\Gamma = W\mathbf{h}_\Gamma, \quad (4.21a)$$

$$\mathbf{g}_\Omega = R_\Omega^*\mathbf{h}_\Gamma + G_\Omega\mathbf{b}. \quad (4.21b)$$

Here, we used the definitions

$$R_\Omega^* := WR_\Omega, \quad (4.22a)$$

$$G_\Omega := WA_\Omega. \quad (4.22b)$$

Using this formulation, we shortcut the computation of the intensity in the domain. The intensity still needs to be computed at the boundary, which is not completely surprising by the way the boundary conditions are formulated.

Note, that now we have a formulation to obtain the intensity at the boundary through (4.18), whereas the modified diffusion approximation of Section 3.2.2 and the FEM formulation of Section 3.4.2 omitted a detailed method to obtain this. These methods must be seen as alternatives to (4.21b) and (4.20) respectively. Equation (4.18) can also be used in combination with these methods. The FEM formulation on the other hand only seems to offer an expensive and approximative solution to (4.20). However, for optically thick geometries the merits of the modified diffusion method could lay in a cheaper evaluation of (4.21b) as G_Ω tends to be a full matrix. The discussion about the costs of the ARTM is made in detail in the next chapter.

This completes the derivation of the ARTM. As we have seen, it is a particular discretisation of the formal solutions based on separate discretisations of the direction space by the DOM and the geometrical space by the method used for the underlying heat problem. The latter makes sure, that the solution obtained by (4.16) can be used in the underlying heat problem.

In the remainder of this chapter we will focus on the accuracy of this method and some simple examples. The next chapter studies the complexity associated with this method and offers some more advanced solution strategies to make the ARTM computationally attractive.

4.2 Accuracy analysis

The ARTM that was presented in the previous chapter performs several numerical approximations in constructing a discretized formulation of the RTE and its solution: a directional discretisation introduced by the DOM, a spatial discretisation of the underlying heat problem which leads to an interpolative formulation of the blackbody intensity, and a quadrature replacing the integral along a ray. To study the errors introduced by the various approximations and their combined effect, we limit ourselves here to a simplified radiative problem.

In order to simplify the following analysis, we study the effects of the ARTM in a completely two-dimensional space, i.e. not only is the geometrical space two-dimensional, but also the direction space is a subspace of \mathbb{R}^2 . The latter means we choose the directions from the unit circle rather than from the unit sphere. Note, that unlike the one-dimensional problem discussed in Section 3.1, this problem is non-physical. Yet, from a mathematical point of view it means just a simplification, not a completely different class of problems.

The geometry under consideration is a disc with radius R with black boundaries. The distribution of the blackbody intensity, a datum, is expressed using polar coordinates as $B(r, \varphi)$. If we furthermore restrict ourselves to prescribing the boundary intensity only in the direction of the centre of the disc, we can easily express the intensity in the centre of the disc as

$$I(0, -\varphi) = e^{-\kappa R} P(\varphi) + \kappa \int_0^R B(r, \varphi) e^{-\kappa r} dr, \quad (4.23)$$

where $P(\varphi)$ is the boundary intensity at (R, φ) in direction $-\varphi$. From the intensity we can compute the total incident radiation, which in two dimensions — in

contrast with (2.18) — is integrated over the unit circle

$$G(0) = \int_0^{2\pi} I(0, \varphi) d\varphi. \quad (4.24)$$

The formulation of the heat flux divergence, too, is slightly different in a two-dimensional space. Adjusting for the different direction space, we find

$$\frac{1}{\kappa} \nabla \cdot \mathbf{q}(0) = 2\pi B(0) - G(0). \quad (4.25)$$

Next, a rectangular mesh is created in the (r, φ) -plane with mesh widths $h_r = R/M$ and $h_\varphi = 2\pi/N$ respectively, where M is the number of intervals in r , and K the number of steps in φ . We do not assume that the number of directions N for use with the DOM is equal to K . Would that be the case, the rays from the origin in the ARTM would coincide with the mesh lines.

Suppose that the temperature, casu quo the blackbody intensity, is known at the nodes of this mesh, such that the discretized blackbody intensity is defined by

$$b_{mk} := B(r_m, \varphi_k). \quad (4.26)$$

The discrete blackbody intensity can be extended to the whole (r, φ) -plane by bilinear interpolation

$$\tilde{B}(r, \varphi) = \alpha_{k+1}(\beta_{m+1} b_{mk} - \beta_m b_{m+1,k}) - \alpha_k(\beta_{m+1} b_{m,k+1} - \beta_m b_{m+1,k+1}), \quad (4.27)$$

with $k = \lfloor \varphi/h_\varphi \rfloor$ and $m = \lfloor r/h_r \rfloor$. Furthermore, the coefficients α_k and β_m are actually functions in φ and r respectively, i.e.

$$\alpha_k := \frac{\varphi - \varphi_k}{h_\varphi} \quad \text{and} \quad \beta_m := \frac{r - r_m}{h_r}. \quad (4.28)$$

Compared to the exact distribution of the blackbody intensity, this approximation has created some defect $E_B(r, \varphi)$, such that

$$B(r, \varphi) = \tilde{B}(r, \varphi) + E_B(r, \varphi). \quad (4.29)$$

For the bilinear interpolation the size of the defect can be estimated as

$$|E_b| \leq \frac{1}{8} M_r h_r^2 + \frac{1}{8} M_\varphi h_\varphi^2 + \frac{1}{64} M_{r\varphi} h_r^2 h_\varphi^2, \quad (4.30)$$

where the coefficients M are defined by

$$M_r := \max_k \sup_r |B_{rr}(r, \varphi_k)|, \quad (4.31a)$$

$$M_\varphi := \max_m \sup_\varphi |B_{\varphi\varphi}(r_m, \varphi)|, \quad (4.31b)$$

$$M_{r\varphi} := \sup_r \sup_\varphi |B_{rr\varphi\varphi}(r, \varphi)|. \quad (4.31c)$$

Interpolation of the boundary radiation gives a similar defect

$$P(\varphi) = \tilde{P}(\varphi) + E_P(\varphi). \quad (4.32)$$

The size of the defect can again be estimated as usual with linear interpolation

$$|E_P| \leq \frac{1}{8} M_P h_\varphi^2, \quad (4.33)$$

with

$$M_P = \sup_{\varphi} |P''(\varphi)|. \quad (4.34)$$

These equations give an insight into the accuracy that we obtain by using linear or bilinear interpolation. In general, the temperature and therewith the blackbody interpolation at the nodes is obtained numerically through the underlying heat problem, so it is not known throughout the domain. This means that interpolation is inevitable when we need to know values in other spots than at the nodes. Consequently, the error introduced by interpolation is inevitable, too. When we look at the accuracy of the integration along the ray, however, we can make use of the fact that the approximated blackbody intensity exists in a particular function space and avoid additional errors.

The formal solution (4.23) for the two-dimensional radiation problem, consists of two parts: a contribution from the boundary and an integral representing the contribution of the domain. If, like before, we split the actual intensity in an approximated intensity and a defect as

$$I(0, -\varphi) = \tilde{I}(0, -\varphi) + E_I(\varphi), \quad (4.35)$$

we can furthermore split the deficit in a part $E_{I,\Gamma}$ caused by the boundary and a part $E_{I,\Omega}$ caused by the domain

$$E_I(\varphi) = E_{I,\Gamma}(\varphi) + E_{I,\Omega}(\varphi). \quad (4.36)$$

The defect caused by the boundary is a simple propagation of the defect caused by the interpolation of $P(\varphi)$, i.e.

$$E_{I,\Gamma}(\varphi) = e^{-\kappa R} E_P(\varphi). \quad (4.37)$$

From this and (4.33), we directly find the estimate

$$|E_{I,\Gamma}| \leq \frac{1}{8} e^{-\kappa R} M_P h_\varphi^2. \quad (4.38)$$

The derivation of an estimate for the defect caused by the domain is slightly more involved. We note that the defect caused by numerical approximation of the integral is dual: we only know the approximated blackbody intensity which has a defect of its own, and there is the defect introduced by making use of a quadrature rather than exact integration. Therefore, we split the domain defect into another two parts

$$E_{I,\Omega}(\varphi) = E_{I,Q}(\varphi) + E_{I,b}(\varphi), \quad (4.39)$$

where $E_{I,Q}(\varphi)$ is the defect due to the use of a quadrature and $E_{I,b}(\varphi)$ is the defect due to use of an inexact approximation of the blackbody intensity. The latter is found by

$$E_{I,b}(\varphi) := \kappa \int_0^R E_b(r, \varphi) e^{-\kappa r} dr, \quad (4.40)$$

the size of which can be readily estimated by making use of (4.30). Thus, we find

$$|E_{I,b}| \leq \frac{1}{8}(1 - e^{-\kappa R}) \left[M_r h_r^2 + M_\varphi h_\varphi^2 + \frac{1}{8} M_{r\varphi} h_r^2 h_\varphi^2 \right]. \quad (4.41)$$

The term $E_{I,Q}$ depends on the type of quadrature. Because of the bilinear interpolation we have chosen and the fact that all rays leaving the origin travel through the domain with constant φ , we know that the approximated blackbody intensity $\tilde{B}(r, \varphi)$ is piecewise linear along such rays. Because of the exponential in the integrand of the formal solution, however, a standard composite trapezoidal rule performs badly here. On first sight it does a good job as the defect can be estimated by

$$|E_{I,Q}(\varphi)| \leq \frac{R}{12} M_{I,Q}(\varphi) h_r^2, \quad (4.42)$$

with

$$M_{I,Q}(\varphi) := \sup_r \left| \kappa e^{-\kappa r} \left\{ \kappa \tilde{B}(r, \varphi) - 2\tilde{B}_r(r, \varphi) \right\} \right|. \quad (4.43)$$

Although (4.42) suggests it performs well, a closer look to (4.43) reveals the problem with the trapezoidal rule here. If the blackbody would be constant throughout the domain and boundary, all the previous defects disappear. Yet, in such a case (4.43) gives $M_{I,Q} = \kappa^2 B$ and therefore an error of

$$|E_{I,Q}(\varphi)| \leq \frac{RB}{12} (\kappa h_r)^2, \quad (4.44)$$

so the error in this case depends rather on the optical step size $\Delta\tau := \kappa h_r$ than on the physical step size h_r itself. For optically thick glass this becomes a problem, as h_r in (4.42) has to be chosen very small. For example the green sample glass of Table 3.1 has $\kappa = 350 \text{ m}^{-1}$, suggesting a step-size $h_r < 10^{-3} \text{ m}$ to keep $\Delta\tau < 1$ and thus the error limited. If we then would like to study a glass furnace of 1 metre deep, 10 metres long and 3 metres wide, we would need something in the order of 30 billion nodes. With the exponential in the integrand all Newton-Cotes type of quadratures suffer from this deterioration for optically thick glasses.

These problems, however, are easily overcome by using a specialised quadrature that integrates integrals of the type

$$y = \kappa \int_a^b f(x) e^{-\kappa x} dx, \quad (4.45)$$

exactly for linear functions $f(x)$. In fact, this is done by the following quadrature

$$\tilde{y} = c_0(a, b)f(a) + c_1(a, b)f(b), \quad (4.46)$$

with

$$c_0(a, b) := \left(1 - \frac{1}{\kappa h}\right) e^{-\kappa a} + \frac{1}{\kappa h} e^{-\kappa b}, \quad (4.47a)$$

$$c_1(a, b) := \frac{1}{\kappa h} e^{-\kappa a} - \left(1 + \frac{1}{\kappa h}\right) e^{-\kappa b}, \quad (4.47b)$$

with $h := b - a$. Chained usage of this quadrature to each linear piece of \tilde{B} along the ray then results in an exact evaluation, i.e. $E_{I,Q} = 0$. So, the small

extra effort in evaluating the quadrature according to (4.46), (4.47a) and (4.47b) is rewarded by the fact that the defect in the computed intensity is caused solely by the interpolation. Using this quadrature we find for the defect in I that

$$|E_I| \leq \frac{1}{8} e^{-\kappa R} M_P h_\varphi^2 + \frac{1}{8} (1 - e^{-\kappa R}) \left[M_r h_r^2 + M_\varphi h_\varphi^2 + \frac{1}{8} M_{r\varphi} h_r^2 h_\varphi^2 \right]. \quad (4.48)$$

The effects of the different types of quadratures are further illustrated by the example computations in Section 4.3.2.

Finally, when the intensity is integrated over all directions an additional defect is created by the quadrature acquired through the DOM. Note that since in (4.25), the origin is part of the mesh, the blackbody intensity is presumed to be known exactly at that spot, making the size of the defect in $\nabla \cdot \mathbf{q}_r(0)$ the same as the defect in $G(0)$.

In two dimensions we can forgo the complex procedure of finding homogeneous sets: such sets can be simply found for any number of directions by dividing the unit circle into equal parts. We can then apply a trapezoidal rule quadrature over all the intensities. Due to the fact that the bilinear interpolation $\tilde{I}(0, \varphi)$ is piecewise linear over φ , we can discern two cases. In case the direction set is chosen to coincide with the φ_k from the mesh the quadrature does not introduce an additional defect. If the directions do not coincide however, the error scales linearly with h_φ .

Assuming we choose the former direction set, the defect in the heat flux divergence can be estimated by

$$|E_{\nabla \cdot \mathbf{q}(0)}| \leq \frac{\pi}{4} e^{-\kappa R} M_P h_\varphi^2 + \frac{\pi}{4} (1 - e^{-\kappa R}) \left[M_r h_r^2 + M_\varphi h_\varphi^2 + \frac{\pi}{4} M_{r\varphi} h_r^2 h_\varphi^2 \right]. \quad (4.49)$$

Although, this is an estimate for the two-dimensional case and in the origin only, a similar analysis could be made for a sphere in three dimensions. This would lead to a similar accuracy estimate. We have shown that for a suitable direction set the accuracy scales quadratically with some identifiable step-size h . To arrive at that result, we made several assumptions. In order to preserve the accuracy obtained for more complex geometries, we need to take care not to violate those assumptions.

The major implication stemming from the accuracy analysis is how the integration along the ray should be performed. We have introduced a quadrature that integrates piecewise linear functions exactly in (4.46). This means we would like to choose the interpolating functions in (4.1) such that we obtain a piecewise linear approximation of the blackbody intensity for every ray in every direction. This puts some constraints on the mesh that we use.

If the underlying heat problem is being solved using finite elements, usually the mesh is built up from simplexes together with appropriate linear test functions. Such a configuration does result in a piecewise linear distribution of the blackbody intensity along the ray, with the transition between the line pieces coinciding with the edges of each simplex. However, for a regular grid, consisting of rectangles or boxes, one would choose bi- or tri-linear interpolation — as was done in the previous section. Using such interpolation only gives linear behaviour within a cell for particular directions. Therefore, in order to get

piecewise linear behaviour for all rays the cells should be divided in simplexes. Although, this means building a separate mesh for performing the algebraic ray tracing, failing to do so would mean non-linear behaviour of the blackbody intensity distribution along a ray, in which case (4.46) has an accuracy of only $\mathbf{O}(h)$ rather than the $\mathbf{O}(h^2)$ we achieved now. Another advantage of using simplexes is that since the abutments of the composite quadratures coincide with the edges or faces of the simplexes, interpolation only occurs at these lower dimensional elements. Clearly, this means that the interpolation can be done at lower costs.

Finally, we note that we have omitted treatment of reflections in this analysis. Since the reflective boundary conditions are formulated in a local manner, their accuracy rests solely on the accuracy of the discrete ordinate method used. At least, this would be the case for cases where a smooth reflection distribution function applies. However, for spectral and Fresnel reflection this distribution contains a Dirac delta function, i.e. one particular direction is singled out. For an arbitrary geometry it is unlikely that also the direction \mathbf{s}^* from (2.58) is in the direction set obtained by the DOM. Two approaches exist to deal with the reflected direction. First, we could interpolate the intensity directionally. This means that the specular reflection is somewhat diffused over neighbouring directions. A second possibility is to clip to the nearest direction. However, both approaches lead to non-specular reflection, reducing the attractiveness of using specular planes in cases of symmetry, if it cannot be guaranteed that both the incoming and outgoing directions are both in the direction set. The symmetry over the octants that both the level symmetric sets and the quasi-homogeneous sets of Section 3.3 portray, implies such a warranty for at least symmetry planes perpendicular to one of the spatial axes.

The main result of the analysis presented here is that the accuracy in principle behaves as $\mathbf{O}(h^2)$, where h is some characteristic mesh size. This accuracy estimate only takes errors into account generated by spatial discretisation. Unfortunately, we were not able to derive a theoretical error estimate for the directional discretisation by the DOM. The error generated by discretisation of the directional space, however, is discussed in some detail below in Sections 4.3.1 and 6.3. Finally, where in this section we concentrated on a theoretical error estimate, we discuss numerical error estimates for some sample problems in Sections 4.4 and 6.3.

4.3 Implementation

Now we have seen the accuracy and complexity estimates, we can have a closer look to the implementation of the ARTM. We start with the one-dimensional case, where the intersections of rays coincide with nodes and therefore are known beforehand. Then, we proceed to the two-dimensional case, which is non-physical but offers good insight in the various steps. Finally, three-dimensional ray tracing is discussed. As we will see, the three-dimensional case does not differ much from the two-dimensional one, so we limit ourselves to the discussion of differences between both implementations there.

4.3.1 One dimension

Algebraic ray tracing in one dimension can be implemented easily. Yet, we have seen before in one dimension the solution is known analytically for simple reflection models. So it only makes sense to do so for more complicated reflection models; e.g. in case of a high specular reflectivity, for which we failed to obtain a solution in closed form. But for the reflection models that were covered, while the algebraic computation of the analytical solution requires a lot of time, accurate results can be obtained numerically by a straightforward discretisation of (3.18). Since the ARTM makes use of the finite number of directions used by the DOM, the accuracy of a one-dimensional implementation is bounded by how well we can approximate the integral (A.1) using only that finite set of directions. After all, the formal solution to the RTE is given by equations (3.3a) and (3.3b), which have a singularity when $\mu \rightarrow 0$, i.e. when the angle ϑ between the radiation direction and the positive x -directions, as shown in Figure 3.1, tends to $\pm \frac{\pi}{2}$. When the direction of the radiation is perpendicular to the x -axis, we know from (3.2), that the intensity is equal to the blackbody intensity at the same location. However, it is clear that for very small values of μ the formulation of the formal solution in one dimension does not make it very accurate numerically.

Because of the small size of the weights following from the directional quadrature (3.12) for those directions, the inaccuracy does not necessarily propagate to the divergence of the heat flux. Staying close to the formulation of the ARTM and its choice for a homogeneous direction set, we construct something that resembles such a set. Having only ϑ left to distribute, we divide the unit circle where the directions can be chosen from into N intervals with nodes at

$$\vartheta_i := i\Delta\vartheta, \quad i = 1, 2, \dots, N; \quad \text{with } \Delta\vartheta = \frac{2\pi}{N}. \quad (4.50)$$

The integral (3.12) can then be discretized by the following quadrature formula

$$(Wf)(x) \doteq \Delta\vartheta \sum_{i=1}^N f(x, \vartheta_i) \sin \vartheta_i. \quad (4.51)$$

Since $\sin \vartheta_i$ approaches zero for directions almost perpendicular to the x -axis, these directions do not contribute much to the final result, and therefore do not need to be very accurate. Of course, we could have chosen a better quadrature than (4.51), but since this is hard or impossible to do in higher dimensions, we choose to stay close to the formulation of the ARTM.

Using the analytical formal solution, we can easily write down the discretized formal solution. We assume that the one-dimensional geometry has a length L , and that the medium inside the domain has an absorption coefficient κ . For the geometry we choose $M + 1$ equidistant nodes, separated by a distance $\Delta x := L/M$. If we follow a ray from a certain node to one of the boundaries, all the intersections of the ray with the boundaries of the elements — here, line pieces — coincide with the nodes. The distance between two consecutive intersections depends on the direction and is $\Delta x / \mu_i$; consequently the optical distance between intersections is $\Delta\tau_i := \kappa \Delta x / \mu_i$ for the i -th direction. Choosing a small number $\delta > 0$ close to zero to avoid the singularity, we use (4.46) to integrate along the

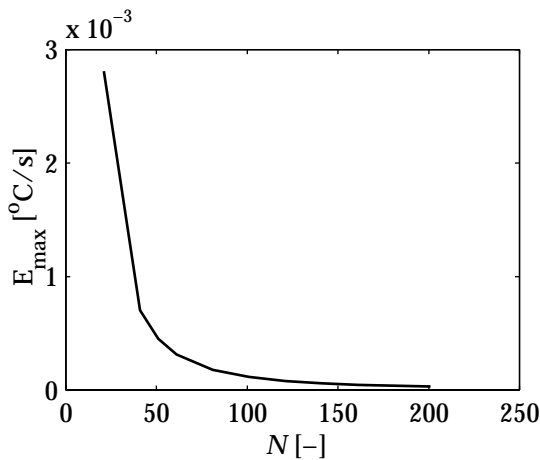


Figure 4.1: Maximum error E_{\max} of the heat flux divergence as function of the number of directions N , for a one-dimensional geometry of 1 cm length with 100 nodes and filled with the green glass of Table 3.1.

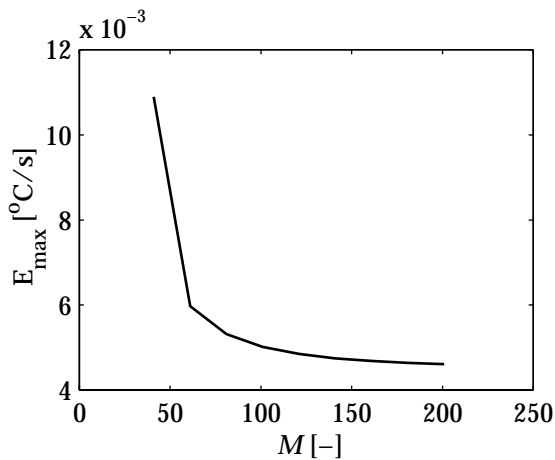


Figure 4.2: Maximum error E_{\max} of the heat flux divergence as function of the number of nodes M , for a one-dimensional geometry of 1 cm length and filled with the green glass of Table 3.1. The direction set consisted of 161 directions. Note that the error does not converge to zero for increasing M .

rays. For all $\mu_i > \delta$, we then find

$$h_{ij} = h_{i0} e^{-j\Delta\tau_i} + \sum_{k=0}^{j-1} \left[c_0(d_k, d_{k+1}) b_{j-k} + c_1(d_k, d_{k+1}) b_{j-k-1} \right]. \quad (4.52)$$

Here we have used $d_k := k\Delta x/\mu_i$ and with the coefficients as defined in (4.47a) and (4.47b). For the directions that are pointing to the left, i.e. $\mu_i < -\delta$, we find

$$h_{ij} = h_{iM} e^{-(M-j)\Delta\tau_i/\mu_i} + \sum_{k=0}^{M-j-1} \left[c_0(d_k, d_{k+1}) b_{j+k} + c_1(d_k, d_{k+1}) b_{j+k+1} \right]. \quad (4.53)$$

Using a trapezoidal rule rather than the improved numerical integration scheme, c_0 and c_1 are chosen as $c_0(a, b) = \frac{1}{2}\kappa(b-a)\exp(-\kappa a)$ and $c_1(a, b) = \frac{1}{2}\kappa(b-a)\exp(-\kappa b)$. For reasons mentioned before, we use the blackbody intensity $h_{ij} = b_j$ for directions close to the singularity, i.e. $|\mu_i| \leq \delta$. These equations suffice to construct the matrices R_Ω , A_Γ , and A_Ω , while they account for half the rows in R_Γ , namely those referring to radiation falling onto the boundary. The other half of that matrix is constructed from the reflection equations. Using a diffuse/specular reflection model, we find at the left boundary that for $\mu_i > 0$

$$h_{i0} = \epsilon_0 B_0 + \rho_{s,0} h_{\xi 0} + 2\rho_{d,0} \Delta\vartheta \sum_{\mu_k < 0} |\cos \vartheta_k| \sin \vartheta_k h_{k0}, \quad (4.54)$$

with the specular reflected direction index ξ chosen such that $\vartheta_\xi = \pi - \vartheta_i$. B_0 represents the blackbody intensity of the left wall. As we have noted before, this does not need to be the same as the blackbody intensity of the medium at the wall, although usually we have $B_0 = b_0$, when conduction is present. Similarly, we find for the right wall when $\mu_i < 0$

$$h_{iM} = \epsilon_1 B_1 + \rho_{s,1} h_{\xi M} + 2\rho_{d,1} \Delta\vartheta \sum_{\mu_k > 0} \mu_k \sqrt{1 - \mu_k^2} h_{kM}. \quad (4.55)$$

Here we have used the alternative formulation of the diffuse reflections in terms of μ rather than ϑ . For the right boundary ξ satisfies $\mu_\xi = -\mu_i$. B_1 is the blackbody intensity of the right boundary. Only when conduction is present, we might assume that $B_1 = b_M$. These equations are all that are needed to complete the formulation of the ARTM in one dimension. For a given vector \mathbf{b} containing the blackbody intensities, we can now apply equations (4.16)–(4.22b) to find the heat flux divergence.

For an example computation we have studied the same geometries as discussed in Section 3.1, i.e. a 1 cm and a 100 cm slab geometry filled with the green sample glass of Table 3.1. On this geometry a parabolic temperature profile was imposed with $T = 1000^\circ\text{C}$ at the boundaries and $T = 1020^\circ\text{C}$ in the middle. The resulting distribution of the radiative heat flux for the different reflectivities are so close to the analytical solution that we refrain from showing them here again, but refer to the graphs in Figures 3.2 and 3.5 which represent the solution obtained through the ARTM, too. Only when the trapezoidal rule is used for integration along a ray, for the optically thick case, we find huge errors of the same order or larger than the solution itself. This had already been predicted by (4.42) and (4.43).

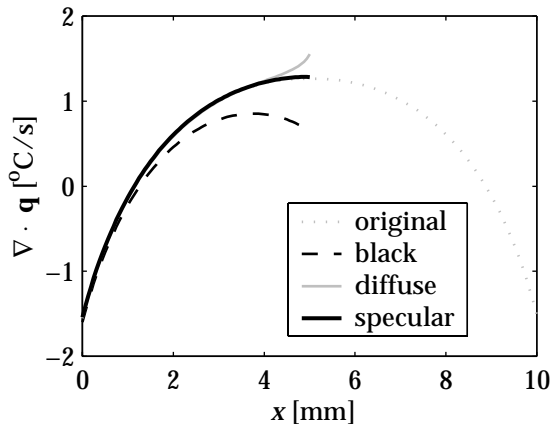


Figure 4.3: Comparison of the radiative cooling of a problem with symmetric temperature profile in a 10 mm slab (dotted curve) with a problem on a geometry half the size where the symmetry plane has been replaced by 100% specularly reflective wall (solid curve). For further comparison the radiative cooling for the cases that the symmetry plane were replaced by a black (dashed curve) or 100% diffusely reflective wall (gray curve) are also shown.

More interesting for the study of the accuracy is how the error changes with increasing N and M . In Figure 4.1, we have plotted the maximum error in the heat flux, when the number of directions N is increasing, keeping the number of nodes M fixed. The maximum error is defined here as

$$\epsilon_{\max} := \max_x \frac{1}{c_v \rho} \left| \nabla \cdot \mathbf{q}_{\text{ARTM}} - \nabla \cdot \mathbf{q}_{\text{exact}} \right|. \quad (4.56)$$

The result of the first figure is not very surprising, the error keeps decaying with increasing number of directions. However, if we keep the number of directions fixed and look at the behaviour of the maximum error with increasing M , we see the distribution as is displayed in Figure 4.2. After M has reached a certain limit, the maximum error does not decrease significantly. Unfortunately, since we are dealing with such a special case with a singularity near $\vartheta = \pm \frac{1}{2}\pi$, we cannot extrapolate this result to higher dimensions and conclude that the accuracy stops decreasing for an increased number of nodes, if the number of directions is not increased at the same time. Clearly, for one dimension this *is* the case.

We end the study of the one-dimensional ARTM, by verifying the assumption that for computation of radiative heat transfer, symmetry planes within the domain can be replaced by purely specular boundaries. For that purpose we cut the one centimetre slab of the previous problem in half, while imposing the same parabolic profile as before, i.e. $T = 1000^\circ\text{C}$ at the left boundary and $T = 1020^\circ\text{C}$ on the right, which corresponds to the centre of the original domain. In Figure 4.3, we have drawn the resulting divergence of the heat flux for various boundary conditions on the right. The three different curves represent a purely black boundary, a purely diffusely reflecting boundary and a purely specular boundary.

We see that the left half of the dotted curve, showing the solution of the original problem, indeed corresponds to the solution on the new domain with a purely

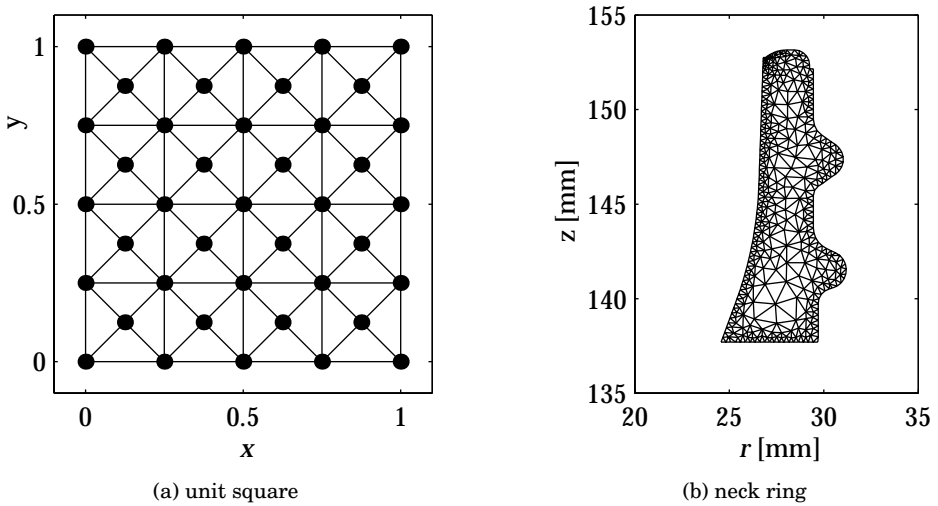


Figure 4.4: Two example meshes used for two-dimensional ray tracing: (a) a dimensionless unit square with 41 nodes, of which 16 are on the boundary; and (b) a neck ring geometry with 449 nodes of which 166 are on the boundary.

specular boundary. Assuming a black boundary would underestimate the heat flux, while assuming a diffuse boundary overestimates the radiative cooling. This clearly signals that only specular boundaries can act as a symmetry plane. It is interesting to note that in the production of glass plates for LCD screens, the furnace in which the glass is molten and the feeder in which the glass melt is transported is coated with platinum, which is very highly specular. The glass needs to be of very uniform quality. As we can see here, utilisation of specular boundaries acts as enlarging the geometry and thereby enhancing the (thermal) homogeneity. This cannot be achieved by lowly reflective walls, as shown by the black boundary, or non-specular reflective walls as shown by the diffuse case. Note that the error introduced by the assumption of a black boundary affects the whole domain, while the effect of a diffusely reflecting boundary is only limited to a small region near that boundary. This can be expected as the radiation leaving the black boundary does not take radiation close to the boundary into account, while the two purely reflective boundaries do.

4.3.2 Two dimensions

Whereas in one dimension we know the intersections of any ray with the interfaces between geometry elements beforehand, in two and higher dimensions they are generally unknown and have to be computed for any given mesh. In this section we explain how ray tracing is performed in practise and which pitfalls should be avoided. To that end we concentrate on two different meshes introduced in Figure 4.4. The first mesh is a simple triangularisation of a unit square. We have omitted the physical dimensions, but can scale the mesh to any size. The second mesh has a practical background. It is a so-called *neck ring*, which is the top part of a bottle; this mesh arises in simulations done to analyse the pressing phase in [Laevsky, 2002]. Unlike the unit square this geometry is

non-convex and with its thickness of about 5 mm it is optically non-thick for the green and brown glasses this shape is typically associated with, whereas it is optically thin for white glasses.

Here we concentrate on triangulated meshes; using a simplex as the building block means we can do true linear interpolation within those blocks. If a rectangular grid is used, we would have to perform bilinear interpolation within the building block. This would mean that the blackbody intensity would not vary linearly along a ray for any arbitrary direction. This, in turn, would mean the term $E_{I,Q}$ would not disappear in (4.39), which imposes additional constraints on the smoothness of $B(\mathbf{x})$. To avoid these problems and the need for a higher order integration scheme, we assume that a regular grid has been transformed in a triangularisation before the ARTM is performed.

A triangulated grid is commonly stored as a list of nodes, edges and triangles. The nodes are typically stored as a coordinate pair. The edges are usually stored as a pair of indices or other references to the nodes they connect, whereas the triangles are stored as triplets of references to either the nodes or the edges, that define them. Furthermore, all these geometrical elements can have a label of some sort as an attribute.

This representation of a triangulated mesh may come directly from a mesh generator, or be passed on from the underlying heat problem. For an efficient use in the ARTM, however, such a simple representation has to be augmented with some additional data structures. Since most of the work during the tracing is done finding intersections between rays and edges of triangles this has to be done as efficiently as possible. This not only requires construction of computationally geometrical line-pieces of the edges, so they do not have to be remade for every intersection test, but also the number of intersection tests should be reduced to a minimum. In the simple representation we would need to go through all the edges and test for an intersection for every ray.

To improve on this situation, we choose to give the edges two additional attributes. The data structure of the edges contains references to the two triangles the are part of. Of course, boundary edges are only part of a single triangle, which offers us a simple manner of knowing whether an edge is a boundary edge. Furthermore, we construct a data structure, such that we can obtain the triangles a specific node belongs to in constant time. With this information we can perform the tracing as follows:

- Every ray starts from a node \mathbf{x}_j of the mesh. To find the intensity in direction \mathbf{s}_i , we follow a ray back to the boundary in the opposite direction, i.e. $-\mathbf{s}_i$. This means the parametric description of the ray is

$$\text{ray}[i, j] : \mathbf{x} = \mathbf{x}_j - \lambda \mathbf{s}_i, \quad \lambda \geq 0. \quad (4.57)$$

- If the node is on the boundary we test whether the inner product of the negative direction and the outward pointing normal is non-negative. If this is the case, we have to use the reflection equations to construct the $(N * j + i)$ -th row of R . In all other cases, we use the ray trace procedure to fill the $(N * j + i)$ -th row of R and the $(N * j + i)$ -th row of A .

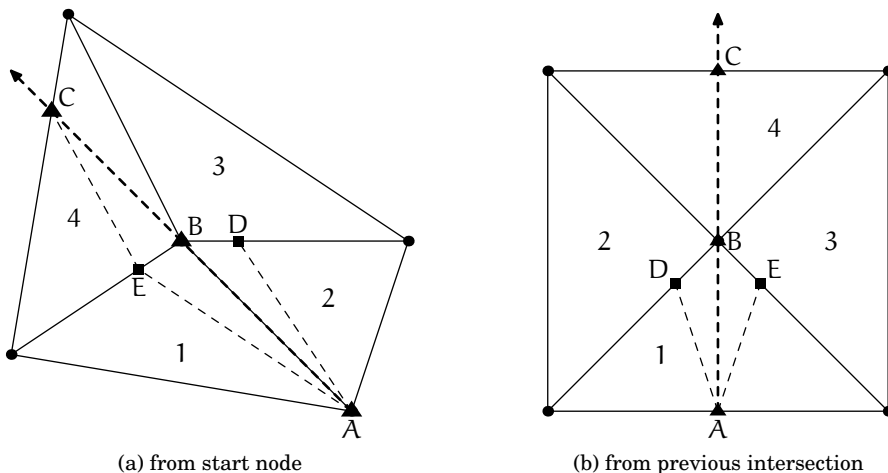


Figure 4.5: Errors in the ray trace procedure. In both figures, analytically the ray would run from A through B to C. Due to rounding errors, however intersection D or E might be found instead. The distances between B, D and E have been greatly exaggerated. In practise they would almost coincide. After proceeding to the next element, the ray trace procedure will fail to find a new intersection point. Only after intersection E is found in figure (a), by chance, the ray trace procedure continues correctly.

- From the special data structure we have constructed, we then obtain a list of all triangles the node belongs to. The first intersection of the ray then is the node itself, i.e. it is the point on the ray with $\lambda_0 = 0$. The second intersection point will be on one of the edges *without* the node of one of the triangles *containing* the node. For the intersection a new λ will be found, such that $\lambda_1 > \lambda_0$. Finding the intersection also reveals the edge that was intersected. A reference to this edge is stored along with λ_1 . Furthermore, this edge knows which triangles it is part of. So, the search for the next intersection can be limited to the two other edges of the next triangle.
- We repeat this until we find an intersection with a boundary edge. For the k -th intersection we obtain a λ_k such that $\lambda_k > \lambda_{k-1}$ and a reference to the edge that this intersection is relative to. We see that after the startup, we ideally never have to test for more than two intersections with edges.

Computers work far from ideally. More specifically, the inherent inaccuracy associated with floating point calculations, means some interesting exceptions can occur when finding the intersection. In two dimensions this is the case when the intersection is very close to another node. This is illustrated in Figure 4.5. The first part of this figure shows a breakdown of the outlined ray trace procedure when a ray is aligned with an edge. Starting from node A the next intersection that should be found is B. However, due to the limitation in the accuracy of floating point operations it is very likely, that the actual intersection found is D or E. In practise D and E are very close to B; the distances in the figure have been exaggerated for clarity. If we would accept D as a valid intersection, the ray trace procedure would proceed from triangle 2 to triangle 3. However, in triangle 3 no intersection would be found such that $\lambda_k > \lambda_{k-1}$. The second part of the figure

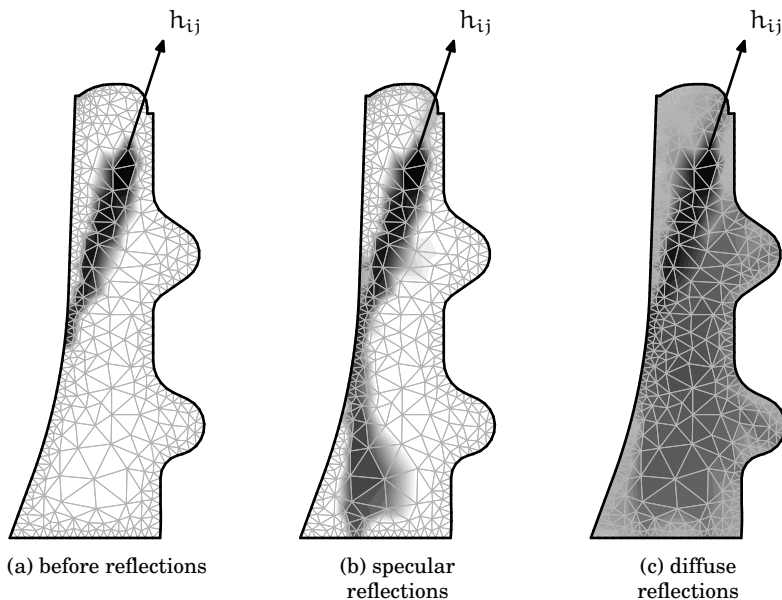


Figure 4.6: Visualisation of a ray through the rows of A . Colours are used according to a logarithmic scale: black is 10^{-2} or higher, white is 10^{-10} or lower. Please consult the text for further explanation.

shows, that the same breakdown can occur, even if the ray is not aligned to one of the edges.

The solution is to check whether an intersection is very close to some node. If it is, we start a new trace procedure from the nearest node, i.e. we check all the triangles that contain that node until a $\lambda_k > \lambda_{k-1}$ is found. Since we are always aware which triangle is being processed, only two nodes need to be compared per triangle. Whether it is more appropriate to do this as soon as an intersection is found, or to do this only if the ray fails to proceed, depends on the geometry. For example, this breakdown is very likely to occur repeatedly for the square mesh of Figure 4.4, while for the neck ring mesh, it would occur only exceptionally. So, the first geometry would benefit for an *a priori* test, while the second geometry would be faster with an *a posteriori* check.

After a ray has been traced we have found a list of intersections, stored as $(\lambda_0, \lambda_1, \dots, \lambda_K)$ and references to edges for example stored as (e_0, e_1, \dots, e_K) . The λ 's allow us to construct the appropriate quadrature weights. From the edges and the actual coordinates of the intersections we can furthermore construct the interpolation coefficients. This yields all the information that is needed to construct the matrix A , as outlined in (4.7)–(4.11).

In Figure 4.6 we have visualised the results of the ray tracing. The figure consists of three different sub-figures, which represent a particular ray for different cases. In (a) the entries of some row of A are plotted on the mesh. Recall that the matrix A has M columns, and that the entry at column k corresponds to the fraction of thermal radiative energy emitted at point \mathbf{x}_k contributing to the intensity the specific row refers to. By plotting the entries of one of the rows of A we see the

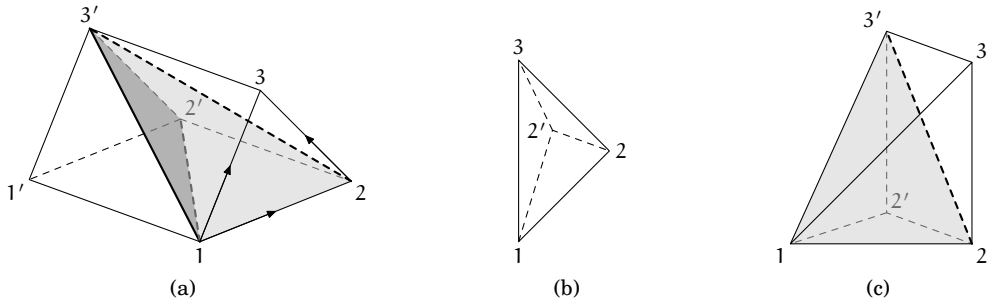


Figure 4.7: Transformation of a triangle to a set of tetrahedra. (a) For triangles with all nodes off the axis of rotation, a prism is constructed and decomposed into three tetrahedra. The decomposition uses the ordering of the nodes indicated by the arrows. (b) If a complete edge is on the axis of rotation only one tetrahedron is created. (c) If one of the nodes is on the axis of rotation, we find two tetrahedra.

ray leaving a point in a certain direction until it has reached the boundary.

The other two sub-figures refer to the same row of the matrix $(I - R)^{-1}A$, i.e. after reflections have been resolved. This shows us how the ray propagates after reflections, just as if we would have continued after reaching the boundary. In (b) we have set out the result for the case that all boundaries are purely specular reflective. In (c) the same is displayed for diffuse reflection. Clearly, since diffuse reflection relates more directions, the influence comes from a much larger part of the domain.

Finally, here too we want to remark that the trapezoidal rule for integration along a ray, shows the behaviour that was predicted in Section 4.2: if the problem becomes optically thick the error becomes enormous. We illustrate this with a numeric example. Suppose the neck ring is made up of an optically very dense glass with $\kappa = 3500 \text{ m}^{-1}$. We further assume a constant temperature all over the domain. The boundaries are assumed to be black and at the same temperature as the glass. In that case, whereas the integration scheme proposed in (4.45)–(4.47b), has a maximum error of less than 10^{-13} times the blackbody intensity in the computation of $\nabla \cdot \mathbf{q}$, the trapezoidal rule exhibits errors as high as 8 times the blackbody intensity. This illustrates that the proposed quadrature is essential for a proper working of the ray tracing.

4.3.3 Three dimensions and axisymmetric geometries

The ARTM procedure in three dimensions does not deviate much from what was outlined in two dimensions. Again, we prefer simplex building blocks to construct the geometry, as they allow for truly linear interpolation. In three dimensions, this means we use tetrahedra where we used triangles in two dimensions. If a regular mesh is used, where the building blocks usually are boxes, we have to split each box in tetrahedra. This means an increase in the number of building blocks, as it takes five tetrahedra to describe a box. The memory requirements for storing the mesh are usually not the limiting factor. Since no new nodes are introduced, the sizes of the various matrices do not increase.

Another source of three-dimensional meshes stems from axisymmetric geome-

tries, which appear often in glass production. While the underlying heat problem is likely to be solved on a two-dimensional mesh, we need a three-dimensional mesh to perform the ray tracing. This means we have to construct a tetrahedral mesh from a triangulated one. We do this by rotating the triangular mesh N_φ times around the axis of rotation. Between every triangle and its copy in the next slice, we construct a number of tetrahedra as is outlined in Figure 4.7. Note that the side planes of the prism in Figure 4.7(a,c) are shared between tetrahedra created from adjacent triangles. This means that we have to use the same line to cut the side of the prism.

To make sure that the same line is used, we attribute a direction for every edge in the triangulated mesh, as indicated by the arrows in the figure. These directions have to be chosen such that they do not form a circular graph. This is easily achieved if the nodes can be put into a strict lexical order and let the direction point from the node lower in the hierarchy to the point further up the hierarchy. That this causes the directions to fulfil the said requirement, is clear if we notice that while for a certain i , j and k the strict lexical ordering asserts that

$$f(\mathbf{x}_i) < f(\mathbf{x}_j) < f(\mathbf{x}_k), \quad (4.58)$$

a circular graph would instead state that

$$f(\mathbf{x}_i) < f(\mathbf{x}_j) < f(\mathbf{x}_k) < f(\mathbf{x}_i) < \dots, \quad (4.59)$$

which is obviously false as it contradicts our strict lexical ordering. So, using such a direction for the edges we ensure that all the tetrahedra we make from a triangle are compatible with the tetrahedra made by the neighbouring triangles. It is very easy to find such strict lexical ordering; e.g. if the nodes are stored in an array, the indices of the nodes form such ordering.

While the tracing has to be done in three dimensions and the complexity of the geometry is greatly increased, this does not have an impact on the memory or time complexity. This is due to the fact that the newly introduced nodes and the physical properties at that position are exact copies of the original nodes. Since we only need to know the intensity at the original nodes, the matrices keep the same size. Only the ray trace procedure itself takes longer, because computation of intersections in three-dimensional space requires some extra floating point operations and because the average length of the traces is a bit longer.

The remainder of the ray trace procedure is quite like the two-dimensional variant. Instead of edges we now have faces, which have planes rather than linepieces associated with them. Like the two-dimensional case, we store a reference the two tetrahedra a particular face is part of together with that face. This allows us as before to easily hop from element to element when following the ray. This hopping is faced with the same complications as in two dimensions: if the ray find an intersection close to a node it might end up looking for an intersection in the wrong tetrahedron. More so, in three dimensions this same breakdown can happen if the intersection is on an edges or in a very near neighbourhood of an edge between two vertices. In that case, we cannot simply restart to trace from the nearest nodes, but limit the search to the intersection of the two sets of tetrahedra associated with each node. Since these sets are small, and such breakdown occurs rarely, it is not necessary to construct a set of tetrahedra for each edge beforehand.

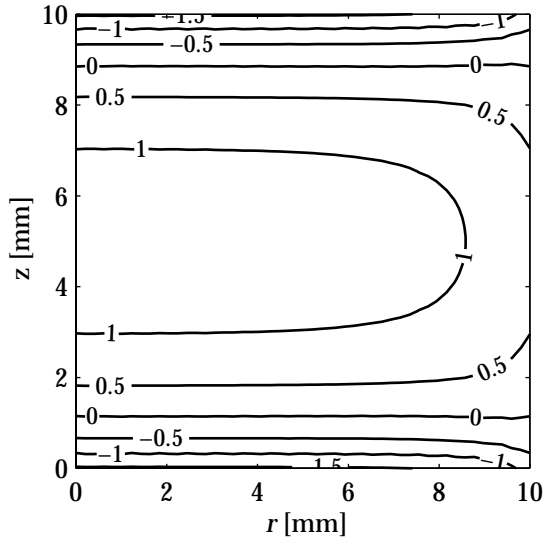


Figure 4.8: Contour lines of the normalised heat flux $\nabla \cdot \mathbf{q}/c_v \rho$ in $^{\circ}\text{C}/\text{s}$ for a cylinder of 1 cm height and 2 cm diameter filled with green glass in a parabolic temperature field.

In the next section, a few example heat flux computations show the results of applying the ARTM and we use a comparison with a one-dimensional geometry as a numeric error estimate. Real applications of the ARTM are discussed in Chapter 6.

4.4 Examples

In this section we illustrate the ARTM by some examples. Here, we limit ourselves to the computation of the divergence of the radiative heat flux. Only later, in Chapter 6, we show how to use this divergence in actual heat computations.

4.4.1 Square mesh

The first example deals with the unit square mesh similar to that of Figure 4.4, but with 145 nodes rather than the 41 shown in the figure. This mesh is used in an axisymmetric setting, which means that the mesh corresponds to a glass cylinder with a diameter that is twice the height. For our example we use a scaled version of that particular mesh such that both the radius and height of the cylinder are 1 cm. For the semi-transparent medium that fills this cylinder we choose the green sample glass of Table 3.1. To find the divergence of the heat flux, the ARTM requires the temperature everywhere in the domain. After the temperature has been transformed into the blackbody intensity and the radiative boundary equations are prescribed, first the boundary intensities and then the divergence of the heat flux can be computed for all nodes.

In the first example, the temperature field is assumed to be parabolic in vertical direction with a temperature of a 1000°C on the top and bottom of the cylinder and 1020°C at 5 mm height. If all boundaries are assumed to be black, we find

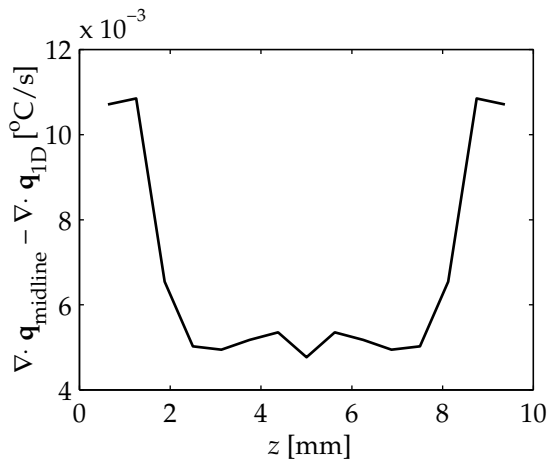


Figure 4.9: Difference between the normalised heat flux on the axis of rotation of the cylinder geometry and the exact solution of the one-dimensional problem with the same temperature distribution.

the divergence as shown in Figure 4.8. The divergence of the heat flux can be thought of as a cooling rate: in absence of other modes of heat transfer this is the speed at which the glass would cool. So, in the figure we see a cooling down in the centre of the cylinder, where the glass is hottest, while near the top and bottom, where the glass is cooler, it is heating up. This is not unlike conduction, although for this parabolic temperature profile the conductive cooling rate would be constant over the domain.

Although the black boundaries that we assume so far, do not model real boundaries, they enable us to find a good numerical error estimate. As the temperature profile does not depend on the r -coordinate, the black boundaries are a model the radiation coming from the remainder of the cylinder if the radius were to stretch to infinity. The latter case we already encountered in the treatment of

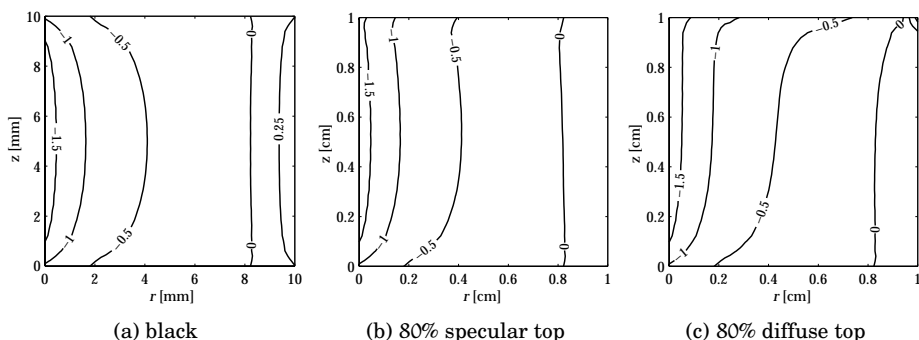


Figure 4.10: Influence of reflectivity. The contour lines show the level of radiative cooling, i.e. $\nabla \cdot \mathbf{q}_r / c_v \rho$, for different reflection models for the top of the cylinder. The levels are given in degrees Celsius per second.

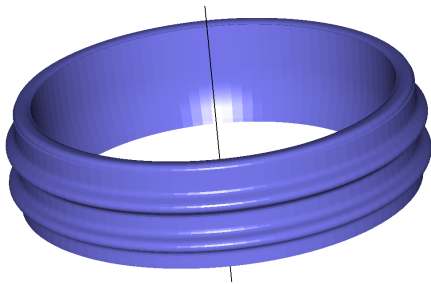


Figure 4.11: Three-dimensional representation of the neck ring first introduced by Figure 4.4.

the one-dimensional problem. So, for this specific case we have an alternative approximation for the solution on the centreline in the form of the exact solution to the one-dimensional problem discussed earlier. In Figure 4.9, we compare the ARTM solution on the centreline by an the exact solution of the corresponding one-dimensional problem. The figure shows the maximum difference between the two models occurs near the boundary and is approximately one hundredth of a degree per second. This means the heat flux divergence computed by the ARTM has an error of less than 1%, given the $1.5^{\circ}\text{C}/\text{s}$ cooling rate at the top and bottom taken from Figure 4.8. Given the fact that for this geometry only 9 nodes were actually placed on the centreline, whereas the exact solution would typically be computed with hundreds of nodes on that line, this result is quite accurate.

To show the effects of reflections, Figure 4.10 shows the computed radiative heat flux for different radiative models for the top of the cylinder. To emphasise the difference we imposed a temperature field linear in the radius r , with the temperature being 1000°C on the centreline and 1020°C on the sleeve of the cylinder. The contour lines, which represent levels in the radiative cooling $\nabla \cdot \mathbf{q}_r / c_v \rho$ and are expressed in $^{\circ}\text{C}/\text{s}$, take a quite different path in the top half of the cylinder. Their effect is almost completely attenuated in the bottom half. While the shape of the contour lines differ, the order of magnitude of the radiative cooling is not affected. In absence of information of other modes of heat transfer it is hard to tell how the difference in radiative cooling rate prevail in actual heat computations. A more thorough discussion of these effects, is therefore postponed to Section 6.4.

4.4.2 Neck ring

We end this chapter with a heat flux computation for the neck ring geometry that we introduced before in Figure 4.4. Again this is an axisymmetric problem, where the heat flux divergence can be processed in two dimensions, while the ray tracing itself takes place in three dimensions. In its three-dimensional form displayed in Figure 4.11, it is easier identifiable as the top of a bottle. For this example computation we impose a temperature gradient that is linear in r -direction and does not vary over the z -coordinate. The temperature field is chosen such that the temperature at the leftmost point is 1000°C , while the rightmost point has a temperature of 1020°C . The boundaries are assumed to have a 20% reflectivity. The results of this problem are shown in Figure 4.12. As expected, we see a slight radiative warming of the left side of the mesh, while the right-hand side

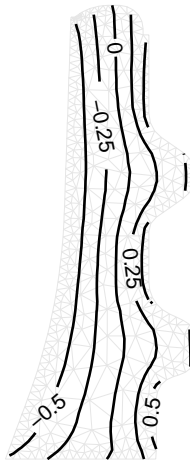


Figure 4.12: Radiative cooling rate on neck ring 20% specular reflectivity. The contours show different levels in $\nabla \cdot \mathbf{q}_r / c_v \rho$ expressed in $^{\circ}\text{C}/\text{s}$.

is cooling down. The divergence of the radiative heat flux is better illustrated in combination with conductive heat transfer. Therefore, we refer to Section 6.3 where we discuss the cooling of the neck ring in a practical section.

In this section, we have show some sample computation of the radiative heat flux divergence. For a cylindrical geometry we were able to find a numerical estimate. With neck ring example we showed, the ARTM has no problem dealing with non-convex problems. The numerical results of these example are by themselves not useful. Rather they need to be studied in the context of an actual heat problem, to study the effects of radiative heat transfer. A detailed discussion of these effects is given in Chapter 6.2, where we treat a few different heat problems and study radiative heat transfer in combination with conduction. Before that, however, we continue the theoretical discussion of the ARTM when we focus on complexity issues in the next chapter.

Reducing complexity

5.1 Complexity analysis

The Algebraic Ray Trace Method introduced in the previous chapter, has shown to be an accurate solution method for radiative heat problems that are not optically thick. This accuracy, however, does not come for free: every time the divergence of the heat flux needs to be computed, a system of equations has to be solved to work out the effects of reflections. In this section these costs are approximated asymptotically. We start by stating the algorithm used to solve the equations of the ARTM, and identify the dominant matrices responsible for memory requirements.

The algorithm used to solve (4.15) and (4.16), consists of a preparatory part, that needs to be performed once only in an unchanging geometry and a part that needs to be repeated for every computation of \mathbf{f} , the discrete form of $\nabla \cdot \mathbf{q}$. In the preparatory stage all matrices necessary to compute the radiative cooling are constructed. In this stage the main memory consumption of the ARTM can be estimated. The second part of the algorithm uses the already constructed matrices to compute the radiative heat flux. In typical applications this step can be made a multitude of times, so it is this part from which the time complexity follows. The two different parts are studied in more detail in the following two subsections.

5.1.1 Memory consumption

As discussed above, the preparation of the matrices needs to be done only once, as long as the geometry does not change. Although this preparatory stage might require considerable time, the fact that it has to be done only once, makes this part mostly interesting for memory consumption estimates. Therefore, we first take a closer look at this part of the ARTM. The preparatory stage of the algorithm consist of the following steps:

1. Obtain a mesh for the geometry. Let us denote the total number of nodes in the mesh, both in the domain and on the boundary, by M and the number of nodes on the boundary by M_Γ ;

2. Obtain a direction set of size N and a corresponding quadrature \mathcal{W} , in its vectorised form \mathbf{w} ;
3. Perform the actual ray tracing using the N directions for all M nodes. This step will yield the matrices R_Γ , R_Ω , A_Γ , and A_Ω — defined in (4.15) — together with the vector \mathbf{r} from that same equation;
4. Memorise reflection and ray trace matrices. Since the system (4.15) can be decoupled into a system for the boundary and one for the domain, and we do not need to know the intensity explicitly throughout the domain, it suffices to compute only the intensity at the boundary. The matrix

$$F_\Gamma := I - R_\Gamma, \quad (5.1)$$

is therefore memorised together with A_Γ and \mathbf{r} . In order to benefit from the sparsity of F_Γ , the system of equations involving this matrix is usually solved using an iterative method. In such a case the preconditioners might be constructed at this point, too;

5. Pre-apply the directional quadrature to the domain matrices. Rather than storing R_Ω and A_Ω , we store

$$R_\Omega^* := W_\Omega R_\Omega, \quad (5.2)$$

$$G_\Omega := W_\Omega A_\Omega, \quad (5.3)$$

where W was defined in (4.17). These can of course better be computed in a matrix-free manner.

The matrices obtained in this preparation are F_Γ , A_Γ , R_Ω^* , G_Ω and optionally the preconditioners for F_Γ . These describe the whole system that we need to compute $\nabla \cdot \mathbf{q}$ for a given temperature distribution, and consequently these matrices are preferably kept in memory. The size of each of these matrices can be estimated a priori by studying the way they are constructed.

First, F_Γ has the same size as R_Γ , i.e. $(NM_\Gamma) \times (NM_\Gamma)$, and — except for the diagonal — the same sparsity pattern. Denoting the number of non-zeroes of a matrix by γ , this means

$$\gamma_{F_\Gamma} \leq \gamma_{R_\Gamma} + NM_\Gamma. \quad (5.4)$$

As was discussed in Section 4.1, the entries in R_Γ are computed in two different ways. In one a row refers to radiation leaving, while in the other it refers to radiation arriving at the boundary. For the radiation arriving at the boundary equation (4.11) is used. For linear interpolation of the intensity between two nodes this means there are two entries per row in R_Γ .

For the radiation leaving the boundary, the number of entries depends on the reflection model used. For black boundaries, the corresponding row in R_Γ is empty, so the row in F_Γ has a single entry. Since for homogeneously distributed direction sets, half of the directions at the boundary are arriving and half are leaving, we find

$$\gamma_{R_\Gamma, \text{black}} = NM_\Gamma \quad \text{and} \quad \gamma_{F_\Gamma, \text{black}} = 2NM_\Gamma. \quad (5.5)$$

Matrix	Size	γ	σ
A_Γ	$(N \cdot M_\Gamma) \times M$	$4N(M - M_\Gamma)$	$4/M_\Gamma$
$F_{\Gamma,\text{diffuse}}$	$(N \cdot M_\Gamma) \times (N \cdot M_\Gamma)$	$\frac{1}{4}N(N + 8)M_\Gamma$	$\frac{1}{4}(1 + \frac{8}{N})/M_\Gamma$
$F_{\Gamma,\text{specular}}$	$(N \cdot M_\Gamma) \times (N \cdot M_\Gamma)$	$\frac{5}{2}NM_\Gamma$	$3/(NM_\Gamma)$
$F_{\Gamma,\text{black}}$	$(N \cdot M_\Gamma) \times (N \cdot M_\Gamma)$	$2NM_\Gamma$	$2/(NM_\Gamma)$
R_Ω^*	$(M - M_\Gamma) \times (N \cdot M_\Gamma)$	$\leq 2NM$	$< 2/M_\Gamma$
G_Ω	$(M - M_\Gamma) \times M$	M^2	1

Table 5.1: Memory consumption estimates for the matrices involved in the ARTM using N directions and M nodes. The number of nodes on the boundary (M_Γ) is 2 for a one-dimensional geometry and can be estimated as $c\sqrt{M}$ for 2D geometries, where c is a constant dependent on the shape.

For diffuse reflection, all incoming directions affect the outgoing radiation, which corresponds to $N/2$ entries per row. In such a situation we find

$$\gamma_{R_\Gamma,\text{diffuse}} = \frac{1}{2}NM_\Gamma\left(2 + \frac{N}{2}\right), \quad (5.6)$$

and

$$\gamma_{F_\Gamma,\text{diffuse}} = \frac{1}{4}N(N + 8)M_\Gamma. \quad (5.7)$$

Finally, the model of specular reflection is a bit simpler, correlating two directions in theory. As was remarked in the previous chapter, however, the reflected direction is generally not in the discrete direction set, in which case interpolation has to be performed using, say, n nodes. For the two-dimensional case — discussed in Section 4.2 — $n = 2$, while for the three-dimensional and axisymmetric cases $n = 3$. If clipping is used, rather than interpolation, we find $n = 1$. Since it represents the worst case, here we assume that $n = 3$. The numbers of non-zeros in F_Γ is

$$\gamma_{F_\Gamma,\text{specular}} = \frac{5}{2}NM_\Gamma, \quad (5.8)$$

which is comparable to the non-zero count for black boundaries. Note, that Fresnel reflections are very similar to specular reflections, so we can use (5.8) as the estimate for Fresnel reflections, too

$$\gamma_{F_\Gamma,\text{Fresnel}} = \frac{5}{2}NM_\Gamma. \quad (5.9)$$

Next, we have a look at the $(NM_\Gamma) \times M$ matrix A_Γ . First, we note that this matrix only has non-zero entries for rows that refer to radiation arriving at the boundary. The number of non-zeros in those rows depends on the length of the ray, or more specifically on the number of nodes it passes. Here, we restrict ourselves to a square grid of M nodes, consisting of \sqrt{M} grid lines containing \sqrt{M} nodes each. Traversing along the grid lines from one side to another we typically encounter \sqrt{M} nodes; if we are off a grid line we have to interpolate between adjacent node pairs. Therefore, for a typical ray information of about $2\sqrt{M}$ nodes is obtained. This results in the following number of non-zeros

$$\gamma_{A_\Gamma} = NM_\Gamma\sqrt{M}. \quad (5.10)$$

Since, for a square grid $M_\Gamma \approx 4\sqrt{M}$, this can furthermore be reduced to

$$\gamma_{A_\Gamma} = 4NM. \quad (5.11)$$

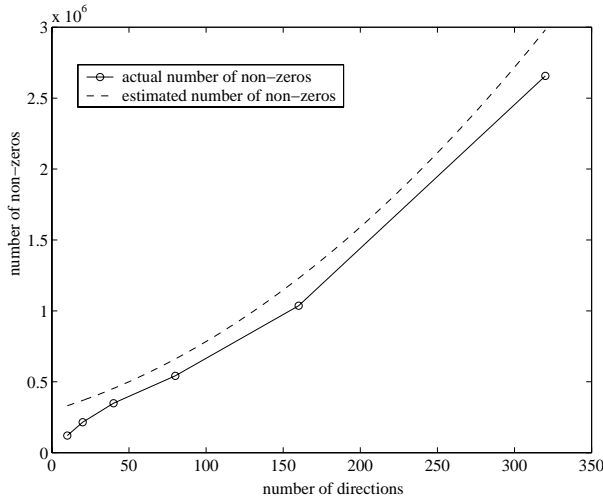


Figure 5.1: Comparison between the estimate for the number of non-zeros with the actual number, for a square containing 545 nodes.

Determining the complexity of the matrices in the domain is easier. If the geometry is convex — and so every node directly sees every other node — G_Ω is a full matrix, or

$$\gamma_{G_\Omega} = (M - M_\Gamma)^2 \approx M^2. \quad (5.12)$$

Finally, the $(M - M_\Gamma) \times (NM_\Gamma)$ matrix R_Ω^* comes from R_Ω , which, as we saw in the discussion of R_Γ , has two non-zero elements per row. So, we find

$$\gamma_{R_\Omega^*} = 2N(M - M_\Gamma) \approx 2NM. \quad (5.13)$$

The sizes of these matrices together with estimates for the number of non-zeroes and the sparsity of the matrices are given in Table 5.1. The sparsity σ of an $n \times m$ matrix is then computed as

$$\sigma = \frac{\gamma}{nm}, \quad (5.14)$$

where n and m are the number of rows and columns, respectively. From this table we see that the total number of non-zeroes is approximately

$$\gamma_{\text{tot,diffuse}} = M^2 + \frac{1}{4}N^2M_\Gamma + 6NM, \quad (5.15)$$

where we left away the lower order terms in N and M . If reflections are omitted, the memory requirements become more independent of the number of directions

$$\gamma_{\text{tot,black}} = M^2 + 6NM. \quad (5.16)$$

For the specular and Fresnel reflection models, a similar number to the latter is found. So, the specularly reflective model does not add additional complexity to the problem, whereas diffuse reflection does. As can be seen in Figure 5.1, the number of non-zeros is quite accurately estimated by the formulas derived above.

For all reflection models the leading term in the complexity is the M^2 needed for G_Ω , as in general the number of directions N is much smaller than the number of nodes. For slender bodies, where M_Γ is not necessarily much smaller than M , and diffuse reflection also the second term in (5.15) has to be taken care of. Since in Chapter 2, we introduced the modified diffusion approximation and a finite element method that in certain cases might be used in stead of G_Ω , some additional work has to be done to make the ARTM attractive to use for the heat flux divergence away from the boundary, too. In the next section, we have a look at one approach to make the ARTM more attractive, but first we have a look at the time complexity of the ARTM.

5.1.2 Time complexity

The second part of the algorithm needs to be repeated every time the radiative cooling is computed. Since in a typical heat computation this needs to be done very frequently these steps are dominant for the time estimates. The radiative heat flux then can be computed using the following steps:

1. Obtain the temperature at the nodes and compute the blackbody intensity in the vector \mathbf{b} ;
2. Compute the right hand side of the system for the boundary:

$$\mathbf{y}_\Gamma := A_\Gamma \mathbf{b} + \mathbf{r}; \quad (5.17)$$

3. Solve the intensities including reflections through the system

$$F_\Gamma \mathbf{h}_\Gamma = \mathbf{y}_\Gamma, \quad (5.18)$$

possibly using the preconditioners computed beforehand.

4. Compute the irradiation at the boundary (\mathbf{g}_Γ) and in the domain (\mathbf{g}_Ω):

$$\mathbf{g}_\Gamma := W_\Gamma \mathbf{h}_\Gamma, \quad (5.19)$$

$$\mathbf{g}_\Omega := R_\Omega^* \mathbf{h}_\Gamma + G_\Omega \mathbf{b}; \quad (5.20)$$

5. Construct the divergence of the heat flux by

$$\mathbf{f} = 4\pi\kappa\mathbf{b} - \kappa \begin{pmatrix} \mathbf{g}_\Gamma \\ \mathbf{g}_\Omega \end{pmatrix}. \quad (5.21)$$

Each of these steps involves a large number of floating point operations, but because steps 1 and 5 operate on vectors only we omit them in the following analysis. The number of floating-point multiplications for a matrix-vector multiplication can easily be estimated by the number of non-zeroes in the matrix. The cost estimate for step 3 is more involved. Using an iterative solver with an appropriate preconditioner simplifies the analysis somewhat, as the cost of solving can be expressed in terms of the number of matrix-vector multiplications and preconditioner solutions. This is done for various iterative methods in [Barrett et al., 1994]. Experiments have been conducted using the BiCG-Stab

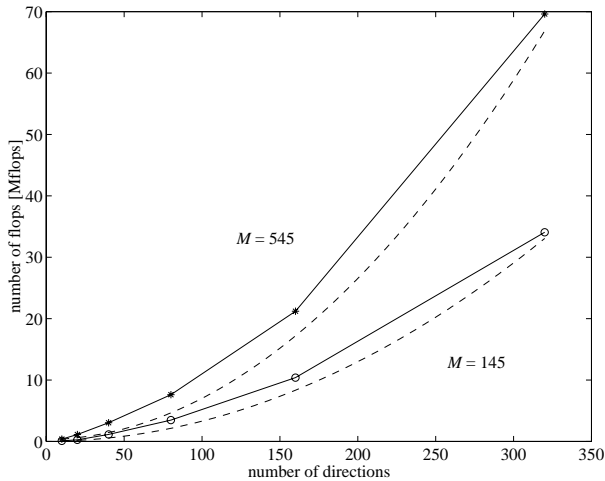


Figure 5.2: Measured and estimated number of flops for two different triangularisations of a square

method in combination with an incomplete LU-decomposition (ILU_ϵ) as preconditioner. During computation of the examples presented later this combination converged in a single iteration step for a suitably small cut-off for the ILU_ϵ .

Note that the number of non-zeros for L and U of the ILU_ϵ -preconditioner will be of the same order as the original matrix for a suitably large cut-off. Therefore, the cost of a preconditioner solution can be estimated proportional to γ_{F_Γ} . If it can be established that the iterative method converges in a fixed number of iterations, the cost of solving the system will asymptotically be a constant times the cost of a matrix-vector multiplication. So, defining ζ as the number of floating-point multiplications, we can estimate the costs of step 3 as

$$\zeta_{\text{step 3}} = \zeta_0 C_{F_\Gamma}, \quad (5.22)$$

where ζ_0 is a constant depending on the chosen iterative method, preconditioner and the number of steps it takes to converge. The factor ζ_0 can be found in [Barrett et al., 1994]. For the BiCG-Stab iterative method that was used for the squares, we find $\zeta_0 = 10$. The major cost of the whole computation thus becomes

$$\zeta = C_{A_\Gamma} + \zeta_0 C_{F_\Gamma} + C_{R_\Omega^*} + C_{G_\Omega}. \quad (5.23)$$

Using the estimates of Table 5.1, this means that the cost of using a diffuse reflection model is

$$\zeta_{\text{tot}} = M^2 + 6NM + \zeta_0 N^2 M_\Gamma. \quad (5.24)$$

Since keeping track of the exact number of floating-point operations in a computer program is almost impossible, the validation of the above relations for the time complexity rely on some kind of measurements of the number of floating point operations. In Figure 5.2 both the measurements and estimates are displayed for two triangulated squares of the same size, but one consisting of 545 nodes, while the other only contains 145 nodes. From the figure we deduce that the estimates mentioned above are reliable.

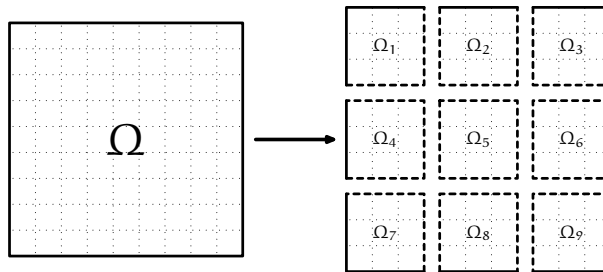


Figure 5.3: Domain decomposition: the original domain Ω is split up into S subdomains. Here $S = 9$ and the domains do not overlap. Note that the subdivision creates extra boundaries. Nodes on these new boundaries belong to more than one domain.

5.1.3 Summary

As was shown, both the memory requirements and the time complexity have a leading term scaling quadratically with the number of nodes M . For a configuration with 10,000 nodes this would require 762MB for a single frequency band, which is at the present limit of memory available to a typical workstation computer. Since present systems can do a matrix-vector multiplication with this size of matrices within seconds, it is especially the memory consumption that needs to be taken care of to make the ARTM more attractive for use in three-dimensional applications.

5.2 Domain decomposition

In the previous section we noted, that it is especially the memory consumption that limits the extent to which the ARTM can be applied. Since furthermore the memory consumption rises quadratically with the number of nodes, intuitively we look for a method that somehow reduces M .

One way to achieve such a reduction is to divide the domain in smaller subdomains, as is shown in Figure 5.3. Since the coefficients in the matrices stem from integration rather than differentiation the subdomains need not overlap. Suppose we divide the original mesh into S subdomains. For simplicity we assume in the following analysis, that each subdomain contains the same number of nodes

$$M_{\text{subdomain}} \approx M/S. \quad (5.25)$$

This is true only approximatively, because — as is also mentioned in the figure — the nodes on the newly created boundaries are duplicated in several subdomains. After dividing the domain, we are left with S smaller radiation problems, which could each be formulated and solved separately in the same manner as the problem on the original domain, if the intensity would be known on the newly created boundaries. Because we do not know the intensity at the interfaces between subdomains a priori, the S problems need to be solved simultaneously or through iteration. In general a domain decomposition always brings communication costs like these.

Here, we look at three different ways of solving the system of equations obtained through domain decomposition, together with complexity estimates for simple

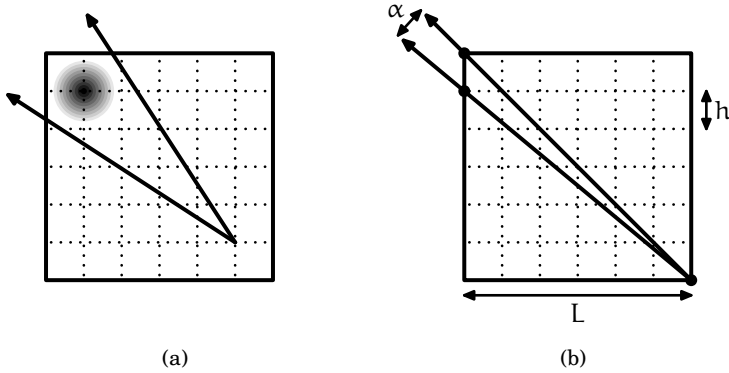


Figure 5.4: (a) In a domain containing a localised hot spot — marked by the dark colours — a limited set of rays will not be able to catch this phenomenon; (b) The definition of the minimum resolution angle to avoid the ray effect.

geometries. The first and simplest method chooses the straightforward approach, viz. divide the domain and iterate. The second method looks more carefully at how to solve the system simultaneously as to avoid an iterative procedure. Finally, the third approach splits up the domain more carefully, to arrive at the same benefits of the second approach, while keeping implementation more simple.

5.2.1 Iterative solution

To solve the decomposed problem through iteration is fairly straightforward: we make an estimate of intensity at the interface nodes, for example by using the solution from a previous time step if a heat problem is solved or by using (3.70). The latter only uses the temperature — through the blackbody intensity — and therefore requires no extra storage. Then, each subdomain can be solved as a separate problem and a new estimate for the intensity at the interface nodes can be made. This whole process then is iterated. The stopping criterion can be based on the change in the discrete total incident radiation g at the interface nodes.

A benefit of this approach is that all solutions are obtained on a small grid. This means that the so-called *ray effect* is less likely to occur. The ray effect occurs when a certain very localised phenomenon is not seen by any of the rays, as is illustrated by Figure 5.4. The likelihood of an occurrence of the ray effect increases as rays are initiated further away from the hot spot. By chopping up the original domain, this effect is less likely to occur; potentially, even fewer rays could be used. One can compute the maximum angle at which all effects are still seen by all nodes. For a square geometry this angle is shown as α in part (b) of the figure. Since, with the definitions of mesh width h and length L , where $h = L/\sqrt{M}$, we find that we should choose the number of directions

$$N \geq 4\pi\sqrt{M}, \quad (5.26)$$

in two-dimensional space to avoid any occurrence of the ray effect. For a large domain, the number of directions thus found is much bigger than one would like

Matrix	$\Upsilon_{1D, \text{domain}}$	$\Upsilon_{1D, \text{total}}$	$\Upsilon_{2D, \text{domain}}$	$\Upsilon_{2D, \text{total}}$
A_Γ	NM/S	NM	$4N(M/S - \sqrt{M/S})$	$4N(M - \sqrt{MS})$
R_Ω^*	$2NM/S$	$2NM$	$\leq NM/S$	$\leq NM$
G_Ω	M^2/S^2	M^2/S	M^2/S^2	M^2/S

Table 5.2: Memory consumption estimates using domain decomposition. Listed are the costs per domain and the total costs of all domains combined.

to take. When decomposing the domain, N will come closer to its optimal value, but only slowly. On the other hand, this approach has the downside that since more boundaries are crossed, intensities are more often interpolated between nodes. This introduces a small level of computational scattering at the interfaces.

Estimates for memory consumption per subdomain could already be made by simply substituting (5.25) into the equations of Table 5.1. However, this would lead to an over-estimation, if the domain contains diffuse boundaries. Because the intensity is prescribed, the interface boundaries act as black boundaries, and there are no extra entries in F_Γ due to reflections.

This effect is most dramatic in a one-dimensional domain. If the original domain has diffusely reflecting boundaries at both ends, after subdivision into $S > 2$ subdomains, only the two subdomains containing the original boundary points contain diffuse boundaries and do so on one of their boundary points only. All the internal subdomains are treated as having black boundaries. This means that

$$\Upsilon_{1D, F_\Gamma, \text{diffuse}, \text{total}} = N^2 + 4(S + 1)N. \quad (5.27)$$

For two-dimensional geometries including axisymmetric ones, the same holds. The total number of non-zeroes in F_Γ is the same as for the original domain, although it is augmented with the cost of the extra interface nodes. A square grid holding M nodes, has about \sqrt{M} boundary points. After dividing the domain in S smaller squares there will be a total of $S\sqrt{M/S}$ boundary nodes. So, $2N(\sqrt{S} - 1)\sqrt{M}$ extra intensities are introduced at the interfaces. For every extra intensity two non-zeroes appear in the appropriate F_Γ for the subdomain under consideration. This leads to the following cost estimate:

$$\Upsilon_{2D, F_\Gamma, \text{diffuse}, \text{total}} = \frac{1}{4}N^2\sqrt{M} + 4(\sqrt{S} + 1)N\sqrt{M}. \quad (5.28)$$

The other matrices do not depend on the reflection model used. Both the capacity per domain as the total capacity are listed in Table 5.2. Leaving out lower order terms, we find that now the total storage demand is as follows:

$$\Upsilon_{1D, \text{total}} = \frac{1}{S}M^2 + 3NM + N^2 + 4(S + 1)N; \quad (5.29)$$

$$\Upsilon_{2D, \text{total}} = \frac{1}{S}M^2 + 5NM + \frac{1}{4}N^2\sqrt{M}. \quad (5.30)$$

In one dimension, all internal domains can easily be chosen to be geometrically equivalent. In this case only one of the internal domains has to be stored together with the two subdomains containing the original boundary points, independent of the number of subdomains

$$\Upsilon_{1D, \text{total}}^* = 3\frac{M^2}{S^2} + 9\frac{NM}{S} + N^2 + 12N. \quad (5.31)$$

A similar trick could be applied to higher-dimensional geometries, especially for problems where the geometries are regular, such as in furnaces and feeders.

As we have seen, domain decomposition leads to a linear reduction of the memory consumption of the ARTM. However, the solution has to be obtained by iteration. The number of iterations required depends on the optical geometry. For one-dimensional optically non-thick geometries, where physical boundaries in different subdomains influence each other, experiments have shown us that about $S/2$ iterations are needed if a multiplicative Schwartz update scheme is used. For an explanation of update schemes in domain decomposition see [Smith et al., 1996]. The number of iterations corresponds to the number of iterations it takes for information of one boundary to reach the other. The number is exact in case of black boundaries and typically rises to S for reflective boundaries. For optically thin geometries the number might rise even more, for optically thick geometries the number is less.

The time complexity can now be computed by multiplying the amount of work for each subdomain by the number of subdomains S and the number of necessary iterations K . The amount of work that needs to be done for each subdomain can be found from (5.24) with adapted values for the sizes. Thus, we find

$$\zeta_{\text{sub}} = \frac{M^2}{S^2} + 6 \frac{NM}{S} + \zeta_0 \frac{N^2 M_\Gamma}{S}. \quad (5.32)$$

For the one-dimensional case, where M_Γ is always 2, this leads to a total time complexity

$$\zeta_{\text{1D}} = S^2 \zeta_{\text{sub}} = M^2 + 6NMS + 2\zeta_0 N^2 S. \quad (5.33)$$

So, while the domain decomposition has a positive effect on the memory requirements, it works out negatively for the time complexity. The work required grows linearly with the number of subdomains.

For geometries in higher dimensions, the domain decomposition does not necessarily suffer from this increase in time complexity. Since the number of iterations depends linearly on the number of subdomains it takes to go from one boundary to another, we argue that for the square domain of Figure 5.3 the number of iterations scales with \sqrt{S} . This leads to a total time complexity of the iterative solution equal to

$$\zeta_{\text{square}} = S\sqrt{S} \zeta_{\text{sub}} = \frac{M^2}{\sqrt{S}} + 6NM\sqrt{S} + \zeta_0 N^2 \sqrt{MS}, \quad (5.34)$$

$$\zeta_{\text{cube}} = S^{4/3} \zeta_{\text{sub}} = \frac{M^2}{S^{2/3}} + 6NM\sqrt[3]{S} + \zeta_0 N^2 \sqrt[3]{MS}, \quad (5.35)$$

where we have used the fact that $M_\Gamma \approx \sqrt{M}$ for a square and $M_\Gamma \approx \sqrt[3]{M}$ for a cube. In Section 5.1, we already saw that using a BiCG-Stab iterative solver to solve the reflection problems means taking $\zeta_0 = 10$. In that case, (5.34) leads to an increase in computing effort if the number of subdomains exceeds S_{opt} defined by

$$S_{\text{opt}} = \frac{1}{2} \frac{M}{N} \frac{5\sqrt{MN} - 3M}{25N^2 - 9M}. \quad (5.36)$$

For slender geometries — such as the neck ring presented in Figures 4.4 and 4.11 in the previous chapter — the number of iterations becomes independent of S .

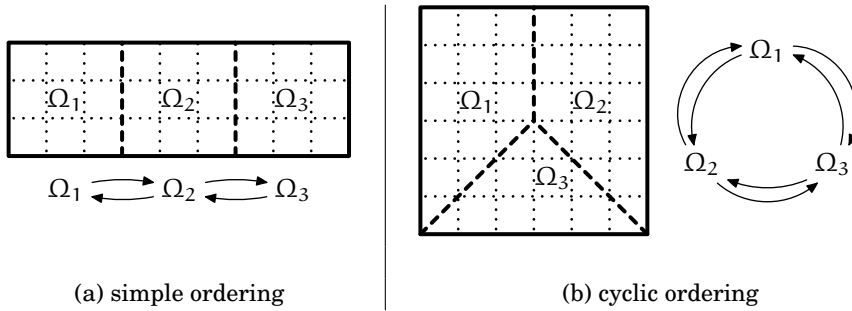


Figure 5.5: Two different possible orderings of the subdomains and their associated graphs. For (a) the associated graph is acyclic; while (b) has an associated cyclic graph.

Because such slender geometries are optically thin in one direction, but optically thick in another, this means that boundaries that influence each other significantly are in either the same or adjacent subdomains, while subdomains further have hardly any influence. In that case the number of floating point operations is

$$\zeta_{\text{slender}} = S \zeta_{\text{sub}} = \frac{M^2}{S} + 6NM + \zeta_0 N^2 M_{\Gamma}. \quad (5.37)$$

This means for slender bodies the time complexity scales similar to the memory consumption: the work done by the large matrix G_{Ω} is reduced linearly, while the effort to solve the boundary equations remains the same.

As we have shown, domain decomposition leads to a linear reduction in memory requirements. However, since the problem on the subdomains is solved in an iterative manner, in general a larger effort needs to be made to solve the various systems. The growth in time-complexity is most noticeable in one-dimensional geometries. For higher dimensions the effect is noticeable to a lesser extent; if the number of nodes is much larger than the number of directions — as often will be the case — there might also be a reduction in computational effort. The iterative solution lends itself particular well for slender geometries, where the influence of a subdomain is typically limited to its direct neighbours.

5.2.2 Direct simultaneous solution

Whereas the simple approach of an iterative solution to the decomposed domain gave the desired reduction in memory consumption, we saw a general increase in time complexity. The rise in time complexity is caused by the fact that for every iteration step, all S boundary systems have to be solved. In Chapter 4 it was shown that the intensity in a node not on the boundary can be computed directly once the intensity on the boundary is known. If we realise that the nodes on the newly created interface boundaries are originally nodes within the domain, it becomes clear that if we could compute the intensities on the original boundary before, the intensities on the interface boundaries follow automatically.

We start by looking at the two domains in Figure 5.5. Both domains are split into three subdomains. However, while the associated graph of (a) is acyclic, the associated graph of (b) is cyclic. As we will show, this has some consequences on the solution method.

For both domains we use the following notation. The boundary of the original domain that is part of subdomain Ω_1 is denoted by Γ_1 , and likewise for the other domains. The newly created interface boundary between subdomains Ω_1 and Ω_2 is referred to as boundary $\Gamma_{1,2}$. The other interface boundaries are referred to in the same fashion. In Chapter 4, we already split up the discrete intensity vector \mathbf{h} into a vector \mathbf{h}_Γ containing the intensities on the boundary and another vector \mathbf{h}_Ω containing the intensities in the domain. Here, we further more split \mathbf{h}_Γ into \mathbf{h}_{Γ_1} , \mathbf{h}_{Γ_2} , and \mathbf{h}_{Γ_3} . The intensity vector \mathbf{h}_Ω is split up in \mathbf{h}_{Ω_1} , \mathbf{h}_{Ω_2} , \mathbf{h}_{Ω_3} , $\mathbf{h}_{\Gamma_{1,2}}$, $\mathbf{h}_{\Gamma_{2,3}}$ and for domain (b) additionally $\mathbf{h}_{\Gamma_{1,3}}$. Finally, even the interface intensities are split into two directions: let $\mathbf{h}_{\Gamma_{\alpha,\beta}}^+$ refer to the intensities on $\Gamma_{\alpha,\beta}$ pointing out of Ω_α into Ω_β ; similarly $\mathbf{h}_{\Gamma_{\alpha,\beta}}^-$ stands for the intensities on that interface pointing out of Ω_β into Ω_α .

Here we first concentrate on domain (a). Since with the new notations, not the whole boundary of a subdomain is contained in a single vector, we rewrite (4.18) as follows. For the boundaries of subdomain Ω_1 , we find

$$(I - R_{1,1})\mathbf{h}_{\Gamma_1} = R_{1,1,2}\mathbf{h}_{\Gamma_{1,2}}^- + A_{1,1}\mathbf{b}_{\Omega_1} + \mathbf{r}_{\Omega_1}, \quad (5.38a)$$

$$\mathbf{h}_{\Gamma_{1,2}}^+ = R_{12,1}\mathbf{h}_{\Gamma_1} + A_{12,1}\mathbf{b}_{\Omega_1}, \quad (5.38b)$$

where we left away the subscripts Γ as all these matrices and intensities refer to the boundary. Furthermore, we used the notation $R_{\alpha,\beta}$ to denote the influence of boundary Γ_β on boundary Γ_α and $A_{\alpha,\beta}$ to denote the contribution of domain Ω_β to the intensity at boundary Γ_α . Here, we see that a subdomain does not carry enough information in itself to form a closed system: after all, \mathbf{h}_{Γ_1} depends on $\mathbf{h}_{\Gamma_{1,2}}^-$, while the subdomain only suggests a value for $\mathbf{h}_{\Gamma_{1,2}}^+$. A description for $\mathbf{h}_{\Gamma_{1,2}}^-$ can be found by studying the second subdomain. For the boundaries of Ω_2 , we find

$$(I - R_{2,2})\mathbf{h}_{\Gamma_2} = R_{2,12}\mathbf{h}_{\Gamma_{1,2}}^+ + R_{2,23}\mathbf{h}_{\Gamma_{2,3}}^- + A_{2,2}\mathbf{b}_{\Omega_2} + \mathbf{r}_{\Omega_2}, \quad (5.39a)$$

$$\mathbf{h}_{\Gamma_{1,2}}^- = R_{12,2}\mathbf{h}_{\Gamma_2} + R_{12,23}\mathbf{h}_{\Gamma_{2,3}}^- + A_{12,2}\mathbf{b}_{\Omega_2}, \quad (5.39b)$$

$$\mathbf{h}_{\Gamma_{2,3}}^+ = R_{23,2}\mathbf{h}_{\Gamma_2} + R_{23,12}\mathbf{h}_{\Gamma_{1,2}}^+ + A_{23,2}\mathbf{b}_{\Omega_2}. \quad (5.39c)$$

Finally, the third subdomain prescribes the last unknown $\mathbf{h}_{\Gamma_{2,3}}^-$ as

$$(I - R_{3,3})\mathbf{h}_{\Gamma_3} = R_{3,23}\mathbf{h}_{\Gamma_{2,3}}^+ + A_{3,3}\mathbf{b}_{\Omega_3} + \mathbf{r}_{\Omega_3}, \quad (5.40a)$$

$$\mathbf{h}_{\Gamma_{2,3}}^- = R_{23,3}\mathbf{h}_{\Gamma_3} + A_{23,3}\mathbf{b}_{\Omega_3}. \quad (5.40b)$$

So far these equations correspond to the system we solve iteratively in the previous section. There we would make an initial guess for $\mathbf{h}_{\Gamma_{1,2}}$ and $\mathbf{h}_{\Gamma_{2,3}}$, then compute \mathbf{h}_{Γ_1} , \mathbf{h}_{Γ_2} , and \mathbf{h}_{Γ_3} using above equations, and finally make an update on the interface intensities. However, here we see that the interface intensities have a simple dependence on the original boundary intensities. Elaborating (5.39b) and (5.39c) such that they contain no references to interface intensities on the right-hand side, we find

$$\mathbf{h}_{\Gamma_{1,2}}^- = R_{12,2}\mathbf{h}_{\Gamma_2} + R_{12,23}(R_{23,3}\mathbf{h}_{\Gamma_3} + A_{23,3}\mathbf{b}_{\Omega_3}) + A_{12,2}\mathbf{b}_{\Omega_2}, \quad (5.41a)$$

$$\mathbf{h}_{\Gamma_{2,3}}^+ = R_{23,3}\mathbf{h}_{\Gamma_3} + R_{23,12}(R_{12,1}\mathbf{h}_{\Gamma_1} + A_{12,1}\mathbf{b}_{\Omega_1}) + A_{23,2}\mathbf{b}_{\Omega_2}. \quad (5.41b)$$

Now we can express all the interface intensities in terms of the original boundary intensities, we can construct a separate system for the original boundary intensities

$$\begin{bmatrix} I - R_{1,1} & -R_{1,12}R_{12,2} & -R_{1,12}R_{12,23}R_{23,3} \\ -R_{2,12}R_{12,1} & I - R_{2,2} & -R_{2,23}R_{23,3} \\ -R_{3,23}R_{23,12}R_{12,1} & -R_{3,23}R_{23,2} & I - R_{1,1} \end{bmatrix} \begin{bmatrix} \mathbf{h}_{\Gamma_1} \\ \mathbf{h}_{\Gamma_2} \\ \mathbf{h}_{\Gamma_3} \end{bmatrix} = \begin{bmatrix} A_{1,1} & R_{1,12}A_{12,2} & R_{1,12}R_{12,23}A_{23,3} \\ R_{2,12}A_{12,1} & A_{2,2} & R_{2,23}A_{23,3} \\ R_{3,23}R_{23,12}A_{12,1} & R_{3,23}A_{23,2} & A_{3,3} \end{bmatrix} \begin{bmatrix} \mathbf{b}_{\Omega_1} \\ \mathbf{b}_{\Omega_2} \\ \mathbf{b}_{\Omega_3} \end{bmatrix} + \begin{bmatrix} \mathbf{r}_{\Gamma_1} \\ \mathbf{r}_{\Gamma_2} \\ \mathbf{r}_{\Gamma_3} \end{bmatrix}. \quad (5.42)$$

This system is in fact an approximation to the original system (4.18), which here is not obtained by tracing the whole domain, but constructed from the results of the various subdomains. In the matrix elements we recognise a trace like form, e.g. when reading from right to left, the expression $R_{1,12}R_{12,23}R_{23,3}$ takes us from boundary Γ_3 via interface Γ_{23} and interface Γ_{12} to boundary Γ_1 . Similarly, $R_{3,23}A_{23,2}$ takes us from domain Ω_2 via interface Γ_{23} to boundary Γ_3 .

Having constructed the system, we can solve the original boundary intensities for any input \mathbf{b} . The interface intensities then are obtained by (5.38b)–(5.41a). Finally, (4.21b) can then be applied to each subdomain, which gives us the desired result.

The memory complexity associated with this approach is very similar to the iterative approach of solving the ARTM on the decomposed domain. However, we would like to save the matrix products as $R_{1,12}R_{12,23}R_{23,3}$, so we could use them at different time steps. Each of these matrices only contains two non-zero elements per row. So, the memory consumption they add is of lesser order than the elements in (5.30), and the latter equation remains a valid estimate for the memory requirement

$$\gamma_{\text{direct}} = \frac{M^2}{S} + 5NM + \frac{1}{4}N^2\sqrt{M}. \quad (5.43)$$

In this approach the boundary problem has the same size as the non-decomposed domain. Still the full matrices G_{Ω} , now have a much smaller size. Thus, for the time complexity we now achieve the same result as (5.37) for all geometries

$$\zeta_{\text{direct}} = \frac{M^2}{S} + 6NM + \zeta_0 N^2 M_{\Gamma}. \quad (5.44)$$

A drawback is that application of this method might not always be trivial. Looking at domain (b) of Figure 5.5, we see the associated graph is cyclic. Because of this, the interface intensities might not be expressed explicitly. If we make a similar derivation as before, we can for example express $\mathbf{h}_{\Gamma_{12}}^+$ as

$$\begin{aligned} (I - R_{12,13}R_{13,23}R_{23,12})\mathbf{h}_{\Gamma_{12}}^+ = & R_{12,1}\mathbf{h}_{\Gamma_1} + R_{12,13}R_{13,3}\mathbf{h}_{\Gamma_3} + R_{12,13}R_{13,23}R_{23,2}\mathbf{h}_{\Gamma_2} + \\ & A_{12,1}\mathbf{b}_{\Gamma_1} + R_{12,13}A_{13,3}\mathbf{b}_{\Gamma_3} + R_{12,13}R_{13,23}A_{23,2}\mathbf{b}_{\Gamma_2}. \end{aligned} \quad (5.45)$$

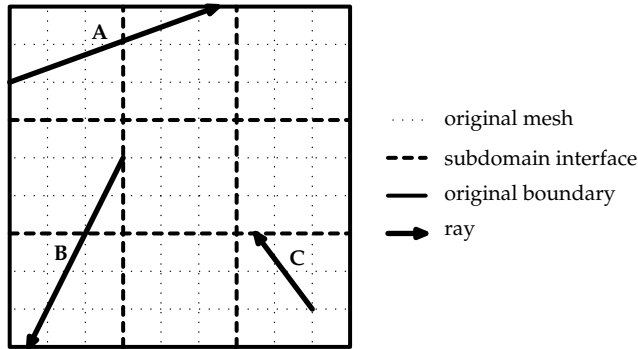


Figure 5.6: Subdivision of the nodes on the original domain in boundary nodes, interface nodes and subdomain nodes. If a node is on the original boundary or on a subdomain interface, rays starting from that node are traced on the original mesh, as illustrated by rays A and B. However, if a node is inside one of the subdomains, the ray is traced on the subdomain only, stopping either a subdomain interface or at a boundary, as shown by ray C.

In case the first subdomain is convex, the product $R_{12,13}R_{13,23}R_{23,12}$ disappears, otherwise we have to find the inverse of that matrix. So, while for domain decompositions with all convex subdomains, we do not need to compute inverses, it is clear that the meta-problem of eliminating the interface intensities can become very involved. How to avoid this meta-problem is studied next.

5.2.3 Modified domain decomposition

As we have seen in the preceding subsections, we can reduce both storage demand and the time complexity using domain decomposition. To achieve a relevant reduction in time complexity, however, we cannot rely on a simple iterative scheme but have to solve a meta-problem first, so the boundary intensities can be solved first and separately from the interface intensities. The meta-problem arises from the fact that ray tracing is done in the subdomains only. To solve the intensities at the boundary, we first have to reconstruct a global boundary problem as was done in (5.42).

The global boundary problem, however, does not necessarily have to be obtained through reconstruction. Remember that the nodes on the interfaces between nodes are just domain nodes on the non-decomposed domain. This means the intensities at those interfaces can be obtained from the boundary intensities by (4.20). Making use of this fact, we can avoid the meta-problem of the last approach.

In Figure 5.6, a domain is decomposed into various subdomains. The subdomains themselves only play a minor role, as it is mostly the classification of the nodes and edges that matters in the approach that we discuss now. Where in the original problem, we made a distinction between boundary nodes and domain nodes, in the *Modified Domain Decomposition* or MDD proposed here, we make an additional distinction between boundary nodes, interface nodes and subdomain nodes. I published the method before in [van der Linden, 2002].

Depending on their class, they are traced differently. The boundary nodes are

treated the same as in the non-decomposed ARTM, i.e. they are traced on the original, large domain. Since domain decomposition did not have an effect on the number of non-zeros in the matrices associated with the boundary problem (4.18), this does not impact the savings obtained through domain decomposition. Just the initial ray trace procedure, which is performed only once, takes longer as the length of the traced rays is longer than if the rays were restricted to a subdomain. This gives us the original boundary problem (4.18)

$$(\mathbf{I} - \mathbf{R}_\Gamma)\mathbf{h}_\Gamma = \mathbf{A}_\Gamma\mathbf{b} + \mathbf{r}.$$

The interface nodes, too, are traced on the original domain, just like all domain nodes would have been in the original problem. In the figure, this operation is shown by ray A. This results in a formulation like (4.20)

$$\mathbf{h}_{\Gamma_i} = \mathbf{R}_{\Gamma_i}\mathbf{h}_{\Gamma_i} + \mathbf{A}_{\Gamma_i}\mathbf{b}, \quad (5.46)$$

where we used Γ_i to denote the interfaces. Then finally, the nodes within the subdomains are traced only until they reach either a boundary or an interface. In the figure, ray B represents this case. For these nodes, we do not need to compute the intensity but can obtain the total incident radiation directly as in (4.21b). So, for each subdomain Ω_s we find

$$\mathbf{g}_{\Omega_s} = \mathbf{R}_{\Omega_s}^*\mathbf{h}_\Gamma + \mathbf{R}_{\Omega_s,i}^*\mathbf{h}_{\Gamma_i} + \mathbf{G}_{\Omega_s}\mathbf{b}_{\Omega_s}. \quad (5.47)$$

Since the interface nodes now are traced on the global domain rather than on subdomains, we find — depending on the number of interface nodes M_i — a slight increase in memory requirement in comparison to the original approach to solving the problem with domain decomposition

$$\gamma_{\text{MDD}} = \frac{(M - M_i)^2}{S} + M_i^2 + 5NM + \frac{1}{4}N^2\sqrt{M}. \quad (5.48)$$

Indeed, as M_i approaches M , the memory savings are nil. This is not surprising, as $M_i = M$ means that all nodes are traced on the global domain. An optimal number of S exists, but depends strongly on the shape of the mesh. In general, making domain cuts on the narrowest parts results in the lowest M_i and therefore the best savings.

Together with the growth of non-zeros the time complexity rises slightly. For the MDD formulation it is estimated as

$$\zeta_{\text{MDD}} = \frac{(M - M_i)^2}{S} + M_i^2 + 6NM + \zeta_0 N^2 M_\Gamma. \quad (5.49)$$

This means that a number of subdomains that is optimal for memory consumption, is likewise optimal for the time complexity.

This approach offers a good trade-off between generality and complexity savings. Whereas the iterative approach does not guarantee a saving in time complexity and the direct simultaneous solution approach requires the solution to a possibly complex meta-problem, the MDD offers similar savings in memory consumption without the need for iteration nor solving a meta-problem. Only in case of a very large number of subdomains and for maximum memory savings, the iterative approach should be used. Depending on the geometry and optical thickness, one might incur a steep increase in time complexity, however.

5.3 Simplification of diffuse boundaries

While the domain decomposition discussed in the previous section performed well in reducing the largest matrix and the work involved, it did nothing to reduce the complexity due to the diffusely radiative terms in R_Γ . This complexity shows up as the $N^2 M_\Gamma$ term in the memory requirement and time complexity and is only present for diffuse reflections; specular and Fresnel reflections as well as black boundaries only incur a complexity proportional to $N M_\Gamma$.

If we look at applications in the glass industry it is likely, that reflections are diffuse. The refractory material of a glass furnace or feeder is naturally diffuse because of its rough surface, while the metal moulds are often smeared with carbon or oil, reducing the specular component. However, we might benefit from the fact that boundaries can be regarded as completely diffuse. After all, in such a case the intensity leaving the boundary is equal in all directions. Below, we study if indeed we can achieve a saving by using this special feature of diffuse boundaries.

Separate the intensities \mathbf{h}_Γ at the boundary in a vector \mathbf{h}_Γ^+ containing the intensities leaving the boundary and another vector \mathbf{h}_Γ^- containing the intensities arriving at the boundary, this can be done using some permutation matrix P consisting of two submatrices P_p and P_m , such that

$$\mathbf{h}_\Gamma = P \begin{pmatrix} \mathbf{h}_\Gamma^+ \\ \mathbf{h}_\Gamma^- \end{pmatrix} = \begin{pmatrix} P_p & P_m \end{pmatrix} \begin{pmatrix} \mathbf{h}_\Gamma^+ \\ \mathbf{h}_\Gamma^- \end{pmatrix} = P_p \mathbf{h}_\Gamma^+ + P_m \mathbf{h}_\Gamma^-. \quad (5.50)$$

To find the new boundary vectors we have to apply the inverse permutation

$$\begin{pmatrix} \mathbf{h}_\Gamma^+ \\ \mathbf{h}_\Gamma^- \end{pmatrix} = P^T \mathbf{h}_\Gamma = \begin{pmatrix} P_p^T \\ P_m^T \end{pmatrix} \mathbf{h}_\Gamma. \quad (5.51)$$

We can reconstruct the original boundary vector then using (5.50). In the ARTM these two new vectors are obtained through two distinct mechanisms. The intensities leaving the boundary are computed through the reflection equations following (4.12), while the intensities arriving at the boundary are obtained through tracing, according to (4.11). Therefore, it seems we could rewrite the boundary problem as follows

$$\begin{pmatrix} I & -R_{pm} \\ -R_{mp} & I \end{pmatrix} \begin{pmatrix} \mathbf{h}_\Gamma^+ \\ \mathbf{h}_\Gamma^- \end{pmatrix} = \begin{pmatrix} \mathbf{r}_p \\ A_m \mathbf{b} \end{pmatrix}, \quad (5.52)$$

with $R_{pm} := P_p^T R_\Gamma P_m$ and $R_{mp} := P_m^T R_\Gamma P_p$. Furthermore, we used $\mathbf{r}_p = P_p^T \mathbf{r}$ and $A_m = P_m^T A_\Gamma$, which both can be obtained by simply leaving out the empty rows. From a system of this form we would be able to construct a separate equation where \mathbf{h}_Γ^+ would be the sole unknown, and proceed with that equation.

However, the form of (5.52) is only obtained ideally. In the ARTM as proposed in the last chapter, when a ray arrives at the boundary after tracing we interpolate the intensity in a specified direction between two points or three points, depending on the mesh. Due to this interpolation we might relate an intensity computed from a trace to another intensity that is computed by tracing rather

than by the reflection equations. In other words an element in \mathbf{h}_Γ^- is dependent on another element in \mathbf{h}_Γ^- . This means that the matrix $R_{mm} = P_m^T R_\Gamma P_m$ is not the null matrix, as was ideally the case in (5.52). Still, as the elements in R_{mm} represent very special cases the number of non-zeroes in R_{mm} is only a fraction of the number of non-zeroes in R_{mp} :

$$\gamma_{R_{mm}} \ll \gamma_{R_{mp}}. \quad (5.53)$$

A similar argument holds for the intensities in \mathbf{h}_Γ^+ . Since the reflection equations can only make use of a limited set of directions, clipping and interpolation can cause an element in \mathbf{h}_Γ^+ to be dependent on another element in that vector. Similar to before, this means that the matrix $R_{pp} = P_p^T R_\Gamma P_p$ is not empty. In this case the occurrence of elements in R_{pp} is more common than an occurrence in R_{mm} . For a diffuse boundary the number of non-zeroes in R_{pp} is about 5% of the number of non-zeroes in R_{pm} . So, while (5.52) represent the ideal case, where geometry and direction set are ideally adapted to each other — a case generally only possible with an infinite number of boundary nodes and directions — the following system represents the real case

$$\begin{pmatrix} I - R_{pp} & -R_{pm} \\ -R_{mp} & I - R_{mm} \end{pmatrix} \begin{pmatrix} \mathbf{h}_\Gamma^+ \\ \mathbf{h}_\Gamma^- \end{pmatrix} = \begin{pmatrix} \mathbf{r}_p \\ A_m \mathbf{b} \end{pmatrix}. \quad (5.54)$$

Eliminating \mathbf{h}_Γ^- from this system we can find the intensity leaving the boundary by solving

$$\left(I - R_{pp} - R_{pm} F_{mm}^{-1} R_{mp} \right) \mathbf{h}_\Gamma^+ = R_{pm} F_{mm}^{-1} A_m \mathbf{b} + \mathbf{r}_p, \quad (5.55)$$

where we used $F_{mm} := I - R_{mm}$. Because R_{mm} has so few elements, computation of the inverse of F_{mm} requires little effort. After solving this equation \mathbf{h}_Γ^- can be obtain, quite straightforwardly by using

$$\mathbf{h}_\Gamma^- = F_{mm}^{-1} R_{mp} \mathbf{h}_\Gamma^+ + F_{mm}^{-1} A_m \mathbf{b}. \quad (5.56)$$

Obviously, with this reformulation we have not yet achieved a complexity reduction. In fact, the matrix in front of \mathbf{h}_Γ^+ in (5.55) typically contains twice as many non-zeroes as the original boundary matrix R_Γ . However, if the boundaries are diffuse we can use the fact that the intensity of radiation leaving the boundary in any direction is equal to the average intensity leaving the boundary. The average outgoing intensity $\bar{I}_\Gamma^+(\mathbf{x}_\Gamma)$ is proportional to the total outgoing intensity $G_\Gamma^+(\mathbf{x}_\Gamma)$ following

$$2\pi \bar{I}_\Gamma^+(\mathbf{x}_\Gamma) = G_\Gamma^+(\mathbf{x}_\Gamma) = \int_{\mathbb{H}^+} I(\mathbf{x}_\Gamma, \mathbf{s}) d\omega. \quad (5.57)$$

Numerically, the discrete total outgoing radiation \mathbf{g}_Γ^+ can be obtained by

$$\mathbf{g}_\Gamma^+ = W^+ \mathbf{h}_\Gamma^+, \quad (5.58)$$

where $W^+ := W P_p$, and W is the quadrature matrix defined in (4.17). For diffuse boundaries we can reconstruct the outgoing intensity perfectly by performing the inverse of the above equation

$$\mathbf{h}_\Gamma^+ = S^+ \mathbf{g}_\Gamma^+, \quad (5.59)$$

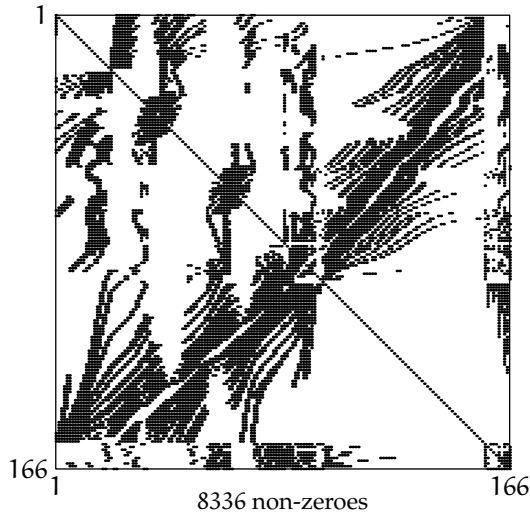


Figure 5.7: Plot of the non-zeros in F^+ for the neck-ring geometry presented in Chapter 4 for completely diffuse boundaries. While the original system involves a $27,888 \times 27,888$ matrix containing 1.2 million non-zeros, diffuse boundaries require only an 166×166 matrix with 8,336 non-zeros.

where S^+ extends \mathbf{g}_Γ^+ into \mathbf{h}_Γ^+ , such that all the elements in \mathbf{h}_Γ^+ corresponding to a certain point \mathbf{x}_j are equal to $g_j^+/2\pi$, independent of the direction \mathbf{s}_i they refer to. In fact, S^+ is a pseudo-inverse of W^+ as $W^+S^+ = I$. Note, that only if \mathbf{h}_Γ^+ does not depend on the direction, (5.59) is a truly inverse operation. For specular or Fresnel reflection this would be a crude approximation.

If we left-multiply equation (5.55) by W^+ , we find that

$$W^+(I - R^+)\mathbf{h}_\Gamma^+ = A^+\mathbf{b} + W^+\mathbf{r}_p, \quad (5.60)$$

where we have introduced $R^+ := R_{pp} + R_{pm}F_{mm}^{-1}R_{mp}$ and $A^+ := W^+R_{pm}F_{mm}^{-1}A_m$. This is an under-determined system, but when we replace \mathbf{h}_Γ^+ using (5.59), we find the square system

$$W^+(I - R^+)S^+\mathbf{g}_\Gamma^+ = A^+\mathbf{b} + W^+\mathbf{r}_p, \quad (5.61)$$

which determines the total outgoing radiation. Whereas W^+ sums up rows, right multiplication with S^+ sums up columns. As we have seen in the previous chapter diffuse reflection creates $N/2$ non-zero entries in the original boundary matrix R_Γ for every outgoing intensity of which there are about $N/2$ per boundary node. The left-multiplication by W^+ and right-multiplication by S^+ sum up all those entries in a single entry in the matrix $F^+ := W^+(I - R^+)S^+$. By doing so, the (N^2M_Γ) term in the memory and time complexity is eliminated.

In Figure 5.7, all the non-zeros are plotted for the matrix F^+ for the neck ring geometry presented in the previous chapter, assuming diffuse reflection on all boundaries. The resulting matrix has less than 10,000 non-zeros whereas R_Γ had $1.2 \cdot 10^6$ and the system $(I - R^+)$ had $2.5 \cdot 10^6$ non-zeros for a direction set with 168 directions. The absolute difference in the computed heat flux between

the original and new method to compute diffuse reflections is less than 10^{-8} times the local blackbody intensity.

In this section we presented an approach to overcome the complexity in memory and time that is introduced by diffuse boundaries. The extra effort that needs to be done for the construction of F^+ is comparable to what would be required for computing the divergence of the heat flux once. Except for the inversion of F_{mm} , which was argued to be cheap, all computations consist of either sparse matrix multiplications or the summing of rows of columns. Because (5.59) is not valid for other reflection models, this approach cannot be used for specular and Fresnel reflections, but by themselves these were already computationally affordable to start with. Next to the large savings in memory consumption that we have obtained by special treatment of diffuse boundaries, the methodology we have followed here is illustrative of the power of the ARTM. By offering a notation, reflections and intensities can be dealt with in algebraic operations. This makes it much easier to find improvements to the method, when faced with a particular challenge.

Applications

In the previous chapters we have concentrated on the derivation of a method for computing radiative heat transport. Since the effects of accurate computation of radiative heat transfer are hard to assess from simply looking at the divergence alone, we look at various applications of the theory derived in this chapter. For a complete treatment, a chapter or even a whole book could be devoted to each of the applications. It is therefore not our goal to treat the application in a thorough and complete manner. Rather the applications are vehicles to show how to use the Algebraic Ray Trace Method and what impact a precise treatment of radiative heat transfer has on the solution. We start this chapter by shortly discussing the heat equation in Section 6.1.

In Section 6.2, the first application studies two stages in the production of a bottle: the so-called dwell and reheat. The elongated geometry of the parison makes one-dimensional modelling of the heat problem possible. Because we can solve 1D problems almost completely analytically, the study of the temperature behaviour in these stages shows the difference between the various numerical radiation models in absence of extra discretisation errors.

The second application studies the dwell in greater detail. In Section 6.3, we consider an axisymmetric model for the top of a jar during a cooling phase. It shows how to use the ARTM in both a transient and intransient heat problem. The transient version of the problem is furthermore used to make a numerical error estimate for the directional discretisation.

Section 6.4 shows the effects of radiation on thermocouple measurements. Insertion of a thermocouple into molten glass changes the radiative field and with it, the temperature distribution. This means that even an ideal thermocouple cannot measure the temperature field as it would be there without the thermocouple. Next to the interesting results, this example also serves as a demonstration of how to treat complicated boundary conditions.

6.1 Heat Equation

For the applications we focus on the heat equation, which can be formulated in general as

$$\rho c_v \frac{DT}{Dt}(\mathbf{x}) = -\nabla \cdot \mathbf{q}(\mathbf{x}) + \Phi(\mathbf{x}), \quad (6.1)$$

where ρ is the *density*, c_v the *specific heat*, and T the temperature. The derivative on the left-hand side represents the total derivative which encompasses both localised change in temperature and convective heat transport, i.e.

$$\frac{DT}{Dt} = \frac{\partial T}{\partial t} + \mathbf{u} \cdot \nabla T, \quad (6.2)$$

where \mathbf{u} represents the speed of the semi-transparent material. The second term, $\rho c_v \mathbf{u} \cdot \nabla T$, is usually referred to as the *convective heat flux* or *convection* in short.

On the right-hand side of (6.1) we have used the combined heat flux, consisting of the radiative heat flux \mathbf{q}_r , on which we have focused so far, and the conductive heat flux \mathbf{q}_c

$$\mathbf{q} = \mathbf{q}_c + \mathbf{q}_r. \quad (6.3)$$

The conductive heat flux can be obtained using *Fourier's Law*, which states that

$$\mathbf{q}_c = -k_c(T) \nabla \cdot T, \quad (6.4)$$

where $k_c(T)$ stands for the *thermal conductivity*, a material property. The thermal conductivity is usually taken to be constant, although it is typically a function of the temperature. Due to the form of (6.4), conductive heat transfer is also referred to as diffusion; a term which we already encountered in the discussion of simple heat transfer approximations in Section 3.2. The second and last term on the right-hand side of (6.1), i.e. $\Phi(\mathbf{x})$, represents a heat source within the medium. This heat source models all other types of heat transfer and generation. Examples of these are heat generation by a viscous flow, heat dissipation because of changing chemical equilibria, or heating of the material through microwaves.

Equation (6.1) is very general. For the applications we study here, we limit ourselves to the treatment of problems without convection and without an additional heat source, i.e. we only look at problems with $\mathbf{u} = \mathbf{0}$ and $\Phi = 0$. The combination of conduction, convection and radiation would give rise to a number of interesting phenomena, such as the occurrence of highly viscous boundary layers. Numerical treatment of convection is a worthy problem by itself, but treatment falls beyond the scope of this dissertation where we want to focus on the heat transfer.

In the remainder of this chapter, we have a closer look at the heat equation and its solution. The first section looks into two different stages in glass bottle production. To clarify the differences between the results obtained with different radiation models we limit ourselves there to an approximative one-dimensional problem rather than studying the full three-dimensional problem. In the second section, we consider a cylindrical geometry that is being used for measurements of glass properties. We have a look at the effects that inserting a thermocouple have on the radiative field and the effect of that change on the measured temperatures. Finally, we study the temperature distribution of the neck ring geometry introduced in earlier chapters.

6.2 Parison

The first application deals with two stages in the production of bottles and jars with the press-and-blow process. We study the two stages during forming of

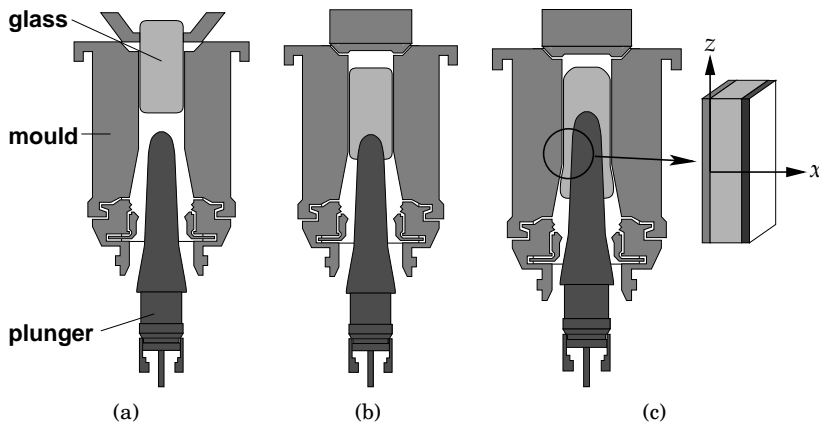


Figure 6.1: The various stages of the pressing phase in a press and blow process: a) The glass enters the mould; b) The plunger presses the glass into form; c) During the dwell the outside of the glass is cooled and solidified. During the dwell part of the parison can be modelled as a slab geometry as is shown in c).

the jar where the glass does not flow. These stages are present in the production especially for heat transfer reasons. We start with an explanation of the press-and-blow process, and then continue to adapt the heat equation to this specific model. As the two stages correspond to different boundary conditions, we use the results to assess the different radiation models. Because the problem is not optically thick, we expect the Rosseland Approximation to perform badly. For clear glasses we expect the problem to be optically thin enough than treatment of radiation can actually be omitted. The results below show, if these expectations are correct. The analysis shown here as also been published as part of [Laevsky, 2002].

The production of glass bottles goes along the following lines. First grains of silica (typically available in the form of sand) and additives, like soda, are heated in a tank. This can be an enormous structure with a typical length of several tens of meters and a width of a couple of meters, positioned several meters above the ground. The depth of the furnace is less impressive and rarely exceeds one meter. Gas burners or electrode heaters provide the necessary heat to liquefy and homogenise the batch products at around 1400°C . From the exit of the oven the glass is led to the forming machinery through a channel called a *feeder*. The feeder should be designed in such a manner that the chemical and thermal homogeneity of the glass melt is preserved.

At the end of the feeder the glass melt can flow through a hole in the bottom of the furnace structure. As the glass flows down it is cut in to gobs of glass melt which then are let to the forming machinery through steep narrow metal guides. The control of the downward flow rate and setting the cutting frequency is essential, as it determines the volume of glass in each gob, which is the same volume of glass that eventually constitutes the bottle.

Modern bottle production consists of two stages, shown in Figures 6.1 and 6.2(c), which have been used with kind permission of K. Laevsky. First the gob is brought to the *pressing mould* as displayed in Figure 6.1(a). In the figure we

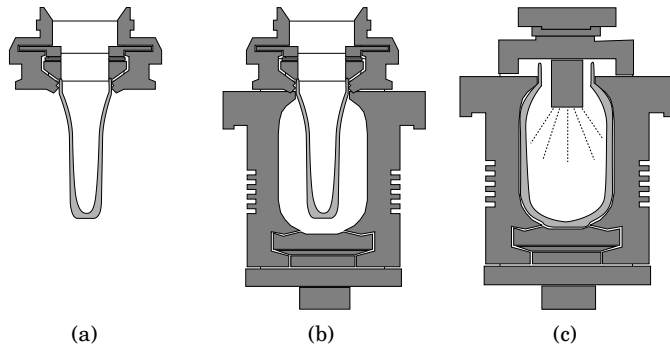


Figure 6.2: The various stages of the blowing phase: a) and b) The plunger is transported from the pressing station to the blowing station and put into the blow mould. During this phase the parison is reheated, i.e. the temperature gradients are weakened; c) The glass is blown into its final stage.

can discern the mould, responsible for the outer form, the *plunger* at the bottom and the gob of glass entering at the top. In the next stage, the mould is closed, see Figure 6.1(b). The plunger then is moved up, as can be seen in the last part of the figure, until the whole cavity between the plunger and mould is filled with glass. Before the half product, the so-called *parison*, is moved to the blowing machine, it is left inside the mould for a second to a couple of seconds, depending on the thickness of the parison, to allow for the outer layer to cool down a bit. This gives the parison a viscous skin, which ensures it retains its shape while it is being moved to the second stage: the blowing machine. The cooling of the skin is called the *dwell*.

The phases of the blowing process are portrayed in Figure 6.2. The blowing stage starts with letting the parison sag without making contact to the blowing mould. This phase allows for the viscous skin to warm up, due to the energy stored in the middle of the glass, and become malleable again. This phase, called the *reheat*, takes about the same time as the *dwell*, i.e. something in the order of seconds. Finally, compressed air is forced into the inside of the parison and the bottle or jar obtains its final shape.

In this section we study the heat transfer of this production process in the two stages where no convection takes place: the *dwell* and the *reheat*. To study the effects of radiation combined with conduction these two cases prove very useful as they represent very different boundary conditions, as is shown below. To simplify the study, we assume a one dimensional geometry. This is possible since both the height of the parison and its radius are much larger than its thickness.

6.2.1 Dwell

During the *dwell* — the stage when the glass is kept in the mould after all the air has been forced out — there is no flow. If the radius and the height of the bottle is much bigger than its thickness, as is usually the case, we can locally approximate the behaviour of the temperature as being one dimensional. It is assumed that the glass makes perfect contact with both the mould on one side and the plunger on the other, so we can assume Dirichlet boundary conditions on

either side. The thickness of the glass layer is denoted by L . In this case, (6.1) simplifies to

$$\rho c_v \frac{\partial T}{\partial t} = -\frac{\partial q_c}{\partial x} - \frac{\partial q_r}{\partial x}, \quad t > 0, \quad 0 < x < L; \quad (6.5)$$

to which the following boundary and initial conditions are added:

$$T(t, 0) = T_{\text{mould}}, \quad T(t, L) = T_{\text{plunger}}, \quad \text{and} \quad T(0, x) = T_0(x). \quad (6.6)$$

If we assume the optical thickness to be large, the Rosseland approximation (3.52) can be used. Therefore, we define the *Rosseland number* Ro as the ratio between radiative and conductive heat transport in the optically thick limit, i.e.

$$Ro := \frac{4n^2 \tilde{\sigma} T_w^3}{k_c \kappa}, \quad (6.7)$$

where T_w is some characteristic temperature, e.g. the temperature of one of the walls or the average thereof. The ratio between the radiative and conductive diffusion parameters can be expressed in terms of the Rosseland number

$$\frac{k_r}{k_c} = \frac{Ro}{3} \vartheta^3, \quad (6.8)$$

where $\vartheta := T/T_w$ is the dimensionless temperature. Remembering we assumed the material properties to be constant, and defining the *thermal diffusivity* to be $\alpha := k_c/\rho c_v$, (6.5) becomes, after dividing left and right-hand side by T_w and k_c :

$$\frac{1}{\alpha} \frac{\partial T}{\partial t} = \frac{\partial}{\partial x} \left[\left(1 + \frac{Ro}{3} \vartheta^3 \right) \frac{\partial T}{\partial x} \right].$$

Next we introduce the *Fourier number*, which represents some dimensionless time, as $\varphi := \alpha t/L^2$. Also the x -coordinate is rendered dimensionless by introducing $\xi := x/L$. Then, after dividing by T_w , the heat equation simplifies to

$$\frac{\partial \vartheta}{\partial \varphi} = \frac{\partial}{\partial \xi} \left[\left(1 + \frac{Ro}{3} \vartheta^3 \right) \frac{\partial \vartheta}{\partial \xi} \right]. \quad (6.9)$$

As we are dealing with radiation, L is not the only length scale of this problem: the reciprocal value of the absorption coefficient, too, gives a length scale. So, alternatively, we can replace the x -coordinate by the optical coordinate $\tau := \kappa L$. The relation between the two dimensionless coordinates is given by

$$\tau = \tau_0 \xi, \quad (6.10)$$

where τ_0 is the optical thickness of the problem. Which dimensionless coordinate is more appropriate is not clear. However, it is easier to compute the radiative heat flux in terms of the optical coordinate τ rather than the usual dimensionless coordinate φ . If we choose for the optical coordinate, the dimensionless time, too, has to be altered. We propose the *optical Fourier number*, defined as $\varphi_r := \alpha \kappa^2 t$, to represent dimensionless time as the heat equation becomes very similar to the earlier formulation

$$\frac{\partial \vartheta}{\partial \varphi_r} = \frac{\partial}{\partial \tau} \left[\left(1 + \frac{Ro}{3} \vartheta^3 \right) \frac{\partial \vartheta}{\partial \tau} \right]. \quad (6.11)$$

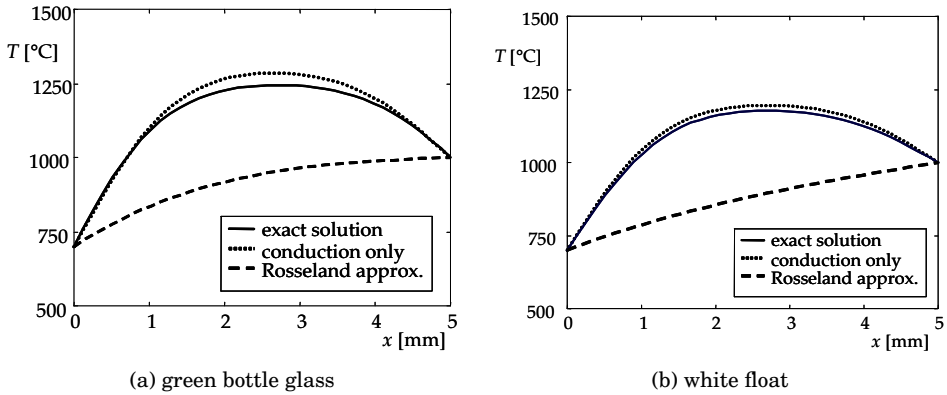


Figure 6.3: Temperature profile after one second dwell (various methods). The exact solution is computed using the ARTM with $\rho_a = 0.5$.

In both dimensionless formulations of the heat equation, we see that the Rosseland number gives an indication of the importance of radiative heat transfer. This remains true if we do not use the Rosseland approximation, but rather some exact method to obtain the radiative flux. We can still perform the same coordinate transformations and if we define the *dimensionless radiative heat flux* as $Q_r := q_r/4n^2\tilde{\sigma}T^4$, we find that the heat equation becomes

$$\frac{\partial \vartheta}{\partial \varphi_r} = \frac{\partial^2 \vartheta}{\partial \tau^2} - \text{Ro} \frac{\partial Q_r}{\partial \tau}. \quad (6.12)$$

In earlier chapters, we have seen that the radiative heat flux scales with the blackbody intensity, so through the limitation of Q_r , it follows that the Rosseland number is still a good indication of the importance of radiation.

For the example, we use a setup taken from an actual pressing setup using the two sample glasses of Table 5.2. We look at the temperature distribution at some height of the parison where the thickness is 5 mm. The mould temperature is taken as 750°C while the plunger temperature is 1000°C ; these temperatures are approximately equal to what is observed in practise. The large difference in temperatures between mould and plunger stems from the fact that the mould is being actively cooled, whereas the latter is not. A higher temperature of the plunger ensures that it moves smoothly into the gob of glass during the pressing.

The initial temperature distribution is taken to be homogeneous at 1250°C . This is an approximation of the real temperature. As the glass is enclosed in the metal mould it is hard to obtain empirical values for this. In reality, at the start of the dwell the temperature will not be constant between the two boundaries. However, we use this approximation as for the pressing phase the change in temperature is usually neglected, see for example [Laevksy et al., 1999]. Furthermore, convection will be dominant during the actual pressing. A more detailed study of this problem is not within the scope of this thesis.

In Figure 6.3, we give the results of the one-dimensional problem for a computation simulating a dwell time of one second. For both glasses, the most eye-catching is the erroneous result that the Rosseland approximation gives us in

this case. We should have been warned by the small optical thickness: $\tau_0 = 1.75$ for the green glass and $\tau_0 = 0.18$ for the white glass. This result is worrying as in industry it is widely used ‘just to take care of radiation’. The results here show that far better results are achieved by simply neglecting the radiation, especially for the white glass. This approximation should be used with great care, since after longer periods the method that neglects radiation, will also deviate severely from the exact solution.

The exact solution in these figures is obtained with the ARTM and a diffuse reflectivity of $\rho_d = 0.5$. The resulting curves for fully black and fully reflective boundary conditions do not deviate much of this result. This is not surprising given the similarity in the radiative heat flux divergence, we already observed in Figure 3.3. A trend that should be noted is that as the reflectivity gets higher, the temperature distribution obtained with an exact method tends more toward the curve obtained by omission of radiation. This is especially true for the white glass where the resulting temperature distribution for purely reflective boundaries almost coincides with that obtained by only considering conductive heat transfer.

The differences between exact solutions for the green and white glass seems smaller than we might expect from the large difference in optical thickness. We noted before, however, that the optical thickness is not the only measure for importance of radiative heat transfer. For the geometrically thin geometry we studied here, over which a large temperature gradient is imposed, also conduction is important. If radiation would be considered without conduction a temperature jump would occur at the boundary. This means that even if we could neglect conduction in the domain, the temperature jump at the boundary would make conductive heat transfer important near the boundary.

This is related to reason the Rosseland approximation fails here. The Rosseland here overestimates the radiative energy transport, because the glass is not thick enough to achieve diffusion-like behaviour throughout the domain. The Dirichlet boundary-conditions applied to both boundaries enforce a large gradient of the thin glass sample. It is this gradient that makes the problem conduction driven, aggravating the results of the Rosseland approximation, which is basically enlarging the effective conductivity. In the figure we see the exact solution is following the solution with only conduction closely near the boundaries, but is flatter within the domain. For these reasons the higher conductivity that the Rosseland method gives, is not the appropriate description of radiation in non-thick domains.

We see from these calculations that for short times (i.e. very small Fourier numbers), the conduction-driven problem can be approximated by omitting radiation. We have seen that this can still be valid for cases in which the optical thickness τ_0 and Rosseland number do not indicate that radiation is unimportant. These numbers do not take the boundary conditions into account and therefore give an incomplete measure for the importance of radiation. Yet, one should be aware that still significant errors are made by such a simple approximation. In this example the maximum error was about 50°C. So, depending on the importance of the temperature and its gradient one can choose between accuracy and speed. In this case, for example, the error of 50°C during the dwell does not give rise to an erroneous prediction of the remainder of the process. Simply omitting radiation

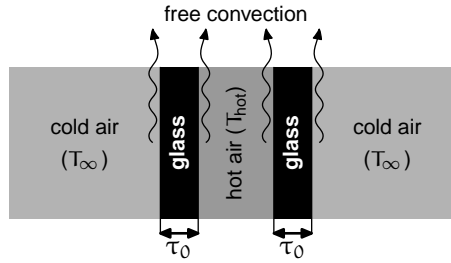


Figure 6.4: The model for the reheating phase. Two infinite glass plates are placed in an infinite atmosphere. The air between the plates can be expected to be hotter. At the edges the glass plates lose heat to the surroundings through free convection and radiation.

would therefore be the most likely candidate for simulations in more dimensions, where the implementation of the exact method brings severe performance penalties.

6.2.2 Reheat

The heat problem in the reheating phase is basically the same as during the dwell; only the boundary conditions differ. During the reheating phase the parison does not make contact with the mould or plunger, but receives radiation from a surrounding atmosphere. From a radiative point of view, this open atmosphere lets itself be modelled accurately as a black boundary, with the ambient temperature as driving temperature. During the dwell, we could impose Dirichlet boundary conditions, as we assumed that the contact between the mould and the glass was perfect and that the mould and plunger had a known and constant temperature. Here, we have to apply a Robin boundary condition describing the heat exchange with the surrounding atmosphere. Since, the *ambient temperature* T_∞ , which we take as standard room temperature (20°C), is much cooler than the parison, we expect it to act as a heat sink.

In Figure 6.4 we show the model for the reheating phase. On the outside we have both convective and radiative cooling of the parison. The convective heat $q_{0,\text{convection}}$ entering the parison on the outside is due to free convection of the surrounding air. It can be calculated by:

$$q_{0,\text{convection}}(t) = h(T_\infty - T(t, 0)), \quad (6.13)$$

where h is the *convective heat transfer coefficient*. Methods to compute this can be found in books like [Tapley and Poston, 1989]. For free convection its value is typically $3\text{--}5 \text{ W/m}^2$.

The method for taking radiative properties into account, depends on the chosen radiation model. If the Rosseland method is used or if radiative heat transport within the medium is neglected altogether, we need to specify the radiative heat losses to the surrounding. This can be done using

$$q_{0,\text{radiation}}(t) = \epsilon \bar{\sigma} (T_\infty^4 - T(t, 0)^4). \quad (6.14)$$

This directly shows one of the problems of not taking internal radiation into account: we need to perform additional approximative modelling to account for phenomena that are not treated by the equations. Since the glass is not an opaque

material, the emissivity ϵ is not just a material property, but depends on the geometry, too. If we imagine the two glass plates are at thermal equilibrium in an isothermal black enclosure, the emissivity will be equal to the absorptivity. It can be determined analytically as follows. Given the intensity B_∞ of radiation entering the glass at certain direction cosine μ , it will travel through the glass, then through the cavity of the parison and then through the glass of the other side of the parison again. Because the hot air neither absorbs nor emits, we see that an intensity of $B_\infty e^{-2\tau_0/\mu}$ caused by the entering radiation, is leaving the glass again. Note that the optical distance that the radiation travels through the glass is $2\tau_0$ rather than τ_0 because we are considering the two glass plates combined. We can now calculate the absorptivity and therefore emissivity ϵ as the quotient of radiation leaving the glass and radiation leaving the glass

$$\epsilon = \alpha = \frac{2\pi B_\infty - 2\pi \int_0^1 \mu B_\infty e^{-2\tau_0/\mu} d\mu}{2\pi B_\infty} = 1 - 2E_2(2\tau_0). \quad (6.15)$$

Referring to the behaviour of the exponential integral, discussed in Appendix A, we see that this equation delivers sensible values for the two extreme cases. For $\tau_0 = 0$, representing an infinitely thin slab or non-participating medium, the emissivity is 0. For large optical thicknesses on the other hand, the emissivity tends to 1. Both these values are as expected.

On the inner side of the parison, the convective heat exchange can be modelled as before:

$$q_{\text{convection}}(t, \tau_0) = h \left(T(t, L) - T_{\text{hot}} \right), \quad (6.16)$$

where T_{hot} is the temperature of the hot air inside the parison. As for the radiative exchange, it does not ‘see’ the surrounding atmosphere (directly), but the other inner side of the parison instead.

The radiative boundary condition for this side of the glass follows from the Fresnel reflection model. However, we can simplify the calculations somewhat by modelling them as specularly reflective. The assumption of a purely specular boundary means that we can treat this boundary as the symmetry plane. To avoid explicit treatment of the radiative boundary conditions we assume the two glass plates are stuck together for the computation of the radiation. Since we only take the left plate into our computations we need to construct the temperature in the right plate in some other matter. Because of the symmetry this is simple: The blackbody intensity on the right half of the domain can be constructed through

$$B(2\tau_0 - \tau) = B(\tau), \quad 0 \leq \tau < \tau_0. \quad (6.17)$$

Computing the radiative heat flux on that domain avoids the inaccuracies associated with the approximative treatment of specular boundaries as was derived in Section 3.1. In that same section, we saw from Figures 3.2 and 3.3 that there is hardly any difference between the results of diffuse and specular reflection. Since for the exact solution to the radiative problem, the diffuse reflections are easier to solve we furthermore model the boundary on the left side as diffusely reflecting.

For the Rosseland approximation and the case without radiation, the radiative heat loss at the right boundary is simple. If we assume that the cavity in between

is filled with normal air — i.e. without high levels of vapour or carbon-dioxide — then we can assume that the cavity itself does not emit or absorb radiation. Because the plates have the same surface temperature on both sides of the cavity, the net heat flux between the two surfaces enclosing the cavity is therefore zero. Concluding, there is no heat loss through radiation at the right boundary for the two simpler models and we can omit the extra term we needed for the other side.

As stated before, the description of the problem in the domain, is the same as for the dwell; so one of equations (6.9), (6.11) or (6.12) can be used for the domain. The Dirichlet boundary equations used for the dwell are replaced by Robin boundary equations to account for the loss of heat at the boundaries. For the model where radiation is omitted, the boundary conditions become

$$-\frac{\partial\vartheta}{\partial\tau}\Big|_{\tau=0} = \text{Nu} \left(\vartheta_\infty - \vartheta(t,0) \right) + \frac{1}{4}\text{Ro} \left(\vartheta_\infty^4/n^2 - \vartheta(t,0)^4 \right), \quad (6.18)$$

for the left boundary. Here we introduced the *Nusselt number* defined in respect to the optical distance $1/\kappa$ as

$$\text{Nu} := \frac{h}{k_c \kappa}. \quad (6.19)$$

For the right-hand side a similar but simpler equation holds because as noted before there is no radiative heat loss on that side

$$\frac{\partial\vartheta}{\partial\tau}\Big|_{\tau=\tau_0} = \text{Nu} \left(\vartheta_\infty - \vartheta(t,\tau_0) \right). \quad (6.20)$$

Since the Rosseland method behaves like a non-linear increase in the conductivity, these boundary conditions have to be adjusted. For the Rosseland method, the dimensionless boundary equations become

$$-\left(1 + \frac{\text{Ro}}{3}\vartheta^3 \right) \frac{\partial\vartheta}{\partial\tau}\Big|_{\tau=0} = \text{Nu} \left(\vartheta_\infty - \vartheta(t,0) \right) + \frac{1}{4}\text{Ro} \left(\vartheta_\infty^4/n^2 - \vartheta(t,0)^4 \right), \quad (6.21)$$

and

$$\left(1 + \frac{\text{Ro}}{3}\vartheta^3 \right) \frac{\partial\vartheta}{\partial\tau}\Big|_{\tau=\tau_0} = \text{Nu} \left(\vartheta_\infty - \vartheta(t,\tau_0) \right). \quad (6.22)$$

In a similar fashion the balance in heat flux for the exact method gives the following boundary conditions

$$-\left(\frac{\partial\vartheta}{\partial\tau} - \text{Ro} Q_r \right)\Big|_{\tau=0} = \text{Nu} \left(\vartheta_\infty - \vartheta(t,0) \right) \quad (6.23)$$

and

$$\left(\frac{\partial\vartheta}{\partial\tau} - \text{Ro} Q_r \right) \frac{\partial\vartheta}{\partial\tau}\Big|_{\tau=\tau_0} = \text{Nu} \left(\vartheta_\infty - \vartheta(t,\tau_0) \right). \quad (6.24)$$

In these equations there is no account for the radiative loss at the boundary, as the exact method and ARTM automatically take losses from the domain to the surroundings into account.

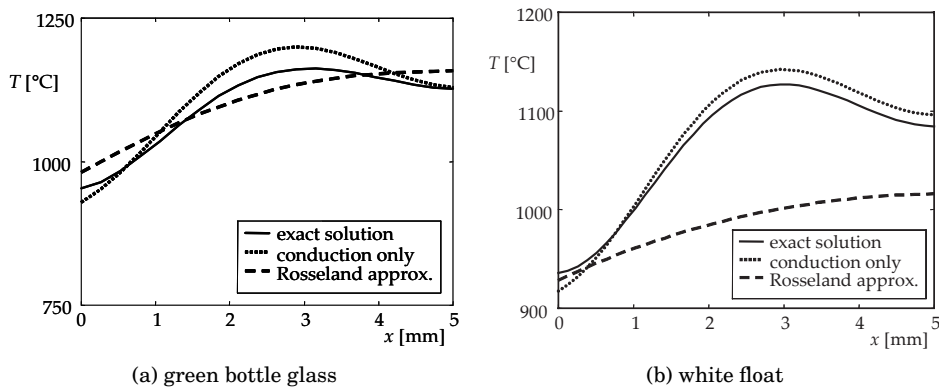


Figure 6.5: Temperature profile after one second dwell and one second of reheating (various methods). The exact solution is computed using the ARTM using specular reflections as an approximation to Fresnel reflections.

The initial solution to the resulting time dependent solution follows from the simulation of the dwell. In Figure 6.5 we present the solution after one second of reheating. For a fair comparison between the three methods, they have been supplied with the same initial solution, i.e. the temperature distribution resulting from a one second dwell simulation using the exact solution.

As we can see in the figure, the three methods give very different results in contrast to what we have seen for the dwell. Unlike during the dwell, however, the Rosseland approximation now gives a good estimate of the energy being extracted during the reheat for the green glass — omission of radiation leads to an underestimate in overall cooling. Both simplifications under-perform in approximating the temperature gradients, which are so important during the reheat.

The conclusion is clear. During reheating, in a case where neither the conduction (as in the optical thin case) nor the radiation (as in the optical thick case) is predominant, only an exact approach gives trustworthy results. If it has been identified that either the temperature itself or its gradient is critical to the functioning of the process, effort has to be made to get the radiative heat transfer right. Two numbers, the optical thickness τ_0 and the Rosseland number Ro , can assist in determining whether this effort has to be made. From comparing the results of the dwell and the reheat, however, we see that these two numbers by themselves are not conclusive. The Dirichlet-conditions applied in the dwell, and thus applying a large temperature gradient over a small distance, forced the conduction to be dominant. Natural boundary conditions as during the reheat, however, give value to the two afore mentioned numbers.

As we show below, the results for these simple one-dimensional cases translate well into higher dimensional geometries. In a conduction-dominated problem, i.e. where large temperature gradients are imposed on the glass, the difference between the exact method and omission of radiation is limited. Whether the difference can be neglected depends on the application. For the dwell and the reheat the exact temperature distribution does not play a major role; for glass cooling it plays a more significant role. The Rosseland method was not intended

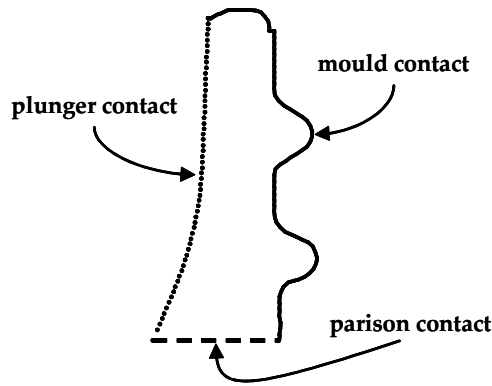


Figure 6.6: Definition of the three different sections of the neck ring boundary. On the right the neck ring makes contact with the mould, on the left with the parison and at the bottom with the remainder of the parison.

for the thin geometries considered here, and it must be no surprise that it does not perform well. If the boundary conditions are of the Robin or Von Neumann type, the differences between the various methods becomes more clear. For green glass, the Rosseland method gives a more accurate prediction of the total heat loss from the glass, than what would be achieved with leaving radiation out of consideration.

So, while the Rosseland number and optical thickness of the problem give some indication of the relative importance of radiation, it is not possible to decide whether to leave out radiation or take it into account based solely on these indicators. The type of boundary conditions plays an important role. Furthermore, we saw that for the simpler radiation models, the construction of the boundary conditions is not straightforward. For semi-transparent media radiative heat losses do not only occur at the boundary, but part of energy from within the domain is permitted to leave. Therefore, use of the exact solution or the ARTM might prove more convenient as it bypasses a complicated modelling of the boundaries. For higher dimensions, the ARTM is preferred, as we do not have an exact solution available in that case.

6.3 Neck ring cooling

The results for the one-dimensional problem in the previous section are very instructive. For one-dimension, we have an approximative analytical solution, which we lack in higher dimensions. Whether the conclusions that we drew for that case translate into higher dimensions is studied for Dirichlet boundary conditions in this section. To that end, we study a heat problem in the neck ring geometry that we introduced before. As the neck ring is part of the parison, the dwell provides a nice problem for study. The neck ring geometry of Figures 4.4 and 4.11 has some artifacts that make it very hard to study analytically: the outer surface has a double curvature and the object is non-convex. For the ARTM of Chapter 4, these artifacts are automatically accounted for thanks to the ray trace mechanism that lays at the base of that method.

The setup of the problem is similar to that of the previous section. The glass is enclosed between a mould and a plunger which make perfect contact with the glass and are kept at a constant temperature. In this analysis we assume that the mould and the plunger both have a 80% specular reflectivity. Figure 6.6 shows which parts of the glass of the neck ring are in contact with the mould and with the plunger. At the bottom of the neck ring we see the part of the neck ring where it is connected to the remainder of the parison. Rather than calculating the temperature distribution in the whole parison, which would be needed for an accurate description of the temperature at this interface, we model it as a black boundary, where we furthermore prescribe the temperature as linearly changing from the plunger temperature to the mould temperature.

This setup is used below to study a couple of problems. We start by studying neck ring in thermal equilibrium as it gives an indication of the importance of radiation. Furthermore, we use the steady problem for measurements of the time penalty that is incurred in using the ARTM in comparison to simpler methods as the Rosseland Approximation. Since most processes in glass industry are not steady but inherently transient in nature — the glass starts at a very high temperature and during its processing is brought down to room temperature — we study the transient problem next. The transient problem shows that the temperature history varies more between the different radiation models than what is indicated by the steady problem. In the final part of this section, we use the transient problem for constructing a numerical error estimate for the directional discretisation.

6.3.1 Thermal equilibrium

In contrast to the previous section, here we start the study with heat problem in equilibrium. This means that the model where treatment of radiation is omitted can be represented quite simply as a Laplace problem:

$$\nabla^2 u = 0, \mathbf{x} \in \Omega \quad \text{and} \quad u(\mathbf{x}) = g(\mathbf{x}), \mathbf{x} \in \Gamma, \quad (6.25)$$

where for our problem $u(\mathbf{x})$ represents the absolute temperature. Because we are dealing with an axisymmetric geometry the problem is best defined using the cylindrical coordinates (r, z) . In these coordinates the Laplace equation becomes

$$\frac{\partial^2 u}{\partial r^2} + \frac{1}{r} \frac{\partial u}{\partial r} + \frac{\partial^2 u}{\partial z^2} = 0, \quad (6.26)$$

which after multiplication by r can be written as

$$\nabla_r \cdot [r \nabla_r u] = 0, \quad (6.27)$$

if we define ∇_r as

$$\nabla_r := \left(\frac{\partial}{\partial r} \quad \frac{\partial}{\partial z} \right)^T. \quad (6.28)$$

This form is convenient if we want to use a two-dimensional solution method. For the Rosseland approximation we have to take account for the non-linear diffusion coefficient and find

$$\nabla \cdot [A(u) \nabla u] = 0, \mathbf{x} \in \Omega \quad \text{and} \quad u(\mathbf{x}) = g(\mathbf{x}), \mathbf{x} \in \Gamma, \quad (6.29)$$

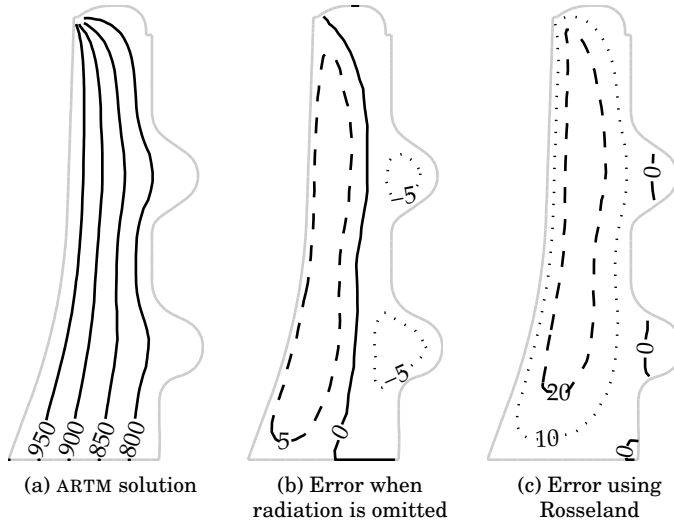


Figure 6.7: Solution to the stationary heat problem for the neck ring geometry with green glass as a medium. Figure (a) shows the solution obtained using the ARTM as radiation model. Figure (b) shows the difference with this solution if radiation was omitted from the heat equation. Figure (c) shows the difference if the Rosseland approximation was used instead. All numeric labels refer to degrees centigrade.

where $A(u)$ is the non-linear diffusion coefficient, defined as $A(u) = k_c + k_R(u)$. The coefficient $k_R(u)$ is the Rosseland diffusion coefficient defined by (3.53). Using cylindrical coordinates, this problem reads

$$\nabla_r \cdot [r A(u) \nabla_r u] = 0. \quad (6.30)$$

The formulation of the ARTM does not change the diffusion coefficient. Since it needs the temperature to compute the divergence of the heat flux, it is best implemented as a non-linear source term. The heat problem then is defined by

$$-k_c \nabla^2 u = f(u), \quad \mathbf{x} \in \Omega \quad \text{and} \quad u(\mathbf{x}) = g(\mathbf{x}), \quad \mathbf{x} \in \Gamma. \quad (6.31)$$

Here, the source term $f(u)$ is the radiative heat flux divergence $\nabla \cdot \mathbf{q}_r$, which can be computed by the ARTM. Note, that the ARTM does not take a single value of $u(\mathbf{x})$ to compute $f(u)$ at a given point \mathbf{x} , but the whole solution u throughout the domain of interest Ω . In cylindrical coordinates this problem is formulated as

$$-k_c \nabla_r \cdot [r \nabla_r u] = r f(u). \quad (6.32)$$

So, for all three radiation models we are able to express the problem in the general form

$$-\nabla_r \cdot [a(u, r) \nabla_r u] = b(u, r). \quad (6.33)$$

This type of equation, which is non-linear for both the Rosseland method and the ARTM, can be solved using an off-the-shelf solver.

In Figure 6.7 the solution to the heat problem is presented for the three methods using the green sample glass of Table 3.1. As in the previous section the mould

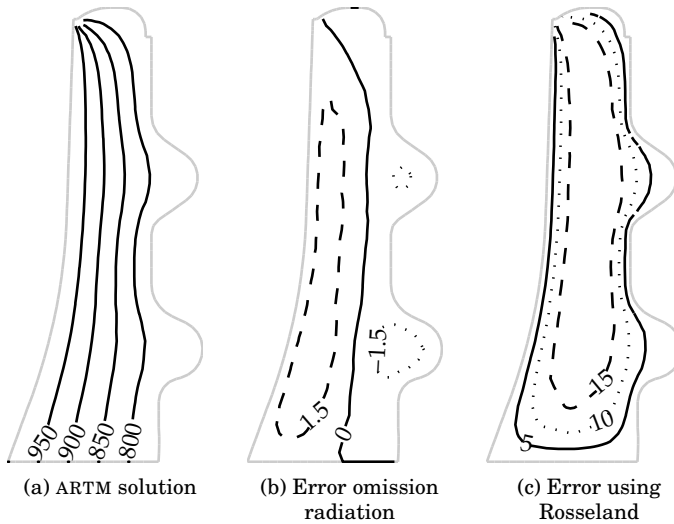


Figure 6.8: Solution to the stationary heat problem for the neck ring geometry with white glass as a medium. Figure (a) shows the solution obtained using the ARTM as radiation model. Figure (b) shows the difference with this solution if radiation was omitted from the heat equation. Figure (c) shows the difference if the Rosseland approximation was used instead. All numeric labels refer to degrees centigrade.

temperature was set to 1000°C and the plunger temperature 750°C . The solution for the ARTM shows the contours of several temperature levels, expressed in degrees Celsius. Because the difference between the contour lines is not clearly visible, for the two simpler models the difference with the ARTM solution is shown. The maximum error incurred by omitting radiation is 8°C , while the maximum error for the Rosseland method was almost 25°C . Although the difference seem small for such a large imposed gradient, the temperature gradient in the neck ring matters a lot. This is actually the only part of the parison that receives its final shape in the pressing phase. As the parison is moved between the two machines by gripping it at this part, the neck ring is continuously cooled during the process. If gradients are too big during this period, unwanted internal stresses may lead to fracture at the neck ring. This is a common problem in the production of jars and bottles.

The solution of the Rosseland approximation and the ARTM is obtained by making use of the same non-linear solver. Therefore, it is interesting to see the factual cost in time that using the ARTM implies. For convergence, 10 iterations were necessary for the ARTM method. This means that the radiative heat flux, too, had to be computed 10 times. In total this took 8.6 s. Unsurprisingly, the Rosseland approximation converged much faster and was finished after 0.4 s. So, the ARTM was over 20 times slower for this problem.

Figure 6.8 shows the solution to the same problem for the white float glass of Table 3.1. As could be expected, the error by omitting radiation is much smaller for this very transparent glass. The maximum difference in temperature is only 2°C . At these small differences it is hard to justify the extra effort that has to be made for obtaining a more accurate solution using the ARTM. The behaviour

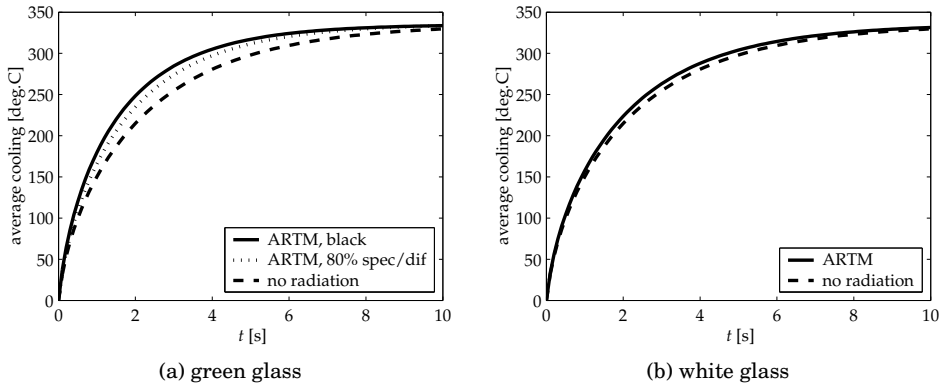


Figure 6.9: Average temperature in time for a neck ring geometry. For green glass different reflection models are shown. For the white glass only the black boundary solution was computed

of the Rosseland approximation is also as expected. Because the geometry under consideration is optically thin rather than optically thick, it fails, which here means a difference of 20°C compared to the ARTM.

Because the absorption coefficients are tenfold lower for this glass in comparison to the green glass, much less dampening occurs along the rays. This results in higher valued elements in the matrices obtained using the ARTM and shows its effect in the time needed for computation of the heat flux divergence. Although in this case only 6 iterations were needed to converge, it took 12 s to evaluate these. In this case also the Rosseland approximation took longer to converge: 0.9 s. So, with respect to the Rosseland approximation white glass makes the ARTM a bit more attractive as it is only 15 times slower.

6.3.2 Transient problem

Although the steady problem gives some indication of the relative importance of accuracy of the treatment of radiative heat transfer, it does not do justice to the time dependence of many processes in glass production. Outside the furnace and feeder, where largely steady flows dominate the heat transfer, most processes in glass production involve a certain cooling of the glass. This is especially true for the neck ring geometry we have considered here. Already during the dwell at the end of the pressing phase in bottle production, as was discussed in Section 6.2, the neck ring is formed and cooled down. For a simulation of that cooling down, we make use of the transient heat equation (6.2), which for axisymmetric geometries looks like

$$r \rho c_v \frac{\partial u}{\partial t} - k_c \nabla_r \cdot [r \nabla_r u] = r f(u). \quad (6.34)$$

Here, we use the same boundary conditions as for the steady problem, i.e. the temperatures at the boundary are prescribed, making a distinction between the plunger interface, the mould interface and the contact with the remainder of the bottle. Because we are dealing with a transient problem, we need to supply

an initial solution u_0 . As with the discussion of the dwell in Section 6.2.1, we assume the glass has a uniform temperature of 1250°C at the start of the dwell. Such a distribution, however, is inconsistent with the boundary conditions of the problem. To avoid large numerical errors that would affect the discussion of the accuracy below, we therefore construct the initial solution by solving the following steady state problem

$$-k_c \nabla_r \cdot [r \nabla_r u_0] = \lambda r (T^* - u_0), \quad (6.35)$$

to which the same boundary conditions as before are added. If we choose the parameter λ large enough the resulting solution will be near homogeneous close to the desired temperature T^* within the domain, while remaining compatible to the applied boundary conditions. The initial solution that is used hereafter is a solution of (6.35) with λ chosen — fairly arbitrarily — as $5 \cdot 10^7$.

As it is hard to portray higher dimensional transient data, we concentrate here on the average temperature in the neck ring. The *average temperature* is defined by

$$\bar{T}(t) := \frac{1}{V} \int_V u(\mathbf{x}, t) dV, \quad (6.36)$$

where V is the whole volume and $u(\mathbf{x}, t)$ is the solution of the transient problem, i.e. the temperature at \mathbf{x} at time t . If the specific heat and density are constant, the average temperature is related to the internal thermal energy E by

$$E = \rho c_v V \bar{T}. \quad (6.37)$$

Since we only have the discrete solution and a true integration over the volume of the neck ring is complicated, we approximate it simply by

$$\bar{T}(t) \approx \frac{\sum_i A_i r_{c,i} u(r_{c,i}, t)}{\sum_i A_i r_{c,i}}, \quad (6.38)$$

where A_i is the area of the i -th triangle in the mesh, $r_{c,i}$ is the r -coordinate of the centre of the triangle, and $u(r_{c,i}, t)$ is the temperature interpolated at that centre. Sometimes it is more convenient to show the change in the average temperature. To that end we introduce the *average cooling* defined by

$$\Delta T(t) := \bar{T}(t) - \bar{T}(0). \quad (6.39)$$

In Figure 6.9 we show the result of the transient problem for the first 10 seconds. The figure displays the change in the average cooling within the neck ring for green and white glass and for two different radiation models: the ARTM and the omission of radiation. For the green glass, furthermore, the various reflection models are displayed. Because they nearly overlap, the curve for the 80% diffuse and 80% specular boundary conditions are shown as a single curve. For the white glass only the curve corresponding to black boundaries is shown.

From the figure we immediately see that the temperature difference between the ARTM and the no-radiation model is much larger in time than the steady state difference. For the green glass with black boundaries a maximum difference is reached after 1.8 seconds, when the ARTM has cooled the neck ring 33.5°C more

than conduction would have done alone. For the 80% diffuse and specular reflection boundaries, the maximum is 20.1°C and 20.8°C respectively; both maxima are reached after 2.2 seconds. For the white glass the maximum transient difference is less: the maximum difference is 8.8°C and is reached after 2.1 seconds.

It is not surprising that omission of radiation always underestimates the cooling rate: the ARTM in the shape of the functional $f(u)$ in (6.34) is added as an extra heat flux. In contrast to the steady problem, we clearly see that treatment of radiation is important. Because too quick cooling can lead to cracks forming in the glass, it is important to know and control the cooling rate. Fracture near the neck ring is one of the most common production errors in glass bottle production. As expected, radiative heat transfer plays a more important role for the optically thicker green glass than for the near-transparent white glass.

6.3.3 Accuracy of directional discretisation

In Section 4.2, we found an analytical error estimate for the spatial discretisation needed for the ARTM. In that section we failed to come up with a theoretical estimate for the influence of the number of directions. Here, we use the transient heat problem to obtain such convergence results experimentally.

The setup of the problem is the same as before. The neck ring starts the dwell with a nearly homogeneous temperature distribution and then is left between plunger and mould, both at constant temperature, to cool down. There are many factors that determine the eventual accuracy of the computations, but by only varying the number of directions N in the formulation of the ARTM we hope to clarify the influence of the size of the directional set on the final accuracy.

Here we use the quasi-homogeneous sets that were presented in Section 3.3. The following set sizes were used to compute the solution to (6.34):

$$N \in \{8, 24, 48, 80, 120, 160, 168\}. \quad (6.40)$$

These all correspond to the specific number needed for the level-symmetric sets and for special symmetry of the quasi-homogeneous sets as given by (3.98), except for the set with 160 directions.

Because we do not have an exact solution, we use the solution obtained using the set with 168 directions as the reference. The difference with the solution obtained by this set is measured by the following distinct quantities. The first is the *average relative error*, defined in terms of the difference in the average temperature as

$$\epsilon_{\text{av}}(N) := \max_{0 \leq t < t_0} \left| \frac{\bar{T}_N(t) - \bar{T}_{168}(t)}{\bar{T}_{168}(t)} \right|, \quad (6.41)$$

where \bar{T}_N is the average temperature obtained with the set of N directions. As the average temperature is related linearly to the internal thermal energy through (6.36), this measure also indicates the accuracy with which energy is conserved.

In Figure 6.10 the distribution of the relative error over the domain is shown for three different direction sets. Because there are only a few regions with larger error, we can expect the maximum local error to be significantly larger than the

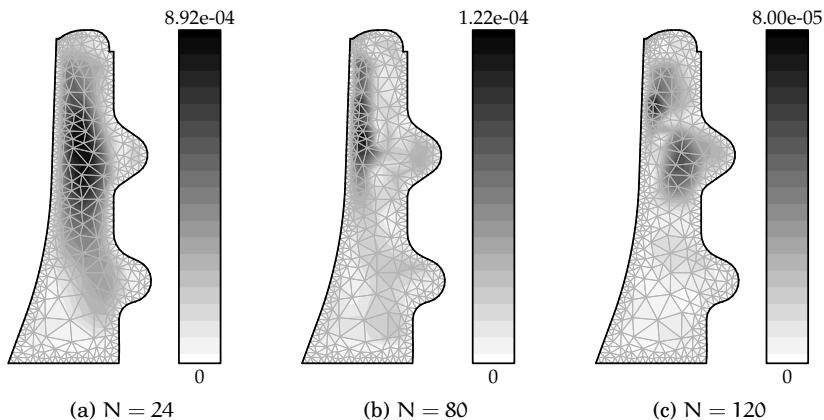


Figure 6.10: Distribution of the relative error after 10 seconds dwell for three different direction sets with varying number of directions N . The mesh is kept the same.

average error. Therefore we introduce another measure, which indicates the *maximum local error*. Defined as

$$\epsilon_{\max}(N) := \max_{0 \leq t < t_0} \max_i \left| \frac{\bar{u}_N(\mathbf{x}_i, t) - u_{168}(\mathbf{x}_i, t)}{u_{168}(\mathbf{x}_i, t)} \right|, \quad (6.42)$$

where u_N represents the solution obtained with the set with N directions, it portrays the effect of the number of directions on the maximum error in the temperature.

The average error and the maximum local error are displayed in Figure 6.11 for a variety of cases. In Figure 6.11(a) we compare the average error for different boundary conditions: black boundaries, 80% diffusely reflective boundaries and 80% specularly reflective boundaries. In all cases the error decreases with increasing N , as we expect. Understandably, the error is large for the two reflective cases. After all, they do not only use the DOM for the directional quadrature in the computation of the total incident radiation, but also in the solution of the radiative boundary equations. Although the discussion of the DOM in Section 3.3 suggests otherwise, the set with 160 directions seems to give more accurate results here. However, that is not the case if white glass was used rather than green glass as can be seen in Figure 6.11(b). The average error does not decrease beyond 80 directions. This could be due to an aberration in the direction set for 80 directions, as that set breaks the trend for the green glass, too; albeit in the opposite direction.

The bottom two Figures 6.11(c) and 6.11(d) show similar graphs for the maximum local error. As we noted before, this error is larger than the average error, here by about a factor ten. The largest deviation from the average error can be seen in Figure 6.11(c), by the fact that now there is hardly any difference in accuracy between the three boundary radiation models. This is explained by the error distribution in Figure 6.10, where we see that the maximum error occurs in the domain and not close to the boundary. The error by solving the discretized version of the radiative boundary equations has a smaller effect here than the

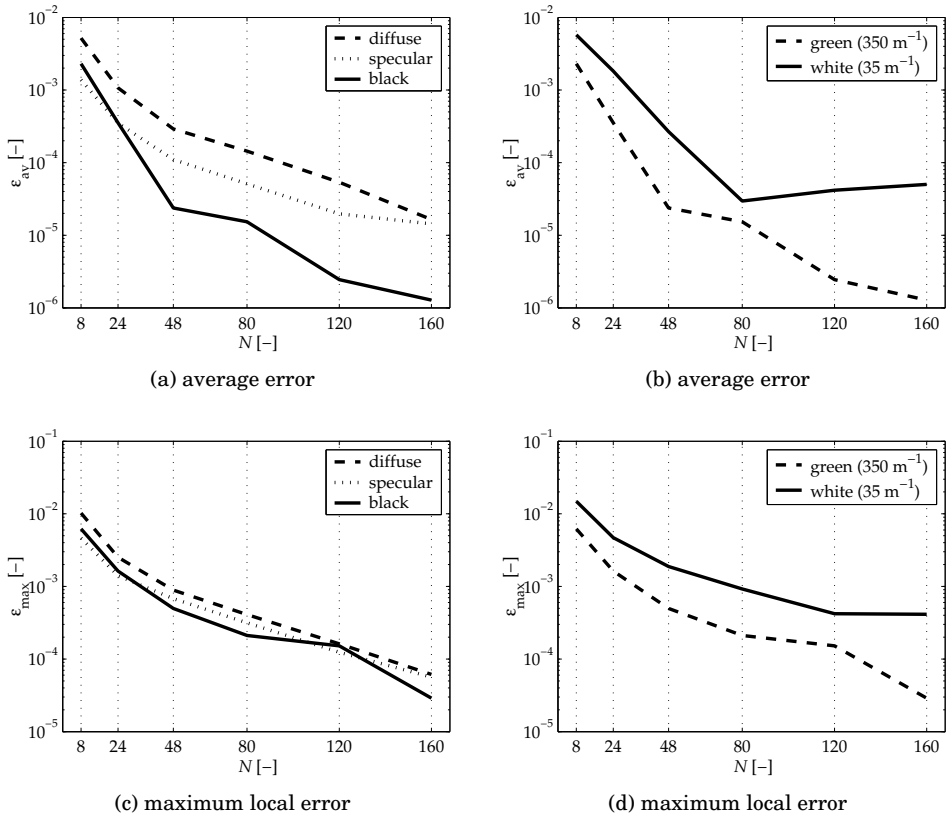


Figure 6.11: Influence of the size N of the DOM direction set on the accuracy of the temperature distribution in the neck ring geometry after a 10 second dwell: (a,c) for different kinds of radiative boundary conditions; (b,d) for glasses of different optical thickness.

error in the directional quadrature used to compute the total incident radiation at a point.

From the graphs in Figure 6.11 we can approximate the asymptotic behaviour of the accuracy. To achieve that we want to fit a curve for the error such that the error can be described by

$$\epsilon(N) = \alpha N^{-p}, \quad (6.43)$$

where the coefficients α and p can be obtained using a least-squares approximation, as we have a set of values for N with corresponding values for the error. The factor α is less interesting for investigating the accuracy than the exponent p . Therefore in Table 6.1 we only list the exponent for the asymptotic approximation. For the least-squares approximation used to determine the exponent p listed in the table, we omitted the results for the direction set with only 8 directions as it lay outside the common trend for all cases.

Not all curves could be properly fitted using the approximation (6.43). Specifically the curves for the reflective boundaries showed a progressively faster convergence for higher N . The values listed in the table should therefore be seen as lower limits. On the other hand for white glass, the curves did not converge

Glass	Boundary	Error measure	Order of convergence p
Green	black	ϵ_{\max}	2.0
		ϵ_{av}	2.9
	80% diffuse	ϵ_{\max}	1.8 ^a
		ϵ_{av}	2.1 ^a
	80% specular	ϵ_{\max}	1.7 ^a
		ϵ_{av}	1.7
White	black	ϵ_{\max}	1.4 ^b
		ϵ_{av}	2.0 ^b

Table 6.1: Order of convergence for the error estimates of the parabolic problem. The orders marked with an *a* show increasing convergence with increasing number of directions, while the orders marked with *b* do not show any convergence for $N > 80$.

for $N > 80$ as we already observed before. This explains the lower corresponding values of p that can be seen in the table. Furthermore, slower convergence of white glass cases can be explained by the fact that due to the lower absorption coefficient the boundary has a bigger effect within the domain. Since the applied boundary conditions here are non-differentiable and the weights were optimised for smoothly varying functions, we can expect the error to vanish more slowly.

From these measurements it follows that the error vanishes for large N faster than $\mathbf{O}(N^{-1})$ in all cases, but usually with an higher order. The average error vanishes more quickly than the maximum local error. Taking the remarks above into account, that explained the lower values for the reflective boundaries, we see that the average error vanishes faster than $\mathbf{O}(N^{-2})$. The maximum local error vanishes slightly less quickly. These convergence rates comply with what is to be expected from a trapezoidal rule. Given the fact that the convergence is usually faster than these conservative estimates, we see that the quasi-homogeneous sets portray some of the super-convergence that the periodic chained trapezoidal rule exhibits, although it does not do so completely. This is because the intensity does not satisfy the smoothness requirements to obtain super-convergence, especially close to the boundary where there can be sudden jumps from one direction to the other. In general though, the quasi-homogeneous direction sets show sufficient convergence, so the number of directions need not to be increased a lot to have more accuracy.

From the numeric error estimates in Figure 6.11, we can estimate the average accuracy for the set with 160 directions. With the temperature around 1000°C , the accuracy for green glass is about one thousandth of a degree, while for white glass the accuracy is about one tenth of a degree. These values are adequate for all but the most demanding computations. The accuracy of the white glass is lower, as the effects of the directionally non-smooth intensity and influences from the boundary propagate further into the glass, making the average error behave much like the maximum local error. For this problem, we have shown that enough precision can be obtained with a limited number of directions.

6.3.4 Overview of results

In this section we showed how to use the ARTM in an actual heat computation. In general it can be treated as a non-linear source term, which makes it suitable

to be used with existing methods. We observed that for the time independent case the accurate treatment of radiative heat transfer does not make a large difference. We saw that for green glass the error made by omission of radiation is limited to about five degrees; for white glass the difference was even less. This small difference does not necessarily justify omission: in Figure 6.7 we can observe that the error in the gradient is over 10°C on a distance of a couple of millimetres, which can make a lot of difference when internal stresses in the finished glass product are studied. As before, we had to conclude that the Rosseland approximation for optically thick problems, does not work out for the small thicknesses seen in forming processes.

The solutions for thermal equilibrium were used as a benchmark. From these tests it followed that the ARTM is about 20 times slower than the Rosseland approximation for this specific case. In Chapter 5 we already addressed methods to speed up the ARTM. For thermal equilibrium, the difference between omitting radiation and taking it into account, did not make a large difference. However, we showed that for the transient case radiative heat transfer is important. Omission of radiative heat transfer leads to a slower cooling rate, which means that before arriving at the steady case the error can grow large. In Figure 6.9 we showed that for the green glass the error caused by omission of radiation can grow to over thirty degrees. This error is reached after approximately two seconds, which is a typical time for the dwell. For white glass, again, radiation is less important, although the difference can grow to ten degrees in a few seconds.

Finally, we used the transient case to construct a numerical accuracy estimate for the DOM, for which we did not obtain a theoretical result before. The results have shown, that the quasi-homogeneous sets already give accurate results for small direction sets, although white glass needs more directions than green glass does.

6.4 Crucible with thermocouple

The final application that we treat in this chapter, looks at how radiative heat transfer influences temperature measurements. For the acquisition of empirical glass data accurate knowledge of the temperature distribution is desirable. Often temperature information is obtained by using thermocouples which are inserted into the glass melt. Examples of where we see this in practise is in the control system of a glass furnace, which is steered by temperature data obtained from the feeder at the outlet of the furnace, and in the setup of material data acquisition.

Thermocouple measurements at high temperatures and immersed in fluids can be inaccurate for a number of reasons, e.g. heat fluxes through the wiring of the thermocouple can cause erroneous feedback in the measured signal. For semi-transparent media such as molten glass there is an additional source of errors. The transparency of the media leads to the effect that the thermocouple ‘sees’ the temperature around it. Consequently, it does not measure the temperature locally, but rather some sort of an average of the media around the thermocouple. Or, more precisely, if we assume perfect contact between the thermocouple and the medium, insertion of the thermocouple into the medium alters the radiative field.

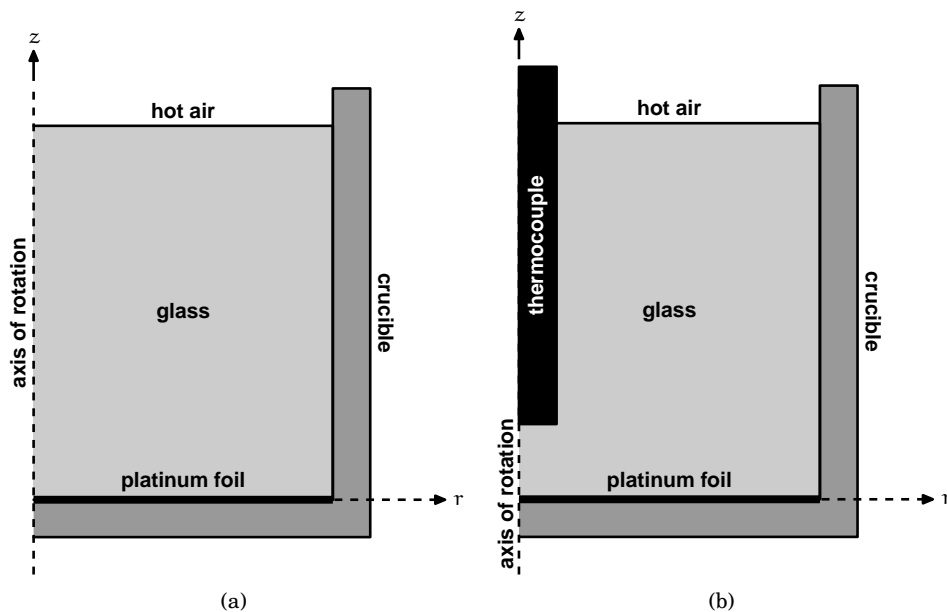


Figure 6.12: Description of the geometrical situation of the crucible without thermocouple (a) and with thermocouple (b). Both problems consider the temperature distribution in the glass only. The presence of the thermocouple means different boundary conditions are used on the left side of the geometry.

In this section we look at how much the radiative field is changed by insertion of a thermocouple. A change in radiative field would induce a change in temperature, which means that the thermocouple cannot but measure a different temperature, independent on how accurate the thermocouple is. As the object of our study we use a small cylindrical crucible, that is used in a sister-project described in [Nagtegaal, 2002], which aims to develop a spectral remote sensing technique for measuring temperature gradients in glass melts. The crucible has a 4 cm radius made of alumina and has the bottom covered with platinum foil to reduce the influence of the bottom on intensity measurements. The depth of the glass in this crucible is 5 cm. The crucible itself is placed inside an oven. The top of the glass therefore makes contact with hot air at about 1000°C.

This setup offers a variety of boundary conditions, which we will discuss shortly. The first geometry presented in Figure 6.12(a) shows the geometry that we use for the crucible before insertion of the thermocouple. Since the crucible geometry is axisymmetric, we reuse equations (6.27) and (6.32) to describe the problem within the domain. Whereas in the previous section we only applied Dirichlet boundary conditions and specular reflective radiative boundary conditions, we have to use a more diverse set here. The bottom of the crucible, thanks to the presence of the platinum foil, can still be described with specular reflectivity and a Dirichlet boundary condition. Empirical data for platinum shows that it is about 90% specular reflective, although accurate data about the reflectivity of platinum immersed in glass is lacking. For the bottom, here, we furthermore

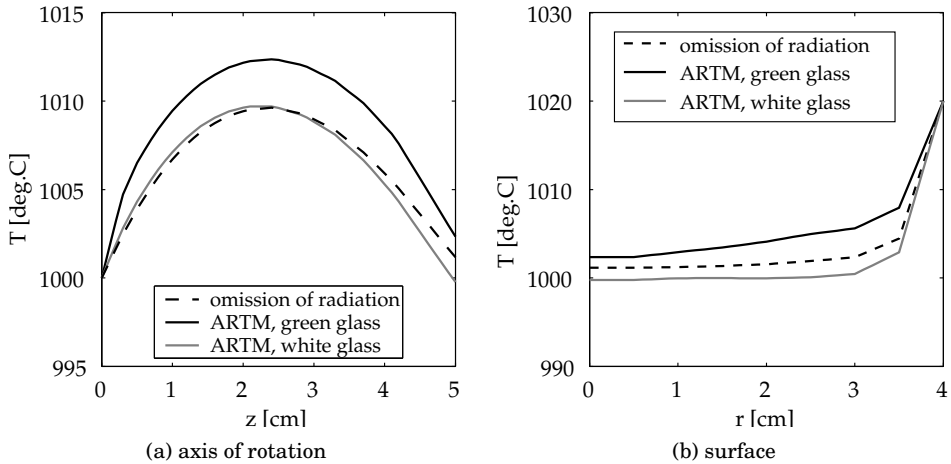


Figure 6.13: Stationary solution of the heat problem for different radiation models and glasses; (a) shows the temperature distribution along the axis of rotation of the glass, while (b) shows the temperature at the surface.

prescribe the temperature at the bottom as a parabolic profile

$$T_{\text{bottom}}(r) = 1000^{\circ}\text{C} + 20^{\circ}\text{C} \cdot (r/R)^2, \quad (6.44)$$

where R is the radius of the crucible. The temperature is also prescribed for the sleeve of the crucible, i.e. the right-hand side of the geometry. We assume that it has constant temperature $T_{\text{sleeve}} = 1020^{\circ}\text{C}$. For the radiative boundary conditions we use the diffuse reflection model. Again, no accurate data is available for the reflectivity; in literature figures vary from 30%–80%. Here we use 80% to maximise the effect as a test for the presented method.

The left side of the geometry represents the axis of rotation. It is prescribed by a homogeneous Neumann boundary condition

$$-\mathbf{e}_r \cdot \nabla_r T_{\text{axis}}(\mathbf{x}_\Gamma) = 0, \quad \text{for all } \mathbf{x}_\Gamma \text{ on the axis of rotation}, \quad (6.45)$$

where \mathbf{e}_r represents the basis vector in r -direction in the (r, z) -plane. Since the axis of rotation is not a boundary proper we do not need to specify the radiative boundary condition.

The top of the glass represents the most interesting case. Since the glass does not make contact with an opaque boundary, more complex mechanisms are at play. For the radiative boundary condition we can use the Fresnel reflection model of Section 2.3. Fresnel reflections can be seen as specular reflections, where the reflectivity depends on the angle of incidence. Like specular reflections the implementation of Fresnel reflections is straight forward. However, there are some differences:

- Fresnel reflections are exclusive. Unlike the specular and diffuse reflection models, which we could combine by varying the reflectivities, the Fresnel reflection model prescribes the reflectivity as a function of the angle of incidence. Therefore it does not allow a combination with one of the other models.

- The Fresnel model has a direction dependent emissivity. Whereas the emissivity for the specular and diffuse reflection models is constant in all (outgoing) directions, the Fresnel emissivity is depending on direction. This means that an implementation of the ARTM should be able to have the emissivity specified on a directional basis, too, and not just for different positions.

The thermal boundary conditions are follow from balance of the heat fluxes at the boundary. For the model without (internal) radiation the resulting non-linear Robin boundary conditions are given by

$$-\mathbf{e}_z \cdot k_c \nabla_r T(\mathbf{x}_\Gamma) = h[T_\infty - T(\mathbf{x}_\Gamma)] + \bar{\sigma}[T_\infty^4 - T(\mathbf{x}_\Gamma)^4], \quad (6.46)$$

where \mathbf{e}_z is the unit vector in z -direction, h is the convective heat transfer coefficient first introduced in (6.16), and $\bar{\sigma}$ is the Stefan-Boltzmann coefficient. The temperature of the hot air inside the oven is given by T_∞ is taken as 1000°C . For convenience we assumed that the part of the oven that the top of the glass ‘sees’ can be modelled as a blackbody radiating at the same temperature. The boundary conditions can be written as

$$-\mathbf{e}_z \cdot k_c \nabla_r T(\mathbf{x}_\Gamma) + \mathbf{e}_z \cdot \mathbf{q}_r(\mathbf{x}_\Gamma) = h[T_\infty - T(\mathbf{x}_\Gamma)], \quad (6.47)$$

where \mathbf{q}_r can be computed from the temperature using the ARTM. In fact, to compute the heat flux numerically we need to know the boundary intensity vector \mathbf{h}_Γ . Through the DOM, we then can approximate the heat flux $\mathbf{q}(\mathbf{x}_j)$ itself as

$$\mathbf{q}(\mathbf{x}_j) \doteq \sum_{i=1}^N w_i h_{ij} \mathbf{s}_i, \quad (6.48)$$

where the vectors \mathbf{s}_i are the directions in our direction set and the coefficients w_i are the corresponding quadrature weights from the DOM. The vector \mathbf{h}_Γ is actually a side product of the ARTM computation. So, in principle, a non-linear finite element solver finds the right-hand side in (6.31) and the radiative term in (6.47) in one step. Some solvers need separate computation of these terms, in which case we need to do the ARTM step twice: once for the computation of $\nabla \cdot \mathbf{q}$ and once for the computation of \mathbf{q} itself.

The second geometry, displayed in Figure 6.12(b), portrays the domain after insertion of a thermocouple of diameter such that it enters from the top along the axis of rotation with its end 1 cm above the bottom of the crucible. In the following computations we first look at a thermocouple of 1 mm diameter. Later, we also consider a thicker thermocouple construction. The vertical position is chosen arbitrarily here; in practise one would measure at different heights of the crucible to obtain information on temperature gradient. The horizontal position, of course, is chosen less arbitrarily. By putting it along the axis of symmetry we preserve rotational symmetry of the problem. We assume that the heat flux within the thermocouple is negligible, i.e. $k_c = 0$ within the thermocouple, and that it takes the temperature of the immediate surrounding at every point. This avoids having to compute the temperature distribution within the thermocouple itself. As there is no heat flow within the thermocouple, we have a balance between the conductive and radiative heat fluxes perpendicular to the surface

$$\mathbf{n}(\mathbf{x}_\Gamma) \cdot (\mathbf{q}_r(\mathbf{x}_\Gamma) - k_c \nabla T(\mathbf{x}_\Gamma)) = 0, \quad (6.49)$$

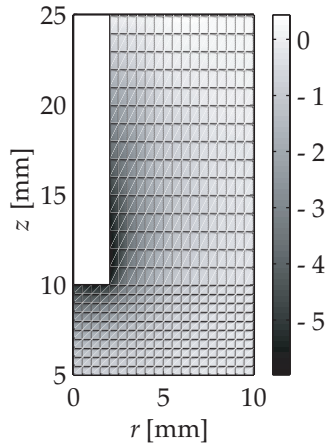


Figure 6.14: Change in temperature between actual temperature and the temperature seen by the thermocouple for a 4 mm thick thermocouple placed in a crucible with white glass and a parabolic temperature profile over r .

for all \mathbf{x}_Γ on the thermocouple/glass interface. For the radiative boundary conditions we assume the thermocouple wire to have a diffuse reflectivity of 80% along the thread, while the shiny metal bottom has a specular reflectivity of 90%.

In Figure 6.13, we show the solution to the above problems for some intersection in the geometry. The first figure shows the solution along the centreline of the crucible, while the second shows the temperature of the free surface. The solution of the ARTM for the white glass and the solution of the problem where radiation was omitted correspond closely, although the temperature near the boundary the deviation becomes larger. The maximum difference between the solutions remains within 5°C, but considering this is dependent on the gradient imposed on the bottom, this should not be a reason to discard treatment of radiative heat transfer. The imposed gradient here spanned 20°C only. Below, we have a closer look at the influence that the imposed gradient has on the solution.

Rather than comparing the methods, we are interested here in the difference between the case with and the case without a thermocouple, as this gives an indication of the disturbance of the radiative field that the presence of the thermocouple wire brings. The difference between these two cases is shown in Figure 6.14 for a small region around the head of the thermocouple. For greater effect and clarity we used a 4 mm thick thermocouple in white glass; the result would be similar but less outspoken for a thinner thermocouple in green glass. Although such a thick thermocouple might seem unrealistic at first sight, we will show that this actually represents the measurements more realistically.

To further investigate the change in temperature due to the presence of the thermocouple wire, we slightly adjust the problem definition so we can impose an arbitrary gradient over the glass. To that end we replace the free boundary at the top by an opaque boundary. All the opaque boundaries are furthermore assumed to be black, which is done solely to speed up computation. On this geometry we impose a linear temperature gradient in either r -direction or z -direction. For the former we prescribe the temperature on the top and bottom as

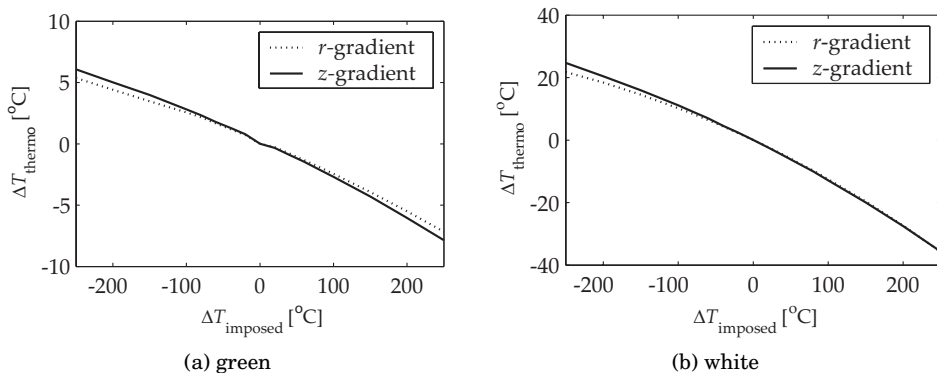


Figure 6.15: Change in temperature at the head of a 1 mm thick thermocouple for varying imposed temperature gradients. Shown are the results for green bottle glass and white float glass.

$T(\mathbf{x}_r) = 1000^\circ\text{C} + \Delta T(r/R)$ while we take as $T(\mathbf{x}_r) = 1000^\circ\text{C} + \Delta T$ on the cylinder sleeve. The imposed temperature difference ΔT can be chosen arbitrarily. For the z -gradient we similarly prescribe the temperature on the cylinder sleeve as $T(\mathbf{x}_r) = 1000^\circ\text{C} + \Delta T(r/R)$, while the bottom is kept constant at 1000°C and the top is constant at $1000^\circ\text{C} + \Delta T$.

In Figure 6.15, we show the change in temperature at the head of the 1 mm thick thermocouple that is induced by inserting the thermocouple into this configuration for the green and white glass we have encountered before. The figure also shows the resulting change in temperature for a gradient in both r and z -direction. The two curves do not differ much, which is due to the fact that an imposed linear r -gradient induces a gradient in z -direction. The thermocouple induces the largest temperature change for the white glass, which is not surprising as the low absorption coefficient lets it see more of the boundary further away and at a different temperature. The measurement errors due to change in radiative field fall within the accuracy of real thermocouples for moderate temperature gradients in green glass. For white glass the induced change is noticeable, even for low temperature gradients.

While a thermocouple is a thin wire, it is usually embedded inside a protecting cover which is considerably thicker, rather than directly inserting the thermocouple into the glass. The cover is used to protect the thermocouple and to give it enough stiffness such that it can be inserted and moved around in the very viscous glass. For example, for the measurements inside the crucible a hollow alumina stick is used as a cover with a diameter of approximately 4 mm. If we consider the cover and the thermocouple as a single object, we can use the same equations as before for the heat problem. In Figure 6.16 the measurement errors introduced by the thicker thermocouple are shown. As expected the effect is larger for both the white and the green glass. The errors introduced are now significant for the green glass, too. This suggests that thermocouple measurements should always be adjusted for the fact they measure a sort of average temperature surrounding of a point rather than the temperature at a point itself. This behaviour makes thermocouple measurements unsuitable for measurements on

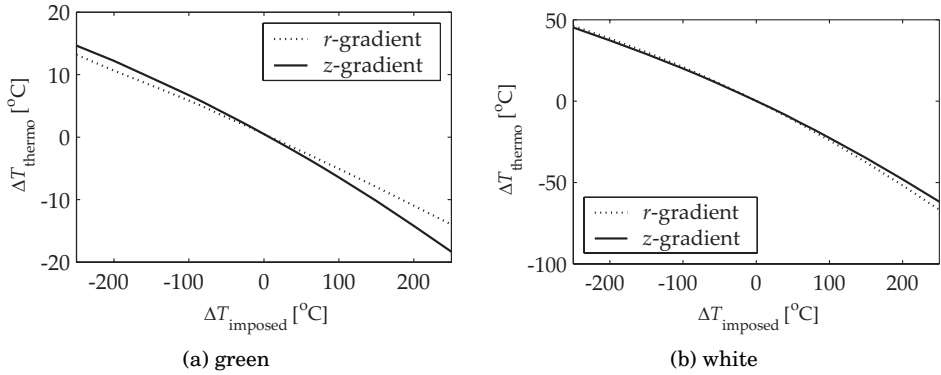


Figure 6.16: Change in temperature at the head of a 4 mm thick thermocouple for varying imposed temperature gradients. Shown are the results for green bottle glass and white float glass.

gradients, as they will appear smoother than they really are.

In this section we have shown how the ARTM can be used with more complex boundary conditions. In the computation of the effects of a thermocouple on the temperature distribution, we used all three of the reflection models. Furthermore, we have shown the usage of the ARTM in combination with Neumann and Robin boundary conditions. The latter needs the heat flux itself rather than its divergence. This puts some constraints on the efficient use of the ARTM. The heat flux on the boundary can be constructed from the boundary intensity vector \mathbf{h}_Γ , which is available as a side product from the computation of the divergence of the heat flux. To avoid duplication of effort this means it is most efficient if the divergence of the heat flux and the computation of the boundary conditions should happen at the same time. Not all solvers allow for these to be computed at the same time. A solution for this problem depends on the implementation of the solver, which means a general solution cannot be given. In the worst case \mathbf{h}_Γ has to be computed twice and the method will be approximately twice as slow, as the computation of \mathbf{h}_Γ is the usually the most time consuming operation of the ARTM.

Here, we have shown that thermocouples in hot semi-transparent media make an inherent measurement error, because the change the temperature at a position by their very presence. This is not an error caused by inaccuracy of the thermocouple itself, but rather an error inherent to temperature measurements that make contact with the glass. The mere presence of a non-transparent object within the glass melt means the radiative field gets altered and a different temperature distribution follows. Even if a thermocouple is fault-free, it cannot measure the temperature at a point accurately. As a thermocouple measures a kind of averaged temperature around the point, gradients will appear flattened when measured with a thermocouple. Here we have shown that the measurement error is dependent on the gradient that is imposed on the boundaries. This means that for good calibration of the thermocouple measurements, one needs to know the approximate temperature gradients expected in the glass melt.

In recent years, research has been underway for contact free temperature mea-

surements, such as in [Nagtegaal, 2002]. These so-called spectral remote sensing methods, try to reconstruct a temperature profile by investigating the radiation that leaves the glass at different wavelengths. The major benefits of such an approach are that it can be used in areas where thermocouples would too much interfere with the process. Such methods need *a priori* knowledge of the approximate temperature distribution, which is seen as a drawback. However, the analysis here has shown, that such knowledge is also required for thermocouple measurements, so the drawback seems inherent to temperature measurements in hot molten glass rather than a feature of a specific measurement technique.

Conclusion and recommendations

Radiative heat transfer in semi-transparent media plays an important role in glass production processes. However, existing computational models either oversimplify radiation or are very time consuming. In this thesis we have sought a method that balances these two extremes. The Algebraic Ray Trace Method we have introduced in Chapter 4 closely resembles the classical Ray Trace Method, although its derivation is rooted in the exact analytical solution for radiative heat transfer in one dimension.

The ARTM can be thought of being in the same category as the classical Ray Tracing Method or the Monte Carlo Method in the way that it prefers accuracy over computational cost saving. It follows the physical description of radiation closely. Different reflection models — an important phenomenon in radiative heat transfer — can be implemented easily as we have shown with the specular, diffuse and Fresnel reflection models. In Section 4.2 we have shown that the method is $O(h^2)$, where h is a typical length scale of the mesh elements. In order that the error remains limited for all optically thicknesses, which is not the case for the standard Newton-Cotes quadrature rules, a specialised trapezoidal rule was derived in Section 4.2 for the integration of the intensity along a ray.

Although the method can be seen as favouring accuracy over keeping computational costs down, special care was taken to reduce the complexity. Without taking special measures the complexity of the method allowed axisymmetric heat problems to be solved on a sub-notebook within minutes. On a present day work station class computer, computation times remain within tens of second for all examples presented in this dissertation. For large geometries with thousands of nodes or for optically very thin geometries with highly diffuse boundaries, complexity needs to be reduced.

Rather than working in a numeric and iterative way, the ARTM proposes a symbolic notation for the contribution of the radiation generated within the domain and for the reflection equations at the boundary. This has some major benefits as computational savings can be more easily found or constructed. In Chapter 5 we have shown two examples of this. In Section 5.2 we constructed a domain

decomposition technique for the ARTM that does not need to iterate over the subdomains to find the global solution. The domain decomposition method allows reduction of time and memory complexity that scales linearly with the number of subdomains. In a similar fashion we have used the symbolic notation to squash the complexity associated with diffuse reflections in Section 5.3. The special treatment of diffuse boundaries reduces the memory requirements for the reflection matrices by N^2 , where N is the number of directions. For the set of 168 directions used throughout this dissertation, a saving of over a factor 1000 can thus be achieved.

In Chapter 6 we have demonstrated the use of the ARTM in practical examples. The method was constructed such that it could be used in an arbitrary existing method. As was shown, the present implementation of the ARTM allows itself to be used in that fashion as long as the PDE solver allows a non-linear source term. In Section 6.3 we further investigated the error caused by directional discretisation, for which we failed to find a theoretical estimate. In Section 6 we showed that in for forming processes the often used Rosseland approximation is a wrong choice as its basic assumptions are violated. The example showed that if accurate treatment of radiation is too expensive, radiation is better neglected instead if the boundary conditions impose a large temperature gradient. Together with the discussion of using complicated boundary conditions in Section 6.4 we acknowledged the general hypothesis than thermocouples do not measure a local temperature accurately in glass melts.

One of the minor achievements of this dissertation is the theoretical estimate of the Rosseland depth, the depth at which use of Rosseland approximation is valid, in Section 3.2. Since the Rosseland approximation provides one of the cheapest methods of accounting for radiative heat transfer knowledge of this depth helps to divide the domain such that a more expensive method needs only to be used in a small portion of the domain. Further an improvement was made in finding a quasi-homogeneous direction set by adjustment the weights in Section 3.3.

Because our efforts were concentrated on giving an complete analysis of the Algebraic Ray Trace method, there are some elements that need to be investigated further before it can be used in realistic simulations. The main shortcoming of this thesis lies in the fact that we only considered grey glasses in the numerical treatment of radiation. In practise the absorption coefficient of glass varies orders of magnitude between different frequencies. Fortunately, unlike gasses the absorption spectra of glass are continuous, such that use of a band model is appropriate. Since the radiative heat flux divergence appears as a source term in the heat equation, application of a band model can be straightforward: In an K-band model we can compute the heat flux divergence K times using different values for the absorption coefficient and blackbody intensity for each band. The total contribution of radiation then can be summed up. Such a simple application would raise the costs of the ARTM by a factor K. While K is generally not higher than 25, further research to reduce the extra costs seems appropriate.

Another omission in this thesis is re-entry of rays leaving a glass object at another location. This is largely an implementation problem: Separate code has to be written to follow the rays efficiently through a non-absorbing medium such as air. While it affects the values of the coefficients in the boundary reflection matrices R_Γ in the ARTM, it brings no need for modification of the present analysis.

Problem	Classification	Rosseland	Omission	ARTM
Blowing	thin/not thick	no	no	yes
Feeder	not thick	no	no	yes
Furnace	thick	yes	no	not everywhere
Pressing	thin/not thick	no	yes	yes

Table 7.1: Application areas of various methods

The solution method can remain the same for such configurations.

We end this dissertation, with an overview of the applicable areas of the various methods we have encountered. We have seen that the ARTM can be deployed for both optically thick and thin cases, but we have also seen that the cheaper methods perform equally well in some cases. In Table 7.1 we show the application areas of the methods we have studied in detail here.

Exponential integrals

In the treatment of one-dimensional radiative problems, exponential integrals appeared when integrating over all directions. Exponential integrals are special functions, that can be computed and tabulated. Although, they are not so common as e.g. Bessel functions, many mathematical programs and computer libraries have subroutines that assist in the computation. Here, we have a look at the definition and properties of exponential integrals. The exponential integral of some positive order n is defined by

$$E_n(x) := \int_1^\infty t^{-n} e^{-xt} dt = \int_0^1 \mu^{n-2} e^{-(x/\mu)} d\mu, \quad n \in \mathbb{N}^+, x \in \mathbb{R}_0^+. \quad (\text{A.1})$$

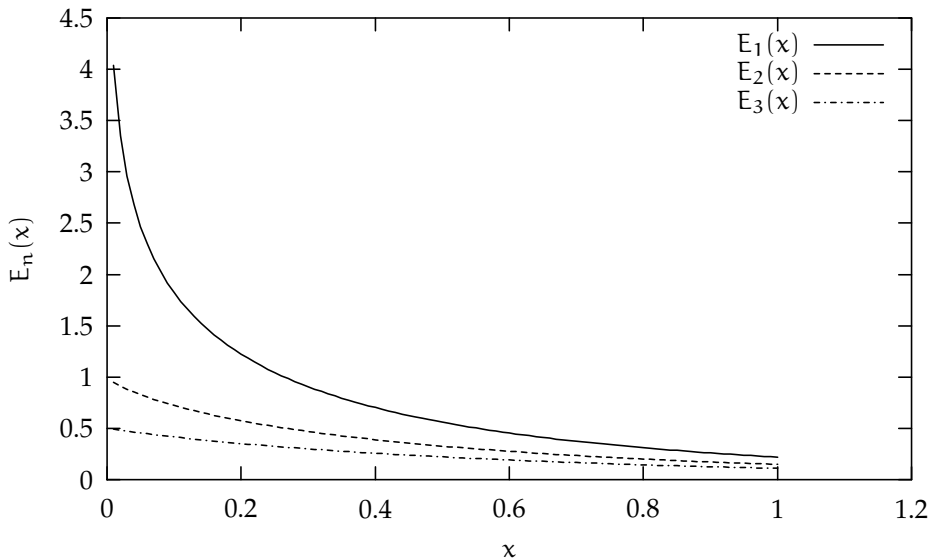


Figure A.1: The exponential integrals $E_1(x)$, $E_2(x)$ and $E_3(x)$

From the definition the following properties of the exponential integrals of different orders can be derived. By taking the derivative of (A.1), we see that

$$\frac{d}{dx} E_n(x) = \begin{cases} -\frac{1}{x} e^{-x}, & n = 1, \\ -E_{n-1}(x), & n = 2, 3, \dots \end{cases} \quad (\text{A.2})$$

Similarly, integration of (A.1), shows that

$$\int^x E_n(x) dx = -E_{n+1}(x) + C. \quad (\text{A.3})$$

By integrating the definition of E_{n+1} by parts, also a directly recurrent relationship can be found:

$$E_{n+1}(x) = \frac{1}{n} (e^{-x} - xE_n(x)), \quad n = 1, 2, \dots \quad (\text{A.4})$$

By taking $x = 0$ in (A.1), we see that the value in the origin is

$$E_n(0) = \begin{cases} \infty, & n = 1 \\ \frac{1}{n-1}, & n = 2, 3, \dots \end{cases} \quad (\text{A.5})$$

For the behaviour when x tends towards infinity, we see directly from (A.1), that

$$\lim_{x \rightarrow \infty} E_n(x) = 0. \quad (\text{A.6})$$

Bibliography

- [Alhazen, 1270] Alhazen (1270). *Kitab al-Manazir / Opticae Thesaurus Alhazeni*. The author's commonly used name is a latinised version of his real name *Abu Ali Hasan ibn Al-Haytham*. The book was first published in arab around the year 1000, and was translated into latin around 1270.
- [Barrett et al., 1994] Barrett, R., Berry, M., Chan, T. F., Demmel, J., Donato, J., Dongarra, J., Eijkhout, V., Pozo, R., Romine, C., and der Vorst, H. V. (1994). *Templates for the Solution of Linear Systems: Building Blocks for Iterative Methods, 2nd Edition*. SIAM, Philadelphia, PA.
- [Beerkens et al., 1997] Beerkens, R. et al. (1997). *NCNG Handbook For Glass Technologists 1997*.
- [Bressloff et al., 1995] Bressloff, N., Moss, J., and Rubini, P. (1995). Application of a new weighting set for the discrete transfer radiation model. In *Proceedings of the 3rd European Conference on Industrial Furnaces and Boilers*, volume 2, pages 208–215.
- [Buijze, 1989] Buijze, W. (1989). *Inleiding Electriciteit*. Delftse Uitgevers Maatschappij, Delft. in dutch.
- [Chai and Patankar, 2000] Chai, J. and Patankar, S. (2000). *Advances in Numerical Heat Transfer*, volume 2, chapter Finite-Volume Method for Radiation Heat Transfer. Taylor and Francus.
- [Chandrasekhar, 1960] Chandrasekhar, S. (1960). *Radiative Transfer*. Dover Publications, Inc., Toronto.
- [Fiveland, 1993] Fiveland, W. (1993). A finite element method of the discrete ordinate method for multi-dimensional geometries. *Radiative Heat Transfer: Theory and Applications, ASME paper HTD*, 244:41–48.
- [Fluent, 1999] Fluent (1999). *FLUENT 5 User Guide*. Fluent Inc., Lebanon (NH), USA.
- [Huygens, 1690] Huygens, C. (1690). *Traité de la Lumière*. Epsilon Uitgaven, Utrecht. ISBN 90-5041-022-7. This is a re-edition, with the original french text accompanied with a dutch translation.

- [Klar and Siedow, 1999] Klar, A. and Siedow, N. (1999). Boundary layers and domain decomposition for radiative heat transfer and diffusion equations: Applications to glass manufacturing processes. Technical Report Berichte Nr. 6, Universität Kaiserslautern and ITWM, Kaiserslautern.
- [Kuske, 1999] Kuske, S. (1999). *Modelling of Radiative Heat Transfer in Sooting Flames*. PhD thesis, Technical University Graz.
- [Laevksy et al., 1999] Laevksy, K., van der Linden, B., and Mattheij, R. (1999). Flow and heat transfer in pressing of glass products. *CIME*.
- [Laevsky, 2002] Laevsky, K. (2002). *Pressing of Glass in Bottle and Jar Manufacturing: Numerical Analysis and Computation*. PhD thesis, Eindhoven University of Technology.
- [Lathrop and Carlson, 1964] Lathrop, K. and Carlson, B. (1964). Discrete ordinates angular quadrature of the neutron transport equation. Technical Report 3186, Los Alamos Scientific Laboratory, Los Alamos, N.M.
- [Lentes and Siedow, 1998] Lentes, F. and Siedow, N. (1998). Three-dimensional radiative heat transfer in glass cooling processes. Technical Report Berichte Nr. 4, ITWM, Kaiserslautern.
- [Lentes and Siedow, 1999] Lentes, F. and Siedow, N. (1999). Three-dimensional radiative heat transfer in glass cooling processes. *Glass Science and Technology / Glasstechnische Berichte*, 72(6):188–196.
- [Limpens, 2000] Limpens, M. (2000). *A Design Tool for Conveyor Belt Furnaces*. PhD thesis, Eindhoven University of Technology.
- [Mihalas and Weibel-Mihalas, 1984] Mihalas, D. and Weibel-Mihalas, B. (1984). *Foundations of Radiation Hydrodynamics*. Oxford University Press, Oxford.
- [Nagtegaal, 2002] Nagtegaal, M. (2002). *Spectral Remote Sensing*. PhD thesis, Eindhoven University of Technology.
- [Nefedov, 1999] Nefedov, V. (1999). Simulation of glass flow in an oven. Technical Report RANA 99-11, Eindhoven University Of Technology.
- [Özişik, 1973] Özişik, M. (1973). *Radiative Transfer and Interactions with Conduction and Convection*. John Wiley and Sons, Inc., Toronto.
- [Planck, 1923] Planck, M. (1923). *Die Ableitung des Strahlungsgesetzes: Sieben Abhandlungen aus dem Gebiete der elektromagnetischen Strahlungstheorie*. Akademische Verlagsgesellschaft, Leipzig. The article concerning the derivation the emissive energy of a blackbody is called *Über das Gesetz der Energieverteilung im Normalspektrum*, which appeared originally in 1901.
- [Robb et al., 2002] Robb, K., Kulkarni, J., Kumar, A., Dutta, A., and Grald, E. (2002). Numerical simulation of the draw down phenomenon in glass furnace forehearth. In *Proceedings of The Second International Colloquium on Modelling of Glass Forming and Tempering*, number 1 in Valensciences, pages 140–149. Presses Universitaires de Valenciennes.

- [Rosseland, 1936] Rosseland, S. (1936). *Theoretical Astrophysics. Atomic Theory And The Analysis Of Stellar Atmospheres And Envelopes*. Clarendon Press, Oxford.
- [Slob, 1997] Slob, M. (1997). Numerical modelling of radiative heat transfer in semi-transparent media. Master's thesis, Eindhoven University of Technology. Department of Mathematics and Information Technology.
- [Smith et al., 1996] Smith, B., Bjørstad, P., and Gropp, W. (1996). *Domain Decomposition. Parallel Multilevel Methods for Elliptic Partial Differential Equations*. Cambridge University Press.
- [Tapley and Poston, 1989] Tapley, B. and Poston, T. (1989). *Eschbach's Handbook Of Engineering Fundamentals, Fourth Edition*. John Wiley and Sons, Inc., Toronto.
- [Uede et al., 2000] Uede, M., Imada, M., Tanaka, K., and Murakami, K. (2000). The optimization for the reheating furnace with the technique of the highly preheated air combustion. In *Proceedings of 2000 International Joint Power Generation Conference, IJPGC2000-15082*.
- [van der Linden, 2002] van der Linden, B. (2002). Domain decomposition for radiative heat transfer using the algebraic ray trace methode. In *Proceedings of The Second International Colloquium on Modelling of Glass Forming and Tempering*, number 1 in Valensciences. Presses Universitaires de Valenciennes.
- [van der Linden and Mattheij, 1999a] van der Linden, B. and Mattheij, R. (1999a). A new method for solving radiative heat problems in glass. *International Journal of Forming Processes*, 2(2–3):41–61.
- [van der Linden and Mattheij, 1999b] van der Linden, B. and Mattheij, R. (1999b). *Progress in Industrial Mathematics at ECMI'98*, chapter Algebraic Ray Tracing, pages 90–96. B.G. Teubner, Stuttgart.
- [Wang, 2002] Wang, K. (2002). *BEM Simulation for Glass Parisons*. PhD thesis, Eindhoven University of Technology.
- [Yang et al., 1995] Yang, W.-J., Taniguchi, H., and Kudo, K. (1995). Radiative heat transfer by the monte carlo method. *Advances in Heat Transfer*, 27.

Index

- absorption coefficient
 - Rosseland mean –, 39
 - spectral –, 16
- absorptivity, 22
- algebraic ray trace method, *see* ARTM
- ARTM, 59
- average cooling, 122
- average relative error, 123
- average temperature, 122

- black boundary, 19, 31
- blackbody, 11
- blackbody intensity, 11

- conductive heat flux, 12
- conductivity
 - thermal –, 106
- convection, 106
- convective heat flux, 106
- convective heat transfer coefficient, 112
- cooling
 - average –, 122
- Coulomb's Law, 49
- critical angle, 24

- density, 106
- diffuse reflection, 34
- diffusion coefficient
 - Fourier, 13
 - Rosseland, 39
- dimensionless radiative heat flux, 110
- discrete ordinate method, *see* DOM
- DOM, 47
- dwelt, 108–112, 117

- electrical permittivity, 49
- electrical potential, 50
- electrical potential energy, 50
- emissivity
 - directional –, 22
- error
 - average relative –, 123
 - maximum local –, 124
- exact solution, 28
- exponential integral, 30, 141

- feeder, 107
- finite element formulation, 57
- formal solution, 17
- Fourier diffusion coefficient, 13
- Fourier number, 109
- Fourier's Law, 106
- Fresnel reflection, 23, 130

- grey medium, 16

- heat flux
 - conductive –, 12
 - radiative –, 13, 30
- heat transfer
 - convective –, 106

- incident radiation, 14
- intensity, 10
 - blackbody –, 11
 - mean, 14
- irradiance, 19

- Level Symmetric Sets, 48
- level symmetric sets, 48
- local thermodynamic equilibrium, 16

- maximum local error, 124
- MDD, 99
- modified diffusion approximation, 38, 43
- modified domain decomposition, *see* MDD
- monochromatic, 11

- Monte Carlo Method, 55
- mould
 - pressing –, 107
- neck ring, 74, 83, 103, 117
- Nusselt number, 114
- one-dimensional solution, 28
- optical
 - distance, 17
 - geometry, 31
 - thickness, 18
- optical Fourier number, 110
- parison, 46, 107
- Planck function, 11
- plunger, 107
- press-and-blow, 107
- pressing mould, 107
- quasi-homogeneous sets, 49
- radiation tensor, 15
- radiative
 - energy density, 14
 - heat flux, 13, 15, 30
 - stress tensor, 15
 - transfer equation, *see* RTE
- radiosity, 19
- ray effect, 92
- Ray Trace Method, 55
- ray trace method, 17
- reflection
 - diffuse –, 21, 34
 - distribution function, 20
 - Fresnel –, 23, 130
 - monochromatic –, 20
 - specular –, 21, 32
- reflectivity
 - diffuse –, 21
 - directional-hemispherical –, 20
 - hemispherical-directional –, 20
 - specular –, 21
- refractive index, 11, 23
- reheat, 108, 112–117
- Rosseland
 - approximation, 38
 - depth, 42
 - diffusion coefficient, 39
 - mean absorption coefficient, 39
- Rosseland number, 109
- RTE, 17
- scattering, 16
- semi-transparent, 9
- specific heat, 106
- specular reflection, 32
- temperature
 - average –, 122
- thermal conductivity, 13, 106
- thermal diffusivity, 109

Summary

The production of glass objects occurs at such high temperatures, that the glass emits a visible yellow/orange glow. Most heat, however, is emitted in the invisible infrared part of the electromagnetic spectrum. On a visit to a glass maker, such as the ones on the island of Murano near Venice, one can learn that the emitted heat remains to be felt, even after the glass has cooled down enough to lose the glow. For a reliable simulation of glass production processes it is necessary to model this radiative heat transfer accurately. After all, the temperature and the gradients that occur in production of glass have a big influence on the quality of the end product. Detailed knowledge of the temperature distribution is also required in the research to furnace abrasion, energy consumption and detailed chemical composition of the glass.

The physical description of radiative heat transfer has been known since the start of the twentieth century. From then on, computation of the radiative heat flux has been possible, yet most applications are restricted to radiative transfer between surfaces. The radiative field inside glass, however, is rather more complex. Because of the transparency of glass, radiation is being partially absorbed and partially transmitted at every point in the glass. This calls for treatment of radiation throughout the domain instead of just at the boundaries. Furthermore, the high temperature of the glass causes radiation to be spontaneously emitted at every point. These phenomena create a strong coupling in the temperature at different points, even if these points are not nearby. In the numerical treatment of a problem, such a coupling re-surfaces as a full matrix, where the number of elements scales quadratically with the number of nodes. For a three-dimensional model, where usage of more than ten thousands of nodes is not uncommon, such a matrix size would approach or exceed the limit of what present day computers can retain in memory. The situation is complicated further by the reflective boundary conditions that occur in the description of radiative problems. Such boundary conditions create a coupling between radiation in different directions, which necessitates the use of an iterative approach to solve a radiative heat problem, thereby further increasing the required computing time.

Existing numerical models for radiative heat transfer are often not appropriate for use in glass production simulations. These models can be split in two categories. The models in the first category simplify the original problem by making some physical assumptions. Such numerical models typically result in a method that is numerically cheap, but has a limited application area. For example, the popular Rosseland Approximation can only be used accurately in the computation of the temperature inside the thick glass bath of a melting furnace. For

other processes this method creates large inaccuracies. The second category of existing methods, tries to compute the radiation inside the glass as accurately as possible. To this end, methods such as the Ray Trace Method, compute the intensity in all nodes and in all discretized directions. Although the accuracy of such methods is high, these methods consume large amounts of memory and computing time when used for problems in semi-transparent media such as glass. In case of reflective boundaries, the required work increases further as it calls for an iterative approach.

The Algebraic Ray Trace Method (ARTM) that we derive in this dissertation, tries to overcome the complexity associated with the second category of solution methods. The ARTM resembles the (classic) Ray Trace Method, but by storing the required operations in a couple of matrices, it avoids repetition of the actual tracing of the rays. Using the ARTM only the intensity at the boundary needs to be computed explicitly. This is done by solving a system of linear equations, where an arbitrary solver can be used. The computation of the radiative heat flux in the remaining nodes occurs by some matrix-vector multiplications without having to compute the intensity first. It is shown that the method is accurate. The resulting matrices are still too large for 3D applications. Therefore, additional complexity reduction schemes are derived. The construction of such schemes is facilitated by the notation offered by the ARTM. To reduce the complexity caused by the interdependency of the nodes, we present a domain decomposition method that does not require iteration between the subdomains. It allows for a simultaneous reduction in memory requirement and computing time that scales linearly with the number of subdomains. Furthermore, we show a method to avoid the complexity associated with diffusely reflecting boundaries.

The use and results of the method are illustrated by three practical examples. First, the effects of some different radiation models is illustrated by means of a simple one-dimensional model for the forming process of a jar. A similar problem is investigated in more dimensions in the second example, where we solve the heat equation for a neck ring geometry. In the final example we study how the insertion of a thermocouple into a crucible with glass affects the temperature distribution.

Samenvatting

Het fabriceren van glazen producten gebeurt bij hoge temperaturen; zo hoog zelfs dat het glas een zichtbare oranje-gele gloed afgeeft. De meeste warmte wordt echter in het onzichtbare, infrarode gedeelte van het elektromagnetisch spectrum uitgezonden. Bij een bezoek aan een glasblazerij, zoals de bekende eeuwenoude blazerijen op het eiland Murano bij Venetië, leert men dat de uitgestraalde warmte vanaf een afstand voelbaar blijft, zelfs nadat de gloed is verdwenen. Voor een betrouwbare simulatie van glas-productie is het nodig deze warmte-overdracht nauwkeurig te modelleren. De temperatuur en temperatuurverschillen, die tijdens de productie optreden, hebben immers een grote invloed op de kwaliteit van het eindproduct. Ook bij bestudering van bijvoorbeeld ovenslijtage, energieverbruik en precieze chemische samenstelling van het glas is een gedetailleerde kennis van de temperatuur essentieel.

De natuurkundige beschrijving van stralingswarmte is reeds sinds het begin van de twintigste eeuw bekend. Sindsdien is het berekenen van de stralingsflux mogelijk, maar in de meeste toepassingen wordt doorgaans gekeken naar stralings-overdracht tussen verschillende oppervlakken. De stralingshuishouding in glas is echter een stuk complexer. Doordat glas transparant is, wordt overal in het domein een deel van de stralingswarmte opgenomen en een deel doorgelaten. Daarom dient de warmtestraling overal in het glas bepaald te worden en niet slechts op de rand. Door de hoge temperatuur van het glas zal bovendien elk punt in het glas warmtestraling uitzenden. Dit zorgt voor een sterke koppeling van de temperatuur tussen verschillende punten, zelfs als ze niet vlak bij elkaar liggen. Zo'n directe relatie komt numeriek-wiskundig terug als een volle matrix met een aantal elementen dat kwadratisch afhangt van het aantal punten dat bekeken wordt. Voor een driedimensionaal model, waarbij tienduizenden of meer punten gebruikt worden, betekent dit een geheugenbehoefte die de grens nadert van wat hedendaagse computers bieden. De situatie wordt nog verder gecompliceerd door spiegelende randvoorwaarden die voor de beschrijving van straling nodig zijn. Zulke randvoorwaarden maken een koppeling tussen straling in verschillende richtingen aan de rand, waardoor doorgaans een iteratie nodig is alvorens een stralingswarmteprobleem kan worden opgelost.

Bestaande numerieke modellen voor stralingswarmte zijn vaak niet inzetbaar voor gebruik in simulaties van glasproductie. Deze modellen kunnen in twee categorieën worden ondergebracht. De modellen in de eerste categorie maken een vereenvoudiging door middel van fysische aanname. Methodes in deze categorieën resulteren typisch in een goedkope methode, maar hebben vaak maar een beperkte inzetbaarheid. Zo kan bijvoorbeeld de populaire Rosseland Be-

nadering alleen accuraat worden ingezet voor berekeningen binnen het dikke glasbad van een smeltoven; voor andere processen levert deze benadering grote onnauwkeurigheden. De tweede categorie van bestaande methoden probeert de fysische beschrijving zo nauwkeurig mogelijk op te lossen. Methodes zoals de Ray Trace Methode berekenen daartoe de intensiteit in elk punt en elke gediscrètiseerde richting. Hoewel voor deze methodes de oplossing nauwkeurig is, is er veel rekenwerk en geheugenruimte mee gemoeid als deze methodes worden toegepast in semi-transparante media zoals glas. Indien er spiegelende randen aanwezig zijn, neemt het rekenwerk nog verder toe, omdat in dat geval een iteratieve benadering noodzakelijk is.

De Algebraïsche Ray Trace Methode (ARTM) die we in deze dissertatie afleiden, probeert de complexiteit van de tweede categorie oplosmethoden in te perken. De methode vertoont sterke gelijkenis met de (klassieke) Ray Trace Methode, maar door de benodigde operaties op te slaan in verschillende matrices wordt vermeden dat steeds opnieuw getracet moet worden. In de ARTM behoeft alleen de intensiteit op de rand expliciet berekend te worden. Dit gebeurt door middel van een stelsel lineaire vergelijkingen, dat met een willekeurige solver kan worden opgelost. De warmteflux in de overige punten kan dan via enkele matrix/vectorvermenigvuldigingen worden gevonden zonder eerst de intensiteit te bepalen. Er wordt aangetoond dat deze methode nauwkeurig is. De resulterende matrices zijn voor 3D applicaties echter te groot. Daarom zijn er diverse verdere oplossingen bedacht om de complexiteit terug te dringen. Het vinden van zulke mogelijkheden wordt vergemakkelijkt door de notatie van de ARTM. Om de complexiteit te verminderen, die wordt veroorzaakt door de afhankelijkheid die punten op elkaar hebben, laten we een domeindecompositie zien die geen extra iteraties tussen de subdomeinen nodig heeft. Hierdoor kan zowel de geheugenbehoefte als rekentijd lineair met het aantal subdomeinen worden teruggedrongen. Verder laten we een speciale behandeling van diffuus spiegelende randen zien, welke de daarmee geassocieerde complexiteit laat verdwijnen.

De werking en uitwerking van de methode worden tenslotte geïllustreerd aan de hand van enkele praktijkgerichte voorbeelden. Eerst vergelijken we de resultaten van verschillende methodes in een eenvoudig één-dimensionaal model voor het vormgeef-proces van een flesje. Hetzelfde probleem wordt in meer dimensies onderzocht in het tweede voorbeeld, waar we de warmtehuishouding in de bovenkant van een glazen pot bekijken. In het derde en laatste voorbeeld, bestuderen we de effecten op de temperatuur, die worden veroorzaakt door het inbrengen van een thermokoppel in een meetopstelling.

